NONLINEAR VIBRATION OF MICROMECHANICAL RESONATORS

SHAO LICHUN

NATIONAL UNIVERSITY OF SINGAPORE

2008

NONLINEAR VIBRATION OF MICROMECHANICAL RESONATORS

SHAO LICHUN

(B.ENG., SHANGHAI JIAOTONG UNIVERSITY)

A THESIS SUBMITTED

FOR THE DEGREE OF DOCTOR OF PHILOSOPHY

DEPARTMENT OF ELECTRICAL AND COMPUTER ENGINEERING

NATIONAL UNIVERSITY OF SINGAPORE

2008

Acknowledgments

I would first like to express my deep appreciation to my supervisors Dr. Moorthi Palaniapan and Associate Professor Tan Woei Wan for their guidance and encouragement throughout my PhD study in National University of Singapore. Without their constant support, this work would not be possible. I would also like to thank Associate Professor Xu Yongping and Dr. Lee Chengkuo, Vincent for their genuine comments and advice on my research.

Many thanks also go to my good friends at NUS: Mr. Zhu Zhen, Mr. Zhao Guangqiang, Mr. Chen Yuan, Mr. He Lin, Mr. Yan Han, Mr. Feng Yong, Mr. Chen Ming, Mrs. Wang Yuheng, Ms. Lim Li Hong and many others for providing a stimulating environment for good research. Special thanks go to my group members: Mr. Khine Lynn, Mr. Wong Chee Leong and Mr. Niu Tianfang for their fruitful discussions and suggestions on the research topics.

I acknowledge Advanced Control Technology Laboratory, Signal Processing & VLSI Laboratory, Center for Integrated Circuit Failure Analysis & Reliability and PCB Fabrication Laboratory for providing the measurement equipments, MEMSCAP Inc. for device fabrication and National University of Singapore for the financial support.

Last but not least, my appreciation goes to my parents. Their love and care always make me strong and help me face all the difficulties in life. This degree is shared with them.

Table of contents

Abstract

In this thesis, a semi-analytic technique is proposed to characterize and model the nonlinearities in micromechanical resonators. Unlike conventional techniques which usually have limited applicability and insufficient accuracy, the proposed technique can be applied to virtually any types of resonators and is capable of extracting the accurate nonlinear model of the resonator from just a few preliminary experimental observations. Based on the extracted model, the nonlinear behavior of the resonator under different driving conditions can be predicted. Furthermore, the intrinsic nonlinear properties such as the amplitude-frequency coefficient and power handling capability can be revealed. Using the proposed technique, we study the nonlinear behaviors of both flexural mode and bulk mode resonators including a 615 kHz fundamental-mode free-free beam resonator, a 550 kHz second-mode free-free beam resonator, a 194 kHz clamped-clamped beam resonator and a 6.35 MHz Lamé-mode resonator. Besides, we compare the flexural mode and bulk mode resonators. It is found that bulk mode resonators have much better performance in terms of the resonant frequency, quality factor, amplitude-frequency coefficient and power handling capability than their flexural mode counterparts towards the VHF and UHF ranges.

Motivated by the superior performance of the bulk mode resonators, in the last chapter of the thesis, some further studies are conducted. Firstly, the effect of etch holes on the quality factor of the resonator is investigated. Secondly, a novel technique is proposed to reduce the capacitive gap size of the resonator to sub-micron range using a standard 2μm

process. Results of these two studies will be very useful for optimal design of bulk mode resonators.

List of figures

List of tables

Nomenclature

Abbreviations	**Description**
AC	Alternating current
AGC	Automatic gain control
cc beam	Clamped-clamped beam
CMOS	Complementary metal-oxide-semiconductor
DC	Direct current
DRIE	Deep reactive ion etch
FEM	Finite element modeling
ff beam	Free-free beam
IC	Integrated circuit
MEMS	Micro electromechanical system
PCB	Printed circuit board
RF	Radio frequency
SAW	Surface acoustic wave
SEM	Scanning electron micrograph
SOI	Silicon on insulator
UHF	Ultra high frequency (300 MHz to 3 GHz)
VHF	Very high frequency (30 MHz to 300 MHz)

Symbols	Definition
C_f	Feedback capacitance of the trans-impedance amplifier
C_m	Series motional capacitance of the resonator
d	Nominal gap size between the resonator and fixed electrode
d_{final}	Final gap size after pull-in
d_0	Original gap size
d_S	Gap size between the electrode and stopper
E	Young's modulus (Si <110>: 170 GPa)
$E_{dissipated}$	Energy dissipated per cycle
E_{stored}	Energy stored per cycle
$E_{stored}^{\max}$	Maximum storable energy of the resonator
f_0	Resonant frequency under linear vibration
f_0'	Resonant frequency under nonlinear vibration
Δf	Frequency offset
Δf_{3dB}	Bandwidth at 3dB below the resonance peak
$F\cos(2\pi ft)$	Applied harmonic force
F_C	Magnitude of the critical applied harmonic force
F_e	Electrostatic force
$F_{e,harmonic}$	Electrostatic harmonic driving force
$F_{e,spring}$	Electrostatic spring force
F_L	Magnitude of the applied harmonic force under linear vibration
F_m	Mechanical force

F_N	Magnitude of the applied harmonic force under nonlinear vibration
G	Shear modulus
h	Structure thickness (25 μm)
i_0	Output current resulting from the vibration of the resonator
$i_{0,f_0'}$	Output current at f_0'
k	Boltzmann's constant ($1.38\times10^{-23} J\bullet K^{-1}$)
k_1	Effective linear spring constant
k_2	Effective quadratic spring constant
k_3	Effective cubic spring constant
k_{1e}	Linear electrostatic spring constant
k_{3e}	Cubic electrostatic spring constant
k_{1m}	Linear mechanical spring constant
k_{3m}	Cubic mechanical spring constant
k_s	Linear spring constant of the support beam
l	Linear dimension of the resonator
L	Edge length of the Lamé-mode resonator
L_m	Support beam separation
L_r	Length of the beam resonator
L_s	Length of the support beam
m	Lumped mass of the resonator
M	Number of capacitive gaps formed between the resonator and one of the fixed comb-finger electrodes
N	Number of drive/sense electrodes

P	Pressure
Q	Quality factor
Q_L	Quality factor under linear vibration
Q_N	Quality factor under nonlinear vibration
Q_{loaded}	Loaded quality factor
$Q_{unloaded}$	Unloaded quality factor
R_f	Feedback resistance of the trans-impedance amplifier
R_L	Equivalent loading resistor
R_m	Series motional resistance of the resonator
$R_{m\_measured}$	Measured series motional resistance of the resonator
t	Time
T	Absolute temperature
TC_f	Temperature coefficient
v_{ac}	Input AC excitation voltage
V_P	Polarization voltage
$V_{pull\text{-}in}$	Pull-in voltage limit
$V_{pull\text{-}out}$	Pull-out voltage limit
W_e	Electrode width
W_r	Width of the beam resonator
W_s	Width of the support beam
y	Displacement of the resonator
Y_C	Critical vibration amplitude at the onset of frequency hysteresis
Y_L	Vibration amplitude under linear vibration

Y_N	Vibration amplitude under nonlinear vibration
$Y_{0,f_0'}$	Vibration amplitude at f_0'
α	Effective amplitude-frequency coefficient
α_e	Amplitude-frequency coefficient due to cubic electrostatic spring constant
α_m	Amplitude-frequency coefficient due to cubic mechanical spring constant
β	Fitting coefficient of cubic nonlinear spring constant
β_n	Mode coefficient
ε_0	Permittivity of free space ($8.854\times10^{-12}F/m$)
κ	Nonlinear parameter $\kappa = \frac{3k_3}{8k_1}f_0 - \frac{5k_2^2}{12k_1^2}f_0$
σ	Scaling factor
ρ	Density of the structural material (Si: $2330kg/m^3$)
γ	Damping coefficient
ν	Poisson’s ratio

Chapter 1 Introduction

1.1 What is a micromechanical resonator?

A micromechanical resonator is a micro-sized mechanical device with a vibratory natural response. Since the development in the 1980's (Howe R T, 1983), these resonators have attracted extensive attention in various applications such as inertial sensors (Schmidt M A, 1986; Tilmans H A, 1992; Andrews M K, 1993), reference oscillators (Nguyen C T C, 1993; Kaajakari V, 2004), bandpass filters (Wang K, 1999; Pourkamali S, 2005) and mixers (Wong A C, 2004). Currently, several efforts are underway to commercialize these micro devices. For example, micromechanical resonators with frequencies in the GHz range have already been reported (Wang J, 2004). Quality factor exceeding one million has also been demonstrated (Palaniapan M, 2007) while active and passive control of temperature sensitivity is being investigated (Ho G K, 2005; Ho G K, 2006). Compared with the conventional frequency selective components such as quartz crystals (Frerking M E, 1996) and surface acoustic wave (SAW) resonators (Wright P V, 1992; Berkenpas E, 2004), micromechanical resonators have several major advantages as follows:

1) Compact size

Compact size is probably the most obvious incentive for using micromechanical resonators. In contrast with the several mm^2 required for a quartz crystal (Vanlong Technology Co., Ltd., 2008), typical dimensions of micromechanical resonators are in the range of 100 μm by 100 μm or even smaller (Nguyen C T C, 1999; Pourkamali S, 2004). Such substantial size difference makes micromechanical resonators very promising in replacing their macroscopic counterparts in portable applications.

2) High integrability

The second direct benefit of using micromechanical resonators is high integrability. Micromechanical resonators can be fabricated using the same process used to manufacture integrated circuits (ICs). Several technologies that merge CMOS process with micromachining process have already been developed and implemented including MEMS-first approaches (Smith J, 1995; Kung J T, 1996) and CMOS-first approaches (Franke A E, 1999; Takeuchi H, 2004). The full integration is highly appealing because it not only reduces the manufacturing and packaging cost, but also eliminates the cumbersome chip-to-chip wire bonding requirements and hence minimizes the interconnect parasitics.

3) Performance benefits

In addition to the size and integrability advantages, micromechanical resonators also provide some other performance benefits as well. For instance, micromechanical resonator based oscillators typically dissipate much less power than crystal oscillators. It has been shown that the standby current of resonator-based oscillators can be as low as 1μA (Discera MOS1), which is more than ten times less than those of the typical crystal oscillators (Epson SG8002LB, NDK 2775Y). Moreover, micromechanical resonators have been demonstrated to be more resilient against vibration and shock than quartz crystals (Lin Y W, 2005). This enables the use of micromechanical resonators in harsh environment.

1.2 Different types of micromechanical resonators

Like many other MEMS devices, micromechanical resonators can be classified according to different criterions. The first criterion classifies the resonators according to their driving and sensing configurations. Specifically, driving of the resonator can be implemented in several ways, including piezoelectric films (Smits J G, 1985), magnetostatic forces (Ikeda K, 1988) and electrostatic forces (Howe R T, 1987; Nguyen C T C, 1993). Similarly, vibration can be sensed by means of piezoelectric films (Smits J G, 1985), optical techniques (Lavigne G F, 1998) and capacitance variations (Howe R T, 1987; Nguyen C T C, 1993). Among different possible combinations of driving and sensing configurations, electrostatic driving and capacitive (electrostatic) sensing is one of the most popular approaches mainly due to its simplicity and compatibility with the IC technologies. Hence, nowadays most of the micromechanical resonators in the market are actually capacitive.

The second classification method divides the micromechanical resonators into flexural mode and bulk mode resonators according to their modes of operation. Flexural vibration mode can be treated as transverse standing waves while bulk mode operation is longitudinal standing waves. To illustrate the performance difference between these two vibration modes, Table 1.1 lists the frequency and quality factor, two major figures of merit, of several recently reported micromechanical resonators.

Table 1.1 Recently reported micromechanical resonators and their resonant frequencies and quality factors.

Category	**Resonator**	**Resonant freq.**	**Quality factor**	**Source**
Flexural mode	Comb-drive folded beam	19 kHz	51,000	Nguyen C T C, 1999
	Clamped-clamped beam	8.5 MHz	8,000	Bannon F D, 2000
	Free-free beam	10 MHz	10,743	Hsu W T, 2001
	Double-ended tuning fork	400 kHz	11,000	Agarwal M, 2007
Bulk mode	Elliptical bulk-mode	150 MHz	46,000	Pourkamali S, 2004
	Radial-contour mode disk	1.51 GHz	11,555	Wang J, 2004
	Square extensional mode	13.1 MHz	130,000	Kaajakari V, 2004a
	Lamé-mode	6.3 MHz	1.6 million	Palaniapan M, 2007

As shown in Table 1.1, most of the beams vibrate in flexural mode while squares and disks normally work in bulk mode. Due to the soft beam structures, the flexural mode resonators generally have much lower resonant frequencies and quality factors than their bulk mode counterparts. Although the comb-drive folded beam resonator can achieve quality factor as high as 51,000, its large mass and small spring constant limit its resonant frequency. Hence, recent research interests are being shifted from flexural mode to bulk mode resonators in order to get ultra high resonant frequencies and quality factors at the same time.

1.3 Nonlinearities in micromechanical resonators

Despite the popularity and diversity, micromechanical resonators still face some technical challenges. For example, the thermal stability of micromechanical resonators (without compensation) is usually much worse than quartz crystals (Hsu W T, 2000). Another more serious issue is resonators' nonlinearities resulting from large vibration amplitudes. In most of the applications, resonator's nonlinearities are highly undesirable because they limit the ultimate resonator performance that can be achieved (Kaajakari V, 2004b). According to (Lee S, 2004) and (Kaajakari V, 2005), resonator-based oscillators suffered from increased close-to-carrier phase noise when they were operated in the nonlinear regime. Roessig T A also showed that nonlinearities degraded the resolution of the resonator-based inertial sensor (Roessig T A, 1998). Hence, it is crucial for engineers to understand the nonlinear dynamics of the resonator in order to achieve optimal device performance.

Unfortunately, the nonlinear vibration mechanism of micromechanical resonators is very complex, since the nonlinearities couple both mechanical and electrostatic energy domains. So far, several methods have been reported to deal with this complexity. In general, these methods can be divided into three categories:

1) Analytic derivation,
2) Finite-element-modeling (FEM) calculation and
3) Experimental curve fitting.

The first analytic approach has been widely adopted by mechanical engineers. Tilmans and Legtenberg (Tilmans H A, 1994) analyzed the nonlinear effects using a modified Rayleigh's energy method to incorporate both the electrostatic force and mid-plane stretching of a microbeam resonator. They derived an equation to relate the resonant frequency to the vibration amplitude. They compared the results obtained using this equation with the experimental results. Although a qualitative agreement was obtained, the agreement was poor quantitatively.

Turner and Andrews (Turner G C, 1995) studied the nonlinear response of a microbeam using a perturbation method. They modeled the microbeam as a spring-mass system and including the cubic nonlinear spring constant. Using the method of harmonic balance, they derived an equation describing the resonant frequency of the microbeam resonator. Their results showed that to eliminate the dependence of resonator frequency on the vibration amplitude, a very high DC polarization voltage was needed, which may not be attainable in practice.

Gui et al. (Gui C, 1998) solved the nonlinear problem of a microbeam using the Rayleigh’s energy method with some modifications to account for electrostatic force and mid-plane stretching. They derived an equation for the resonant frequency and predicted a spring-hardening behavior. They compared their analytical results with experiments and found reasonable agreement.

One commonality among these reported analytic methods is that all of them only applicable to simple microbeam resonators. The analytic methods are generally highly mathematical and for more complicated structures such as free-free beam or even bulk mode resonators, there are no analytic models yet. Furthermore, most of the existing models are formulated with pre-assumed behavior. For instance, the nonlinearity is assumed to be cubic and positive to justify the observed hardening behavior whereas the nonlinearity due to electrostatic force is ignored. Besides, in some cases, the microbeam is modeled as a lumped spring-mass system and thereby neglecting the distributed mass and electrostatic force. Hence, the accuracy of the modeling is still not satisfactory.

As an alternative, recently most of the researchers try to extract the nonlinear stiffness in the spring force using FEM tools such as ANSYS or ABAQUS. Veijola and Mattila (Veijola T, 2001) utilized ANSYS to extract both the linear and cubic spring constants of a microbeam resonator. Subsequently, they substituted the extracted parameters into an equivalent circuit model. In this model, different elementary circuit blocks were constructed to implement the force acting on the resonator. The equivalent circuit was then simulated using the harmonic balance method in an RF-circuit simulator APLAC, manifesting both the spring hardening and softening behavior.

Kinnell et al. (Kinnell P K, 2004) performed ABAQUS simulation to obtain the cubic spring constant of a double-ended-tuning-fork (DETF) resonator in its fundamental and second vibration mode, respectively. In their simulation, the DETF structure was constrained to deformations equivalent to the dynamic vibration mode shape. By relating the total strain energy or internal work to the vibration amplitude, the equivalent cubic spring constant was determined using Castigliano’s theorem.

Although the FEM based approach is very convenient to use, the reported data shows that the accuracy of FEM calculation is only around 60% to 70%. The discrepancy in FEM modeling can be attributed to distributed force over the length of the transducer (Bannon F D, 2000), variations in the modulus of elasticity (Kaajakari V, 2004b), process imperfection (Miller D C, 2007) etc., all of which are difficult to quantify.

Another nonlinear modeling technique involves experimental curve fitting. Ayela and Fournier (Ayela F, 1998) experimentally studied several microbeam resonators with different geometries. They showed that the resonant frequency became dependant on the vibration amplitude when the resonator was in the nonlinear operation regime. The experimental data was then used to extract the linear and cubic spring constants to fit the equation of a spring-mass system. However, this study neglected the electrostatic nonlinearities and concluded that dynamic behaviors of different resonators needed to be investigated separately.

From the above discussion, we can see that the literature still lacks a generalized approach which is convenient to use, yet accurate to model the nonlinearities in micromechanical resonators. In order to address the limitations of the existing methods, this thesis presents a general-purpose semi-analytic modeling technique which combines the analytic derivation with experimental curve fitting. The proposed technique incorporates both the mechanical and electrostatic nonlinearities and enables the accurate extraction of nonlinear resonator model from just a few preliminary measurement results. Based on this technique, we comprehensively studied and compared the nonlinear properties of both flexural mode and bulk mode resonators including free-free beam resonators, clamped-clamped beam resonators and Lamé-mode resonators. For all these devices, excellent agreements were achieved between the nonlinear models and the experimental results, confirming the reliability of the proposed technique.

1.4 Thesis organization

This thesis consists of six chapters and is organized in the following way. In Chapter 2, the mathematical nonlinear model of the micromechanical resonator is presented and the effects of nonlinearities on the resonator performance are discussed. Chapter 3 proposes a general-purpose semi-analytic technique and its application in characterizing and modeling the nonlinear behaviors of flexural mode free-free beam and clamped-clamped beam resonators. The useful nonlinearity cancellation phenomenon is also investigated in detail. Chapter 4 extends the application of the proposed semi-analytic technique to the study of nonlinearities in Lamé-mode bulk resonators. Comparison between the flexural mode and bulk mode resonators reveals that bulk mode resonators have much better performance than their flexural mode counterparts towards the VHF and UHF ranges. In Chapter 5, further studies are conducted on bulk mode resonators. Firstly, the effect of release etch holes on the resonator performance is analyzed. Secondly, a novel technique is proposed to reduce the capacitive gap size and motional resistance of the resonator. Chapter 6 summarizes the thesis and provides some recommendations for future work.

Chapter 2 Nonlinear vibration of micromechanical resonators

In this chapter, we will first review the linear equation of motion of micromechanical resonators. Next, the nonlinear equation of motion will be introduced. Detailed mathematical analysis will be provided to model mechanical nonlinearities, electrostatic nonlinearities and quality factors. Furthermore, the effects of nonlinearities on the resonator performance will be addressed.

2.1 Linear model of micromechanical resonators

A typical micromechanical resonator can be treated as a lumped single-degree-of-freedom spring-mass-damper system, as shown in Fig. 2.1.

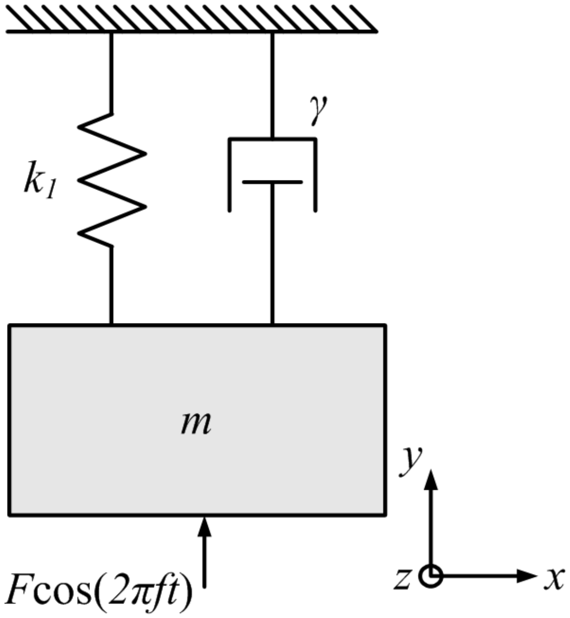

Figure 2.1 Resonator as a spring-mass-damper system.

According to Newton's Second Law of Motion, the dynamic equation of motion of the resonator along y-axis can be written as:

$$m\frac{d^2y}{dt^2}+\gamma\frac{dy}{dt}+k_1y=F\cos\left(2\pi ft\right) \tag{2.1}$$

where

t = time,

y = displacement of the resonator,

m = lumped mass of the resonator,

γ = damping coefficient,

k_1 = effective linear spring constant of the resonator and

$F\cos(2\pi ft)$ = applied harmonic force.

Solving Eq. (2.1) for the amplitude of vibration gives:

$$\left|y\right|=\frac{F/m}{4\pi^2\sqrt{\left(f^2-f_0^2\right)^2+\left(f\,f_0/Q\right)^2}} \tag{2.2}$$

where

$$f_0=\frac{1}{2\pi}\sqrt{\frac{k_1}{m}} \tag{2.3}$$

is denoted as the "resonant frequency" and

$$Q=\frac{\sqrt{k_1m}}{\gamma} \tag{2.4}$$

is known as the "quality factor".

Fig. 2.2 (a) plots the amplitude-frequency response of the resonator (Eq. (2.2)). At low frequencies, the vibration amplitude is proportional to the harmonic force in the form $|y| = F / k_1$ whereas at resonant frequency f_0, the vibration amplitude is enhanced by a factor of Q. As the focus of this thesis is on resonators, we will concentrate on the response near the resonant frequency.

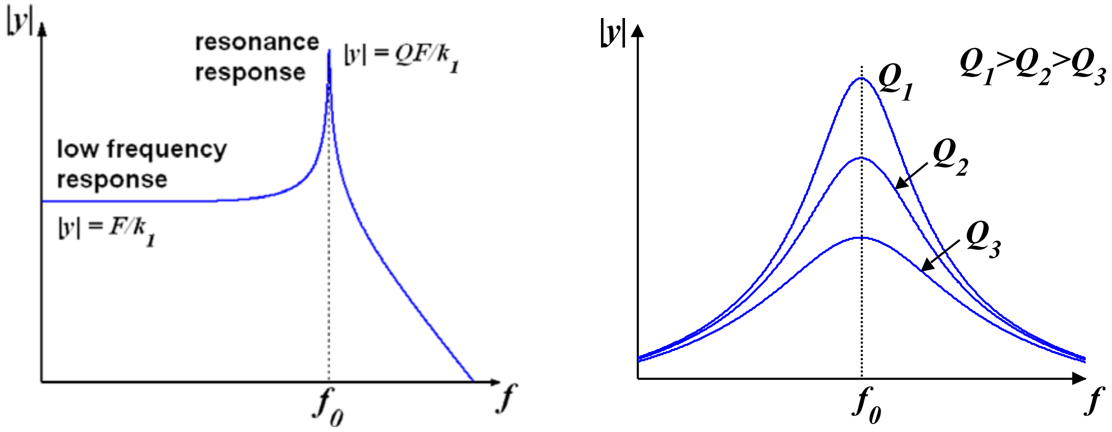

(a) *(b)*

Figure 2.2 (a) Amplitude-frequency response of a typical micromechanical resonator (b) amplitude-frequency responses with different quality factors.

As shown in Eq. (2.2), the quality factor Q is an important qualifier of micromechanical resonators as it determines the sharpness of the resonance (Fig. 2.2 (b)). A high quality factor leads to large vibration amplitude and improves the resolution of the resonator. Besides Eq. (2.4), there are another two equivalent Q definitions. One of them is commonly used in direct measurement whose expression is:

$$Q = \frac{f_0}{\Delta f_{3dB}} \tag{2.5}$$

where Δf_{3dB} refers to the bandwidth at 3dB below the resonance peak.

The other Q definition is the ratio of the total energy stored per cycle E_{stored} to the energy dissipated per cycle $E_{dissipated}$ (Hao Z L, 2003):

$$Q = 2\pi \frac{E_{stored}}{E_{dissipated}} \tag{2.6}$$

Eq. (2.6) tells that to achieve a high quality factor, the stored energy should be maximized while the dissipated energy should be minimized.

2.2 Nonlinear model of micromechanical resonators

2.2.1 Nonlinear equation of motion

During the derivation of Eq. (2.1), it is assumed that the vibration amplitude is small and hence the resonator is operated in the linear regime. However, for large vibration amplitudes, additional terms must be included in Eq. (2.1) to account for the nonlinear relationship between the spring force and displacement. Including these additional terms, the nonlinear equation of motion (Duffing's equation) of a micromechanical resonator becomes (Landau L D, 1999; Quévy E, 2003):

$$m\frac{d^2y}{dt^2} + \gamma\frac{dy}{dt} + k_1 y + k_2 y^2 + k_3 y^3 = F\cos\left(2\pi ft\right) \tag{2.7}$$

where k_2 and k_3 are the effective quadratic and cubic nonlinear spring constants, respectively.

According to Landau (Landau L D, 1999), the response of Eq. (2.7) exhibits an amplitude-dependent resonant frequency f_0' whose value can be solved using the successive approximation method:

$$f_0' = f_0 + \kappa Y_{0,f_0'}^2 \tag{2.8}$$

where $Y_{0,f_0'}$ is the vibration amplitude at f_0' and κ is a nonlinear parameter determined by the nonlinear spring constants:

$$\kappa = \frac{3k_3}{8k_1} f_0 - \frac{5k_2^2}{12k_1^2} f_0 \tag{2.9}$$

Eq. (2.8) indicates that the orientation of the resonant frequency shift is determined by κ: a negative κ causes the resonance to tilt to a lower frequency, showing the "spring softening effect" whereas a positive κ results in a higher resonant frequency, showing the "spring hardening effect". These effects are illustrated in Fig. 2.3.

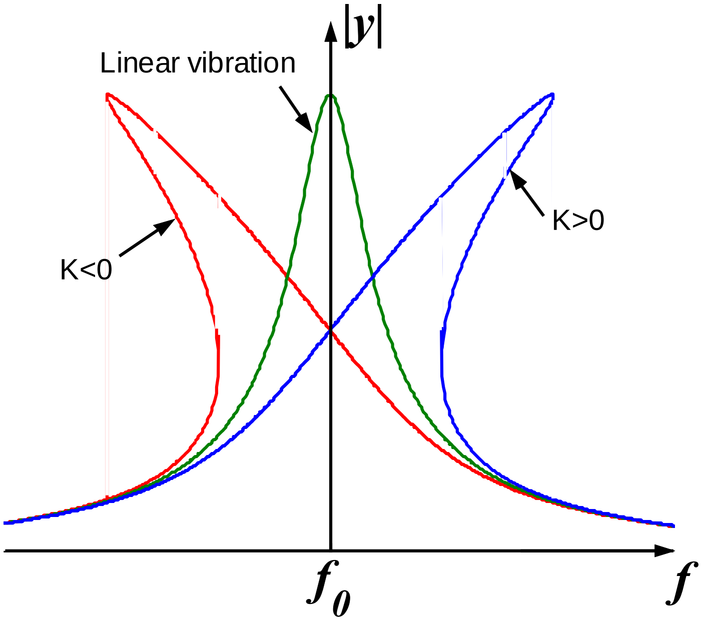

Figure 2.3 The effect of nonlinearities on the resonant frequency.

Furthermore, Eq. (2.8) shows that the amount of frequency shift is proportional to the square of the vibration amplitude at resonance. Increasing the vibration amplitude causes further bending in the amplitude-frequency response curve and eventually leads to the abrupt “jump phenomenon” due to the frequency hysteresis, as shown by BCDE region in Fig. 2.4. When the hysteresis occurs, sweeping the frequency forward gives the response curve ABCD and sweeping backward yields curve DEBA. Hence, an important test of whether the nonlinear vibration is present is to sweep through a resonance in both directions. Without nonlinear vibration, the two response curves are identical. It should be noted in Fig. 2.4 that the middle curve CE corresponds to the unstable state which cannot be observed in the open-loop amplitude-frequency measurement. Any small disturbance will cause the operating point to jump from CE curve to either BC or DE curve. However, some recent work demonstrates that if the resonator is part of a closed-loop oscillator circuit with appropriate phase feedback, stable vibration is achievable at any point along the amplitude-frequency curve including CE (Greywall D S, 1994; Yurke B, 1995). More detailed discussions of the resonator stability can be found in (Yurke B, 1995).

In practice, the critical vibration amplitude Y_C at the onset of frequency hysteresis is defined as the nonlinear limit for the micromechanical resonator. Above Y_C the nonlinear multi-valued frequency hysteresis is triggered whereas below Y_C is the linear hysteresis free region, as shown in Fig. 2.4. The value of Y_C is given by (Landau L D, 1999):

$$Y_C = \frac{F_C}{k_1} Q = \sqrt{\frac{4 f_0}{3\sqrt{3}\kappa Q}} \tag{2.10}$$

where F_C is the magnitude of the critical applied harmonic force:

$$F_C = \sqrt{\frac{64\sqrt{3}\pi^4 m^2 f_0^5}{9|\kappa| Q^3}} \tag{2.11}$$

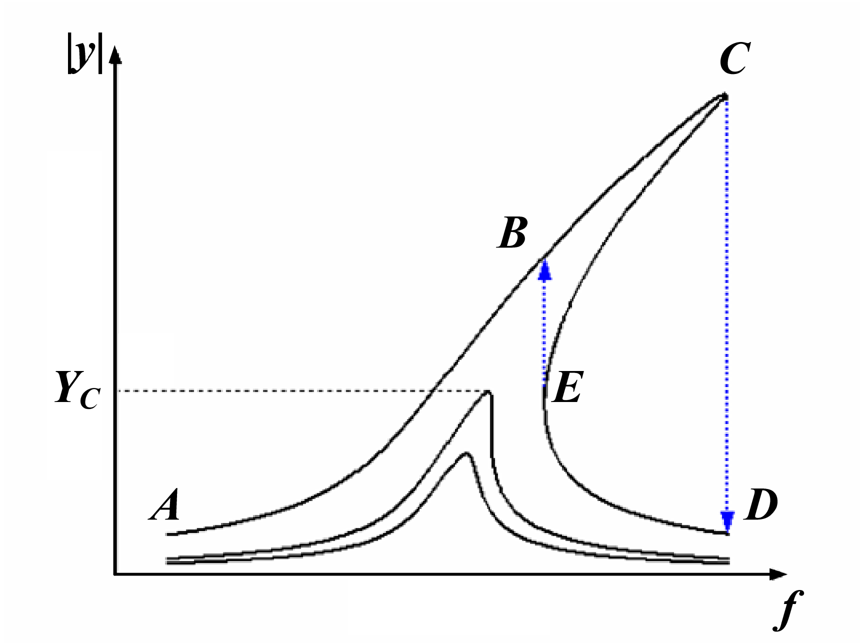

Figure 2.4 Amplitude-frequency response curves for a typical micromechanical resonator. At large vibration amplitudes, the response curve shows hysteresis.

For a capacitively driven and sensed micromechanical resonator, the interaction between the mechanical restoring force and electrostatic driving force governs the overall dynamics of the device. As a result, the nonlinearities in the resonator can have both mechanical and electrostatic components which need to be analyzed separately.

2.2.2 Mechanical nonlinearities

Mechanical nonlinearities arise from both geometrical (area and volume change) and material effects of the resonator (Kaajakari V, 2004b). Since both effects are determined by the intrinsic device properties, mechanical nonlinearities can differ a lot for different types of resonators. Specifically, for most of the flexural mode beam resonators, the dominant mechanical nonlinearities are the geometrical effects resulting from the beam extension during vibration. The extended beam introduces additional stress to the structure, leading to the spring hardening effects (Younis M I, 2003; Greywall D S, 2005). On the other hand, the nonlinearities in bulk mode resonators are much more complicated. This is because for bulk mode resonators such as longitudinal beams and extensional squares (Kaajakari V, 2004b), the geometrical effects could be very small and hence the material effects (i.e. nonlinear Young's modulus) have to be included in the analysis as well.

For resonator structures designed to be symmetric for both positive and negative displacement (which is usually the case), the quadratic nonlinear spring constant can be ignored and the nonlinear mechanical force is given by:

$$F_m = -k_{1m} y - k_{3m} y^3 \tag{2.12}$$

where k_{1m} and k_{3m} are the linear and cubic mechanical spring constants, respectively.

One common method to extract k_{1m} and k_{3m} from a resonator is to perform the force-large displacement simulation using finite-element-modeling (FEM) softwares such as ANSYS or ABAQUS (Lamminmaki T, 2000). During the simulation, a force is applied to one side of the resonator. Then, the values of k_{1m} and k_{3m} can be extracted by fitting the force versus displacement relationship using Eq. (2.12). Despite the convenience of the method, the accuracy of FEM-calculated spring constants is usually limited around 60% to 70% due to various non-ideal effects such as distributed force (Bannon F D, 2000), variations in the modulus of elasticity (Kaajakari V, 2004b), process imperfection (Miller D C, 2007), etc.. Moreover, the accuracy is further degraded for resonator structures whose dynamic mode shapes differ from their corresponding static deflection profiles. To further investigate this, the modal and static simulations were performed in ANSYS for two flexural mode resonators: the clamped-clamped beam (Yongchul A, 2001) and free-free beam resonators (Hsu W T, 2001).

As shown in Fig. 2.5, the two displacement profiles match reasonably well for the clamped-clamped beam resonator. However, for the free-free beam resonator, its vibration mode shape deviates from the static displacement, especially in the portion between its hinges and the beam ends. Because of this deviation, the dynamic spring constants of the free-free beam resonator cannot be accurately characterized by the force-large displacement analysis.

Although it is possible to constrain the static deformation of the structure to its dynamic mode shape during the FEM analysis, the error in extracting k_{1m} and k_{3m} still remains around 60% (40% accurate) (Kinnell P K, 2004). Hence, a more accurate technique is needed to characterize and model the nonlinear spring constants of the resonator.

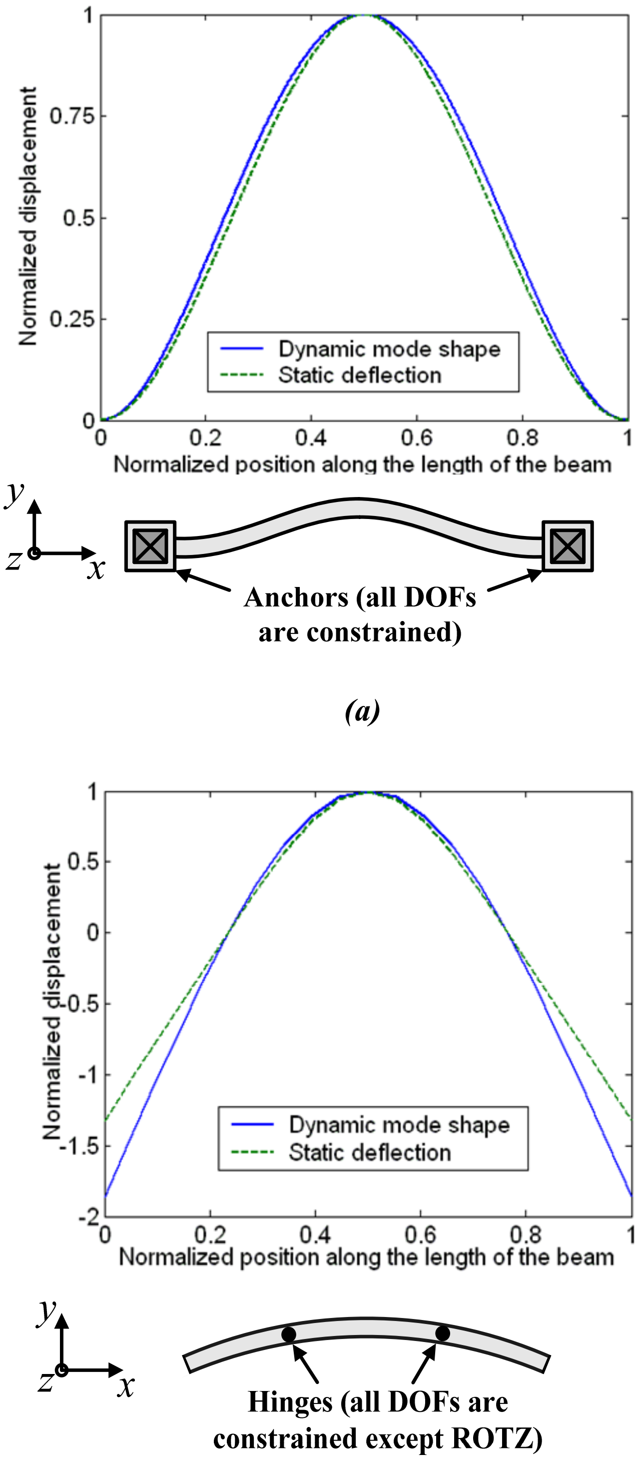

(a)

(b)

Figure 2.5 Normalized vibration mode shape and static deflection profile: (a) clamped-clamped beam resonator (b) free-free beam resonator.

2.2.3 Electrostatic nonlinearities

Unlike intrinsic mechanical nonlinearities, electrostatic nonlinearities are the external effects arising from the inverse relationship between the displacement and capacitance. Fig. 2.6 presents the schematic of a typical parallel-plate actuator. Assuming a small displacement y of the resonator, the net electrostatic force F_e is given by:

$$F_e = \frac{1}{2}\varepsilon_0 W_e h\left[\frac{V_P^2}{\left(d-y\right)^2} - \frac{\left(V_P - v_{ac}\right)^2}{\left(d+y\right)^2}\right] \tag{2.13}$$

where $\varepsilon_0 = 8.854\times10^{-12}\,F/m$ is the permittivity of free space.

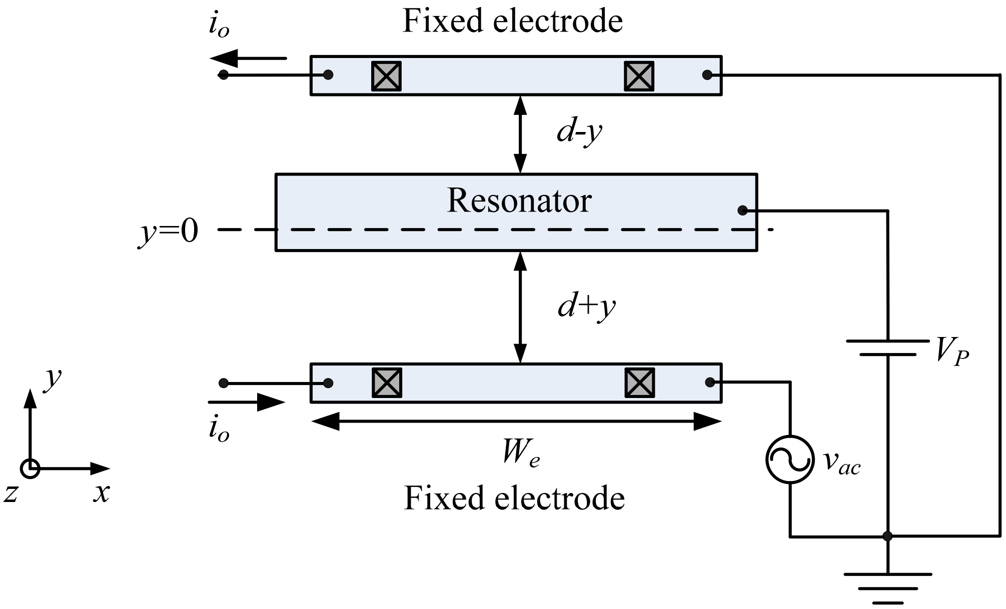

d = nominal gap between the resonator and fixed electrode
W_e = electrode width
h = structure thickness
v_{ac} = input AC excitation voltage
V_P = polarization voltage (voltage between the resonator and fixed electrodes)
i_o = output current resulting from the vibration of the resonator

Figure 2.6 Schematic of a parallel-plate actuator.

For $y \ll d$, Eq. (2.13) can be expanded into a Taylor series near y = 0 as follows (up to third order):

$$F_e = \frac{1}{2}\frac{\varepsilon_0 W_e h}{d^2}\left[2V_P v_{ac} - v_{ac}^2 + \frac{2}{d}\left(2V_P^2 - 2V_P v_{ac} + v_{ac}^2\right)y + \frac{3}{d^2}\left(2V_P v_{ac} - v_{ac}^2\right)y^2 \right. \\ \left. + \frac{4}{d^3}\left(2V_P^2 - 2V_P v_{ac} + v_{ac}^2\right)y^3\right] \tag{2.14}$$

With the simultaneous assumption of $\left|v_{ac}\right| \ll V_P$, Eq. (2.14) can be further simplified as:

$$F_e = \underbrace{\frac{\varepsilon_0 W_e h}{d^2} V_P v_{ac}}_{F_{e,harmonic}} + \underbrace{\frac{2\varepsilon_0 W_e h}{d^3} V_P^2 y + \frac{4\varepsilon_0 W_e h}{d^5} V_P^2 y^3}_{F_{e,spring}} \tag{2.15}$$

In Eq. (2.15), the first term $F_{e,harmonic}$ is the harmonic driving force while the second and third terms are functions of the displacement and they represent the electrostatic spring force $F_{e,spring}$. From the expression of $F_{e,spring}$, the linear and cubic electrostatic spring constants can be recognized as:

$$k_{1e} = -\frac{2\varepsilon_0 W_e h}{d^3} V_P^2 \tag{2.16}$$

$$k_{3e} = -\frac{4\varepsilon_0 W_e h}{d^5} V_P^2 \tag{2.17}$$

The negative sign of k_{1e} and k_{3e} indicates that the electrostatic spring force acts in a direction to displace the resonator further. Hence, in the absence of positive spring constant, the resonator will snap into either of the fixed electrodes once it is disturbed from the equilibrium center position.

Including k_{1e}, the expression of the resonant frequency (Eq. (2.3)) can be rewritten as:

$$f_0 = \frac{1}{2\pi}\sqrt{\frac{k_{1m} + k_{1e}}{m}} = \frac{1}{2\pi}\sqrt{\frac{k_{1m} - \frac{2\varepsilon_0 W_e h}{d^3} V_P^2}{m}} \tag{2.18}$$

where k_{1m} is the linear mechanical spring constant whose value is fixed after fabrication. However, applying different polarization voltage V_P effectively changes k_{1e}. Hence, the resonant frequency can be tuned by changing V_P for desired operation. Such technique is known as the "frequency tuning effect" and it is practically used for post-fabrication fine tuning (Palaniapan M, 2002) and temperature compensation (Ho G K, 2005; Ho G K, 2006).

As for the negative cubic electrostatic spring constant k_{3e}, it causes the spring softening effect which leads to the bending of the amplitude-frequency response curve to lower frequency side, as shown in Fig. 2.3.

In order to combine the effects of both mechanical and electrostatic spring constants, k_m's and k_e's should be summed up and thus Eq. (2.7) becomes:

$$m\frac{d^2y}{dt^2}+\gamma\frac{dy}{dt}+\underbrace{\left(k_{1m}+k_{1e}\right)}_{k_1}y+\underbrace{\left(k_{3m}+k_{3e}\right)}_{k_3}y^3=F\cos\left(2\pi ft\right)=\frac{\varepsilon_0 W_e h}{d^2}V_P v_{ac} \tag{2.19}$$

where the quadratic nonlinear spring constant k_2 is ignored with the assumption of a symmetric resonator structure.

Besides the cubic spring constant, the parallel plate configuration results in the distortion of the output current i_o as well. The expression of i_o is given by:

$$\begin{aligned} i_0 &= V_P\frac{dC}{dt}=\frac{\varepsilon_0 W_e h}{d^2}V_P\left(1+\frac{2}{d}y+\frac{3}{d^2}y^2+\ldots\right)\frac{dy}{dt} \\ &= \underbrace{\left(\frac{\varepsilon_0 W_e h}{d^2}V_P\right)\frac{dy}{dt}}_{\text{fundamental}}+\underbrace{\left(\frac{2\varepsilon_0 W_e h}{d^2}V_P\right)\frac{y}{d}\frac{dy}{dt}}_{\text{second harmonic}}+\underbrace{\left(\frac{3\varepsilon_0 W_e h}{d^2}V_P\right)\left(\frac{y}{d}\right)^2\frac{dy}{dt}}_{\text{fundamental and third harmonic}}+\ldots \end{aligned} \tag{2.20}$$

Thus, even linear displacement y leads to higher order harmonics. Nevertheless, since only the fundamental amplitude-frequency response is studied in this work and the second and third terms in Eq. (2.20) are much smaller in magnitude than the first term due to the small y/d, $(y/d)^2$ ratios, we will simply take the first term to calculate the output current i_o.

In addition to the parallel-plate actuator, there are also cases where linear electrostatic force and output current are required. In such cases, the comb-finger actuator can be used, as shown in Fig. 2.7.

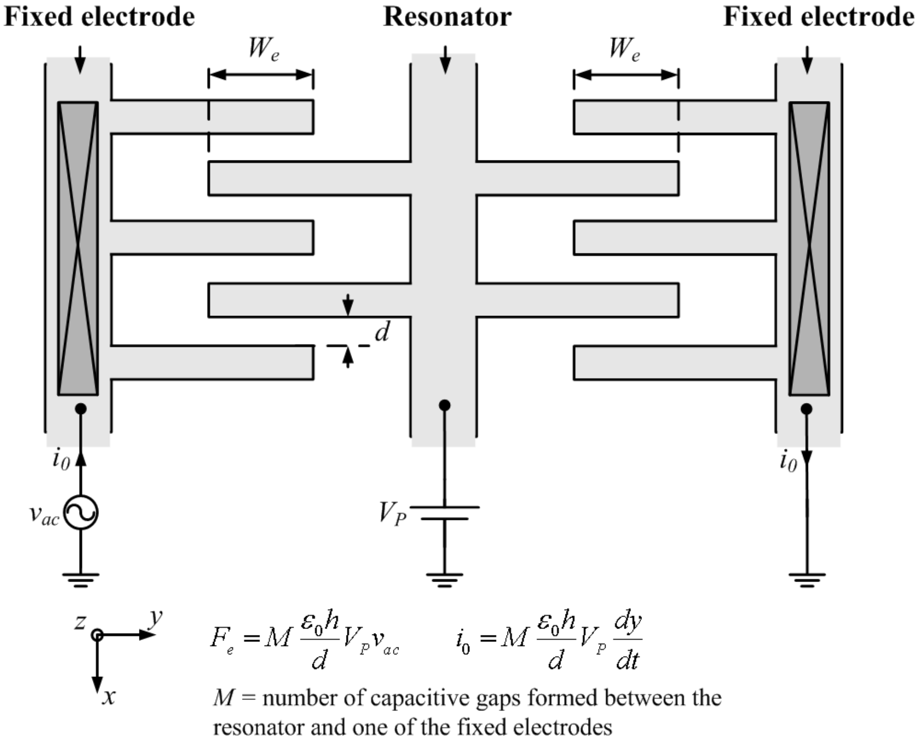

$$F_e = M\frac{\varepsilon_0 h}{d}V_P v_{ac} \qquad i_0 = M\frac{\varepsilon_0 h}{d}V_P\frac{dy}{dt}$$

M = number of capacitive gaps formed between the resonator and one of the fixed electrodes

Figure 2.7 Schematic of a comb-finger actuator.

Compared with the parallel plate, the comb-finger actuator has much lower transduction efficiency (i.e. F_e and i_o) and much larger mass, both severely limiting the resonant frequency of the device. Hence, comb-finger actuators are less used nowadays.

2.2.4 Quality factors

Another important parameter related to the nonlinear vibration is the quality factor Q (or equivalently, the damping coefficient γ). It has been reported that at very large vibration amplitude, the nonlinearities not only adjust the resonant frequency, but also alter the structural damping and Q (Roessig T A, 1998). However, a quantitative predictive model is not available yet and once the resonator is driven into the nonlinear regime, it becomes very difficult to determine Q based on the bandwidth at 3dB below the resonance peak (Eq. (2.5)). Therefore, alternative means to define the equivalent quality factor for nonlinear vibration is required.

As shown in Fig. 2.8, there are two response curves obtained under different driving conditions. When the applied harmonic force is small, the vibration remains linear and the vibration amplitude at resonance is given by:

$$Y_L = \frac{F_L}{k_1} Q_L \tag{2.21}$$

where Q_L and F_L are the quality factor and magnitude of the applied harmonic force under linear vibration, respectively. In case of nonlinear vibration, the vibration amplitude at resonance becomes:

$$Y_N = \frac{F_N}{k_1} Q_N \tag{2.22}$$

where Q_N and F_N are the quality factor and magnitude of applied harmonic force under nonlinear vibration.

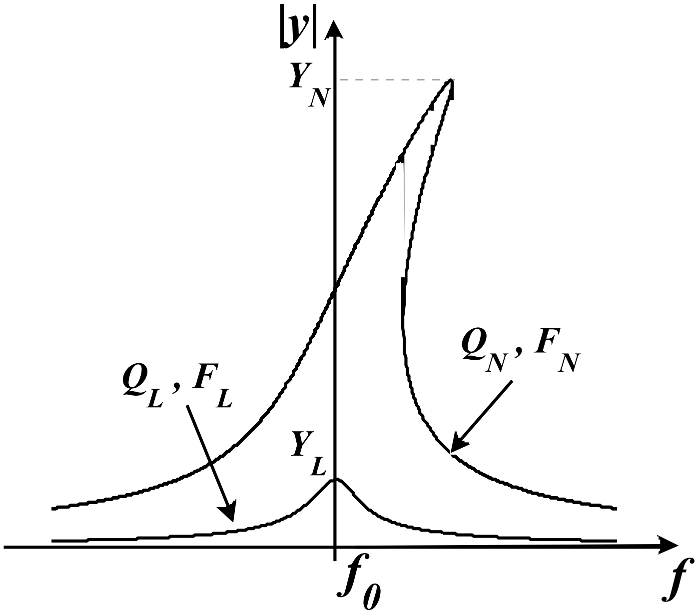

Figure 2.8 Quality factor variation under different driving conditions.

Combining Eqs. (2.21) and (2.22), Q_N is related to Q_L as follows:

$$Q_N = Q_L \frac{F_L}{F_N} \frac{Y_N}{Y_L} \tag{2.23}$$

On the right hand side of Eq. (2.23), the first term Q_L can be obtained using the 3dB bandwidth measurement (Eq. (2.5)). The second term F_L/F_N can be calculated by comparing the $V_P v_{ac}$ products (Eq. (2.15)) and the third term Y_N/Y_L can be calculated by comparing the output currents according to Eq. (2.20). Hence, although Q_N cannot be measured directly, its value can be estimated from other measurable parameters.

2.3 Effects of nonlinearities on the resonator performance

So far, the mathematical model of micromechanical resonators has been constructed. In this section, we will look into two major effects of nonlinearities on the resonator performance, namely: (1) amplitude-induced frequency fluctuation and (2) power handling limitation.

2.3.1 Amplitude-induced frequency fluctuation

As mentioned earlier in Chapter 2.2.1, the direct impact of nonlinearities on the resonator performance is to change the resonant frequency according to the vibration amplitude. To quantify this effect, an amplitude-frequency coefficient α is introduced to the following expression:

$$\frac{\Delta f_0}{f_0}=\frac{f_0'-f_0}{f_0}=\frac{\kappa Y_{0,f_0'}^2}{f_0}=\alpha\left|i_{o,f_0'}\right|^2 \qquad (2.24)$$

where $i_{o,f_0'}$ is the output current at resonance f_0' and it is a good indicator of the vibration amplitude, according to Eq. (2.20). Substituting Eqs. (2.9), (2.17) and (2.20) into Eq. (2.24), α can be expressed as:

$$\alpha \doteq \underbrace{\frac{3k_{3m}d^4}{128\pi^4 f_0^4 m\varepsilon_0^2 W_e^2 h^2 V_P^2}}_{\alpha_m}+\underbrace{\left(-\frac{3}{32\pi^4 f_0^4 d m\varepsilon_0 W_e h}\right)}_{\alpha_e} \qquad (2.25)$$

where the first term α_m is attributed to the cubic mechanical spring constant and the second term α_e is attributed to the cubic electrostatic spring constant. For resonators with mechanical spring hardening effect (i.e. k_{3m}>0), their α_m's are positive, bending the resonance to higher frequency side. On the other hand, the softening effect from the electrostatic nonlinearities always bends the resonance to lower frequency side. Hence, it is desirable to operate the resonator in an intermediate region where the mechanical spring hardening effect and electrostatic spring softening effect cancel out, making the resonant frequency independent of the vibration amplitude to the first order, as shown in Fig. 2.9.

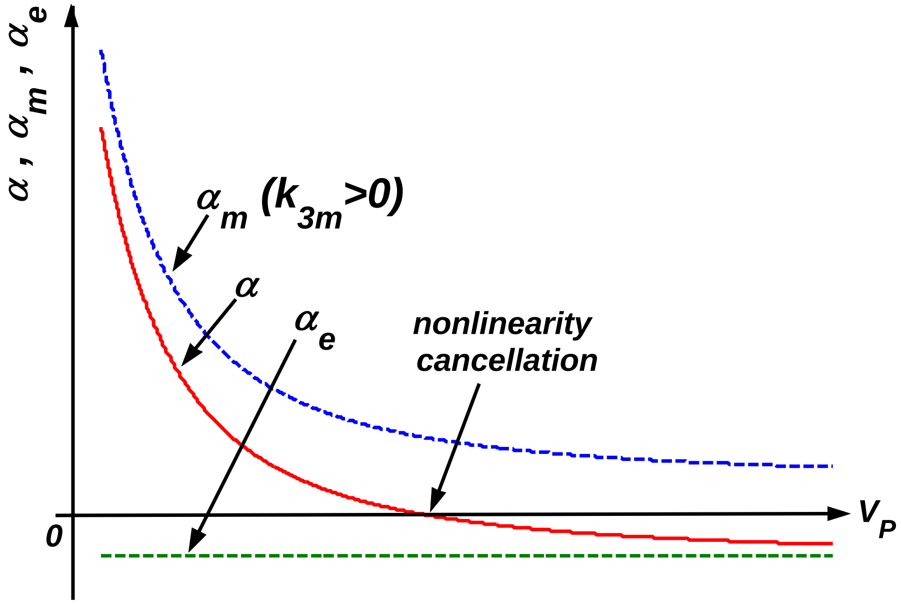

Figure 2.9 Relationship between the amplitude-frequency coefficient and the polarization voltage.

The operating point for nonlinearity cancellation can be solved by equating Eq. (2.25) to zero:

$$\alpha = \alpha_m + \alpha_e = 0 \Rightarrow V_P = \sqrt{\frac{k_{3m} d^5}{4\varepsilon_0 W_e h}} \tag{2.26}$$

2.3.2 Power handling limitation

The second impact of nonlinearities on the resonator performance is to limit the power handling capability. In order to illustrate the importance of power handling capabilities for micromechanical resonators, it is useful to review the *Leeson's* equation, which models the phase noise-to-carrier ratio in an ideal linear resonator-based oscillator (Lee T H, 1998; Kaajakari, 2005):

$$L(\Delta f) = 10\log\left[\frac{kT}{\pi f_0}\frac{Q}{E_{stored}} + \frac{kTf_0}{4\pi\Delta f^2}\frac{1}{QE_{stored}}\right] \tag{2.27}$$

where

k = Boltzmann's constant ($1.38\times10^{-23} J\cdot K^{-1}$),

T = absolute temperature,

E_{stored} = vibration energy stored in the resonator and

Δf = frequency offset.

In Eq. (2.27), the first term represents the noise floor and the second term represents the near carrier noise. As shown, the near carrier noise can be reduced by increasing either E_{stored} or Q. However, the increase in Q will deteriorate the noise floor (first term) which should be compensated by increasing E_{stored} as well. In this respect, achieving both high E_{stored} and high Q are equally important. For quartz crystals, storing enough energy without being operated in the nonlinear regime is generally not an issue due to the large physical size. In contrast, the micron-sized micromechanical resonators have to be driven close to the nonlinear limits for sufficient energy levels (Kaajakari V, 2004b). Beyond the nonlinear limits, the low-frequency noise aliasing will increase which severely degrades the oscillator phase noise performance (Lee S, 2004; Kaajakari V, 2005). The maximum storable energy of the resonator prior to frequency hysteresis is given by:

$$E_{stored}^{\max} = \frac{1}{2}kY_C^2 = \frac{1}{2}k_1Y_C^2 + \frac{1}{2}k_3Y_C^4 \tag{2.28}$$

For weak nonlinear resonators studied in this work, the second term is much smaller in magnitude than the first term and thus Eq. (2.28) can be further simplified as:

$$E_{stored}^{\max} = \frac{1}{2}k_1Y_C^2 = \frac{16k_1^2}{9\sqrt{3}Qk_3} \tag{2.29}$$

Eq. (2.29) shows that in order to maximize $E_{stored}^{\max}$, it is important to characterize and reduce the resonator nonlinearities (i.e. k_3).

2.4 Summary

In this chapter, we have introduced both linear and nonlinear equations of motion of micromechanical resonators. Three key parameters of nonlinear resonators: mechanical nonlinearities, electrostatic nonlinearities and quality factors have been analyzed and modeled mathematically. In addition, we have investigated the effects of nonlinearities on the resonator performance. It is shown that nonlinearities not only destabilize the resonant frequencies, but also limit the maximum storable energy of the resonator. Based on the theoretical results, in the next chapter, we will propose a novel characterization and modeling technique and its use in the study of nonlinearities in flexural mode resonators.

Chapter 3 Nonlinearity in flexural mode resonators

This chapter will investigate the nonlinearities in flexural mode micromechanical resonators. Both free-free (abbreviated as “ff”) beam and clamped-clamped (abbreviated as “cc”) beam resonators will be studied. A semi-analytic technique will be proposed to characterize and model the device nonlinearities. Different from the conventional finite-element-modeling (FEM) based method whose accuracy is limited around 60% to 70%; the proposed technique is capable of accurately extracting both the resonator’s mechanical and electrostatic nonlinear parameters from just a few preliminary experimental observations. The nonlinear model constructed using these extracted parameters can be used to predict the resonator behavior under different driving conditions and further reveal the intrinsic nonlinear properties of the resonator.

3.1 Free-free beam micromechanical resonators

This section presents the nonlinear behavior of a fundamental-mode and a second-mode ff beam resonators. Design details of the ff beam resonators are described in section 3.1.1, followed by fabrication and resonator characterization in section 3.1.2 and 3.1.3, respectively. In section 3.1.4, the simulation results are provided and compared with the measured values and a brief summary is given in section 3.1.5.

3.1.1 Resonator design

Fig. 3.1(a) presents the top view of a capacitively driven and sensed 700 kHz, fundamental-mode ff beam micromechanical resonator with the typical bias, driving and off-chip sensing configuration. As shown, the resonator is designed to vibrate in the lateral flexural mode, with its nodal locations being suspended by four flexural support beams (Hsu W T, 2001; Palaniapan M, 2006). The two support beams on opposite sides of the ff beam (from anchor to anchor) form a composite cc beam which resonates in the second mode with its frequency designed at the fundamental-mode frequency of the ff beam. With such configuration, the coupling between the ff beam and composite support cc beams is minimized and hence the energy loss from the ff beam through the support beams to the anchors is reduced, allowing the resonator to achieve a high quality factor. From the fundamental mode shape obtained from ANSYS simulation, as shown in Fig. 3.1(b), the displacement at the nodal points is verified to be close to zero.

Fig. 3.2(a) gives the top view schematic of a 600 kHz, second-mode ff beam resonator, which is also realized in this work. This resonator is similar to the fundamental-mode one, except that it is longer for a given resonant frequency and has three nodal points. At each nodal point, the ff beam is held in place by just one support beam (half of the composite cc beam). The use of fewer support beams is to further reduce the energy losses (Demirci M U, 2003b). The ANSYS simulated vibration mode shape is shown in Fig. 3.2(b). To preferentially excite the second vibration mode and suppress the spurious modes, the two drive electrodes are phase shifted by 180 degrees during the operation.

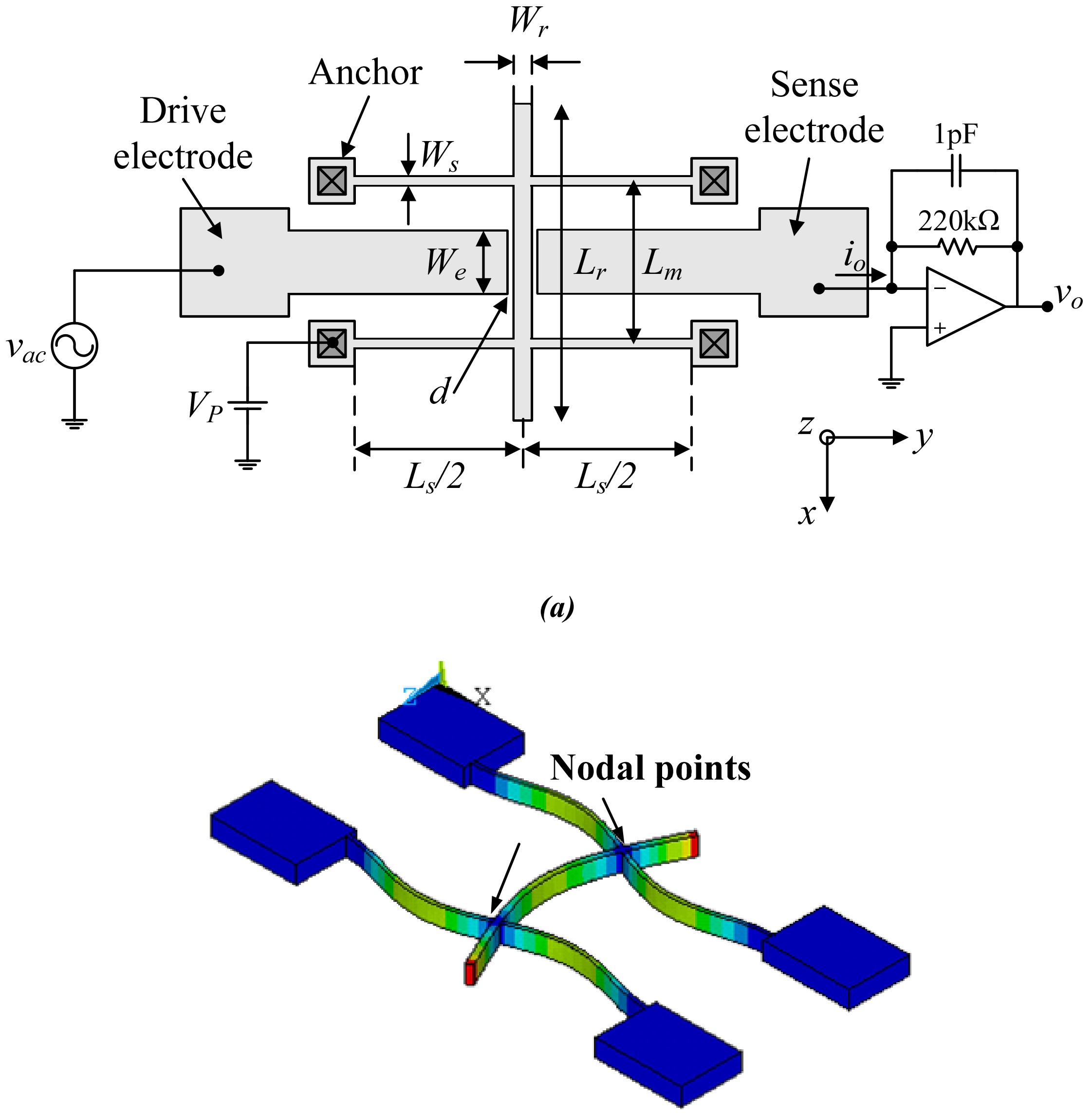

(a)

(b)

Figure 3.1 (a) Top view schematic of a fundamental-mode ff beam microresonator in a typical bias, excitation and sensing configuration (b) the flexural vibration mode shape of a fundamental-mode ff beam microresonator obtained via ANSYS simulation.

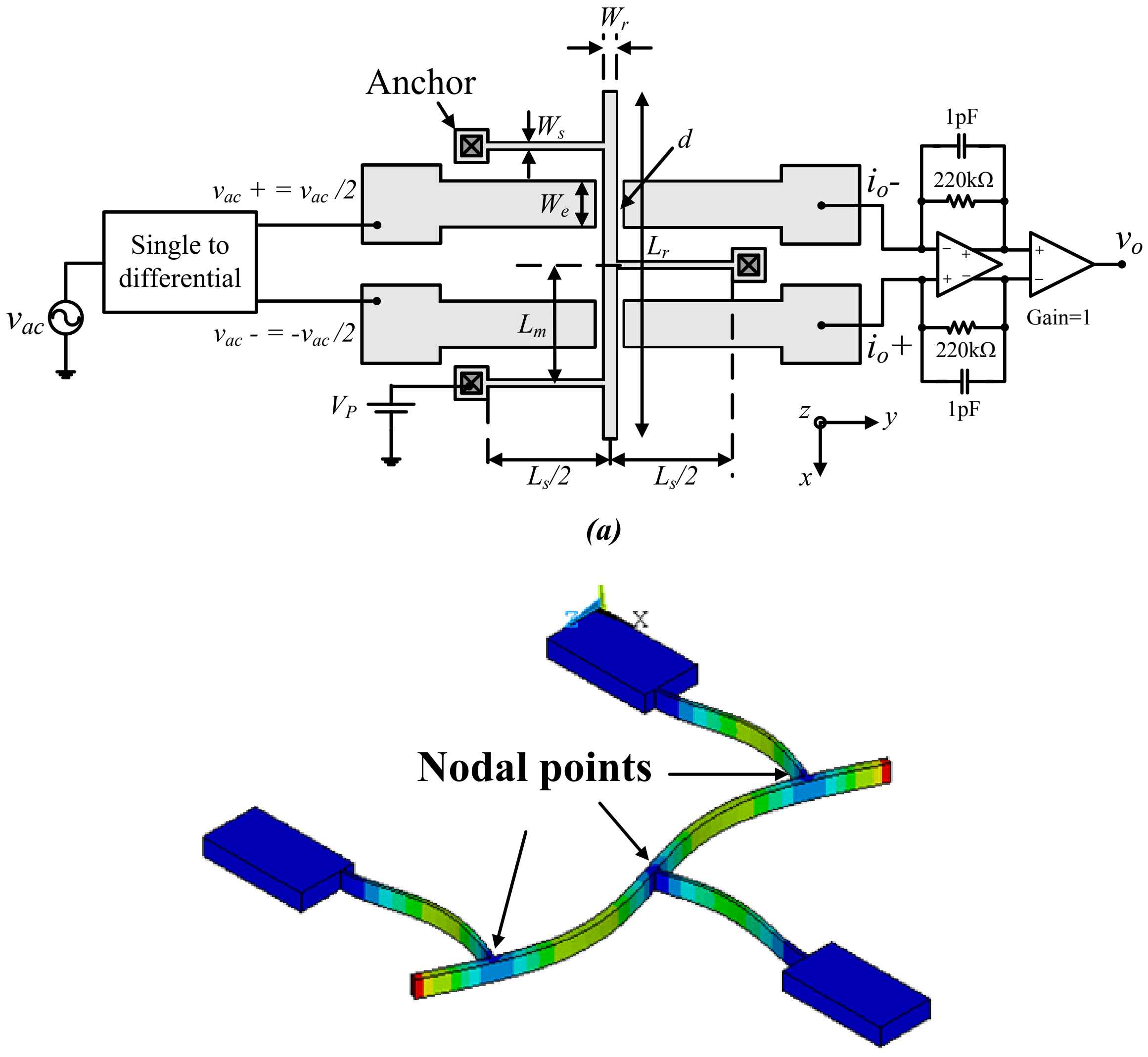

(a)

(b)

Figure 3.2 (a) Top view schematic of a second-mode ff beam microresonator in a typical bias, excitation and sensing configuration (b) the flexural vibration mode shape of a second-mode ff beam microresonator obtained via ANSYS simulation.

The nominal resonant frequency of the ff beam follows the well-known *Euler-Bernoulli* equation as (Demirci M U, 2003b):

$$f_0 = \frac{1}{2\pi\sqrt{12}}\left(\beta_n L_r\right)^2 \sqrt{\frac{E}{\rho}}\frac{W_r}{L_r^2} \tag{3.1}$$

where

E = Young's modulus,

ρ = density of the structural material,

L_r = length of the ff beam resonator,

W_r = width of the ff beam resonator and

β_n = mode coefficient.

For the fundamental and second modes of vibration, $\beta_1 L_r$ and $\beta_2 L_r$ are 4.73 and 7.853, respectively (Demirci M U, 2003b).

Once the resonant frequency of the ff beam is fixed, the composite support cc beams are designed to vibrate in the second mode with the same frequency as the ff beam. To achieve this, the length of the support beams L_s should satisfy (Demirci M U, 2003b):

$$L_s = 1.683\left[\sqrt{\frac{E}{\rho}}\frac{W_s}{f_0}\right]^{1/2} \tag{3.2}$$

where W_s is the width of the support beams.

As for the nodal points, their locations can be determined by evaluating the mode shape equation. According to Timoshenko (Timoshenko S, 1974), the n^{th} vibration mode shape of a ff beam is:

$$y_{\mathrm{mode}}(x) = \cosh\beta_n x + \cos\beta_n x - \xi\left[\sinh\beta_n x + \sin\beta_n x\right] \tag{3.3}$$

where $y_{mode}(x)$ is the displacement in the y direction at location x (refer to Figs. 3.1(a) and 3.2(a) for axis definition), and

$$\xi = \frac{\cosh\beta_n L_r - \cos\beta_n L_r}{\sinh\beta_n L_r - \sin\beta_n L_r}$$

At the nodal points, ideally no translational motion occurs (i.e. $y_{mode}(x)|_{\text{nodal point}}=0$).

Table 3.1 lists the design parameters and layout data for the two ff beam resonators, with reference to the dimensions indicated in Figs. 3.1(a) and 3.2(a). As shown in Table 3.1, for both resonators, the ANSYS-calculated resonant frequencies of the whole structures (ff beam and support beams) agree well with the theoretical values of the *Euler-Bernoulli* equation (ff beam only), confirming the decoupling between the ff beam and the support beams.

Table 3.1 FF beam design and layout parameters.

Parameter	**Vibration mode of the ff beam**	
	Fundamental	***Second***
Target frequency, [kHz]	700	600
FF beam length, L_r [µm]	320	650
FF beam width, W_r [µm]	8	10
Support beam length, L_s [µm]	420	470
Support beam width, W_s [µm]	5	5
Support beam separation, L_m [µm]	170	235
Beam thickness, h [µm]	25	25
Electrode width, W_e [µm]	140	185
Resonator to electrode gap, d [µm]	2	2
Young's modulus, E [GPa]	170	170
Poisson's Ratio, v	0.28	0.28
Density, ρ [kg/m^3]	2330	2330
ANSYS-calculated resonant frequency, [kHz]	708.9	586.1
Euler-Bernoulli frequency, [kHz]	685.9	572.8

3.1.2 Fabrication

The fundamental-mode and second-mode ff beam resonators were fabricated using the commercially available SOIMUMPs process (Miller K, 2004). This SOI micromachining process provides several unique advantages for resonator fabrication. Fig. 3.3 presents a cross sectional view of this process and parameters of different layers.

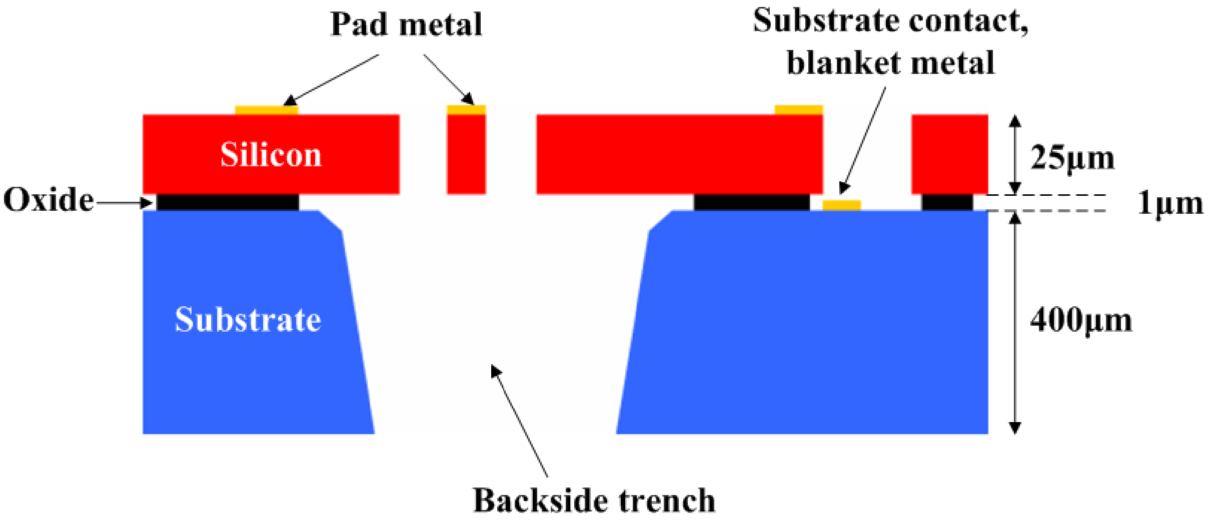

Film	Thickness (µm)			Sheet Resistance or resistivity		
	Min.	Typ.	Max.	Min.	Max.	Units
Pad metal	0.47	0.52	0.57	0.045	0.065	Ω/□
Silicon	24	25	26	6	10	Ω/□
Oxide	0.95	1.00	1.05	N/A		
Substrate	395	400	405	1	10	Ω-cm
Blanket metal	0.58	0.65	0.72	0.035	0.055	Ω/□

Figure 3.3 Cross Sectional view and parameters of different layers for SOIMUMPs.

As shown, the SOIMUMPs process starts with a silicon-on-insulator (SOI) wafer which consists of either a 10 μm or 25 μm top structural silicon layer, a 1 μm oxide layer, and a 400 μm substrate layer. The top silicon layer is lithographically patterned and deep reactive ion etched (DRIE) to define the mechanical structures. In this work, the 25 μm structural layer is used because the thick structure layer not only pushes the undesirable out-of-plane resonant modes to higher frequencies, but also facilitates larger electrical transduction signals. Next, the wafer is selectively backside-etched through the substrate layer to make trenches. These trenches help to release the movable structures in the top silicon layer and suppress the substrate parasitics. There are totally two types of metal available in the process: the "pad metal" used for fine electrical interconnections and the "blanket metal" used for large metal blocks such as the substrate contact. The pad metal, consisting of 20 nm of chrome and 500 nm of gold, is patterned through a liftoff process while the blanket metal, consisting of 50 nm Cr+ and 600 nm Au, is deposited using a shadow masking technique. The minimum feature size of the top silicon layer is 2 μm, and hence the electrode gap is limited to 2 μm as well. Fig. 3.4 presents the scanning electron micrographs (SEMs) of the fabricated 700 kHz fundamental-mode and 600 kHz second-mode ff beam resonators. To prevent the reduction in the quality factor from interconnection ohmic loss (Yongchul A, 2001; Bhave S A, 2005), all the electrodes are coated with pad metal whose average sheet resistance is as low as 0.055 ohm/sq.

3.1.3 Resonator characterization

After device fabrication, some preliminary measurements were carried out to characterize the linear spring constant, lumped mass and cubic nonlinear spring constant of the

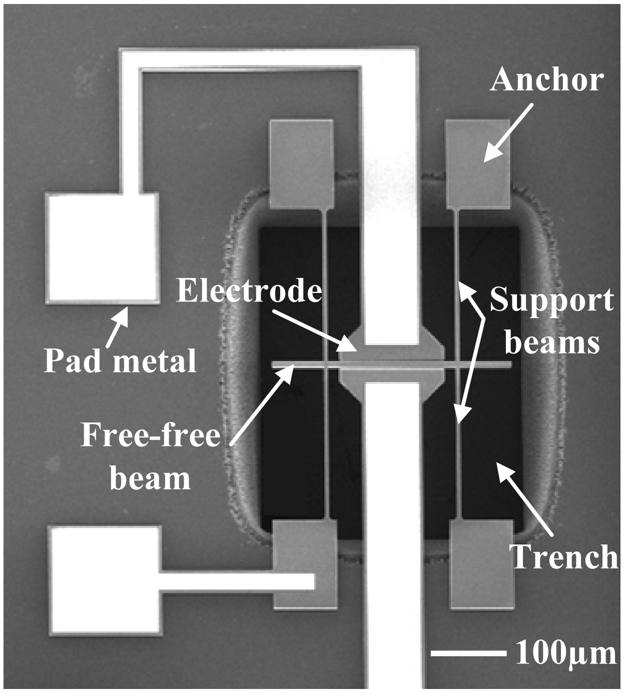

(a)

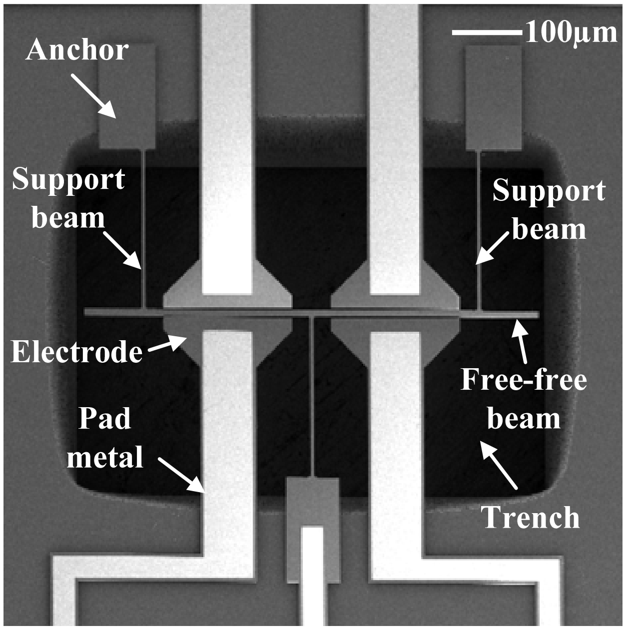

(b)

Figure 3.4 SEM of a: (a) fundamental-mode ff beam resonator (b) second-mode ff beam resonator.

fundamental-mode and second-mode ff beam resonators. The procedure of the experimental work involves the following three steps:

1) operating the resonator under linear vibration; changing the DC polarization voltage V_P to obtain the relationship between f_0 and V_P ; fitting the experimental data with the linear mechanical spring constant and lumped mass (Eq. (2.18)),

2) driving the resonator into nonlinear regime; adjusting both AC and DC voltages; plotting the Δf_0 versus $Y^2_{0,f_0'}$ curve to determine the nonlinear parameter κ for each V_P, and

3) translating κ into k_3, extracting both the cubic mechanical and electrostatic nonlinear spring constants from the relationship between k_3 and V_P.

Each of the three steps will be discussed in detail. Experimental results will be presented separately for the two resonators.

(a) Fundamental-mode ff beam resonator

During the measurement, the die containing the fundamental-mode ff beam resonator was mounted on a printed circuit board and placed in a custom-built vacuum chamber with air pressure of 37.5 μTorr. The bias, driving and sensing of the resonator was set up according to Fig. 3.1(a). The SOI substrate was grounded to minimize the parasitic effects (Nguyen C T C 1991). The resonator was characterized using a Bode 100 vector network analyzer and S-parameter test set.

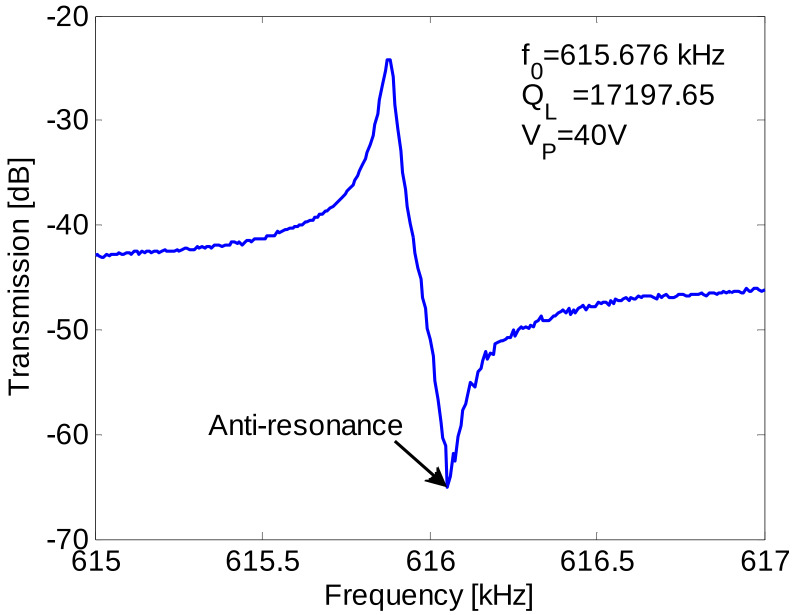

Figure 3.5 Measured S21 transmission for a 615 kHz fundamental-mode ff beam resonator.

Fig. 3.5 presents the S21 transmission frequency response curve for the fundamental-mode ff beam resonator with a DC polarization voltage of V_P= 40V. As shown, besides the upward resonance peak, the transmission curve also contains a downward anti-resonance which is caused by the feed-through current between the drive and sense electrodes (Nguyen C T C, 1991). In order to suppress the anti-resonance, the feed-through current must be separated from the output current. This separation can be done either in the time domain using the gated-sinusoid excitation and detection method or in the frequency domain using the electromechanical amplitude modulation method (Nguyen C T C, 1991). Due to process variations, the measured resonant frequency is 615.676 kHz, 10.2% off the designed value and the quality factor is Q_L=17197.65.

Pursuant to extracting the linear spring constant k_1 and the lumped mass m, Fig. 3.6 plots the relationship between measured resonant frequency f_0 and V_P.

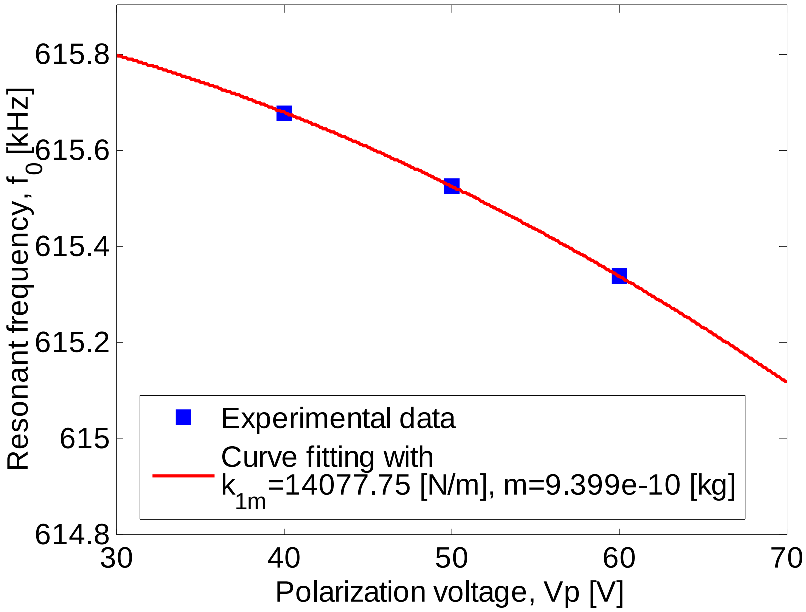

Figure 3.6 Plot of resonant frequency f_0 versus V_P for the fundamental-mode ff beam resonator.

As Fig. 3.6 shows, the resonant frequency decreases as V_P increases, exhibiting the frequency tuning effect. By fitting the experimental data with Eq. (2.18), the linear mechanical spring constant is found to be k_{1m}=14077.75 N/m and lumped mass m=9.399×10^{-10} kg. Strictly speaking, Eq. (2.18) is not accurate enough to model the frequency tuning effect because of two reasons. Firstly, the process variations in defining W_e, h and d are ignored. Secondly, the parallel plate approximation neglects the distributed effects which also contribute some errors (Bannon F D, 2000). Nevertheless, these secondary effects are ignored here merely to simplify the formula. All the errors in k_{1e} will be absorbed by k_{1m} and m as a scaling factor and they do not affect the quantitative results. For the same reason, a fitting coefficient β is introduced to the cubic nonlinear spring constant k_3 as follows:

$$k_3 = k_{3m} + k_{3e} = k_{3m} - \beta \frac{4\varepsilon_0 W_e h}{d^5} V_P^2 \tag{3.4}$$

where β is included to account for the errors in defining k_{3e}. As shown by Eq. (3.4), the values of k_{3m} and β can be obtained by fitting the k_3 versus V_P relationship. Direct measurement of k_3 being difficult, its value can be estimated indirectly from the nonlinear parameter κ by Eq. (2.9). κ can be easily extracted from the slope of Δf_0 versus $Y_{0,f_0'}^2$ curve according to Eq. (2.8). $Y_{0,f_0'}$ is the vibration amplitude at resonance f_0' whose value is given by substituting $F_{e,harmonic}$ (Eq. (2.15)) into Eq. (2.22):

$$Y_{0,f_0'} = \left| \frac{F_{e,harmonic}}{k_1} Q_N \right| = \left| \frac{\varepsilon_0 W_e h}{d^2} \frac{Q_N}{k_1} V_P v_{ac} \right| \tag{3.5}$$

where Q_N is the equivalent quality factor under nonlinear vibration and its definition is provided in Eq. (2.23).

Based on Eq. (3.5), Fig. 3.7 shows Δf_0 as a function of $Y_{0,f_0'}^2$ for V_P=40, 50 and 60V. As expected from Eq. (2.8), the relationship between Δf_0 and $Y_{0,f_0'}^2$ is linear and the slope of the curve gives the nonlinear parameter $\kappa=3.751\times10^{16}$ Hz/m^2. Having identified κ, k_3 can be calculated from Eq. (2.9) to be 2285.05 μN/μm^3. For this fundamental-mode ff beam resonator, both κ and k_3 are constant values, regardless of the DC polarization voltage applied. This is unexpected, if k_3 is indeed a parabolic function of V_P (Eq. (2.19)). The only possible reason is $k_{3m} \gg k_{3e}$, suggesting that k_{3m} dominates the cubic nonlinear stiffness k_3. A rough estimation confirms that for V_P as high as 100V, $|k_{3e}|$ is just 38.7 μN/μm^3, 1.7% of k_3. Thus, k_{3e} can be ignored to simplify the modeling process without sacrificing too much accuracy.

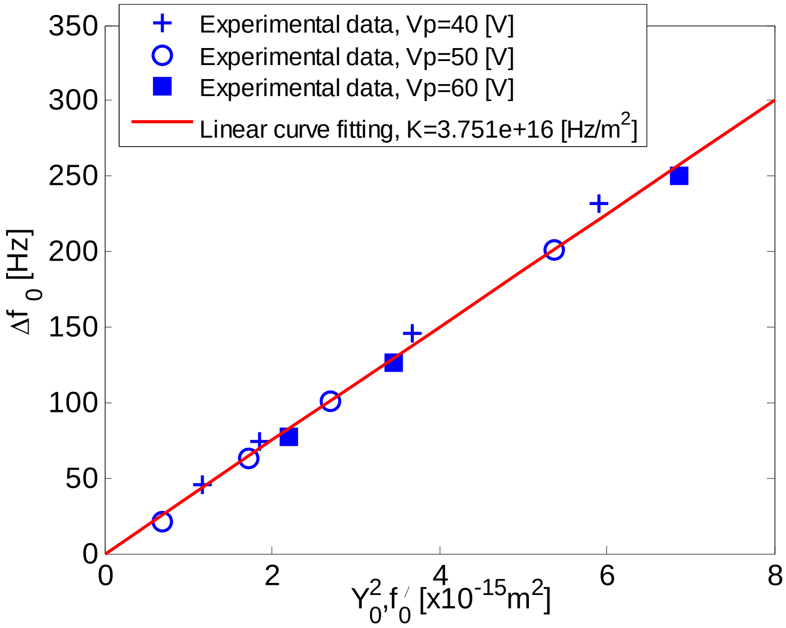

Figure 3.7 Relationship between Δf₀ and $Y^2_{0,f_0'}$ for the fundamental-mode ff beam resonator.

(b) Second-mode ff beam resonator

As for the second-mode ff beam resonator, its parameters can be characterized by following the same procedure as the fundamental-mode one. Fig. 3.8 presents the frequency response curve for the resonator with a DC polarization voltage V_P=40V. Due to the fully differential drive and sense configurations, the anti-resonance is largely suppressed (Bhave S A, 2005) and hence the transmission curve of the second-mode ff beam resonator is more symmetric than that of the fundamental-mode one. The linear mechanical spring constant and lumped mass of the resonator are obtained by fitting the

f_0 versus V_P relationship in Fig. 3.9. Their values are k_{1m}=6701.88 N/m and m=5.5374×10^{-10} kg.

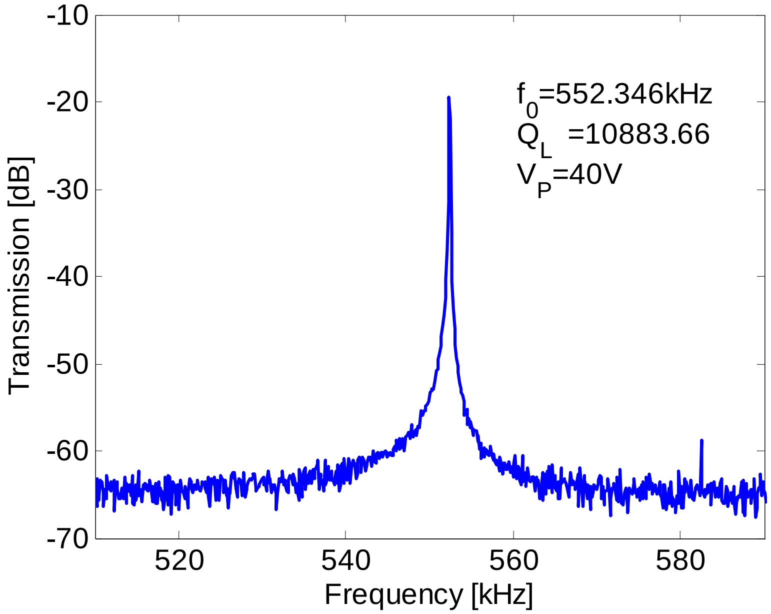

Figure 3.8 Measured S21 transmission for a 550 kHz second-mode ff beam resonator.

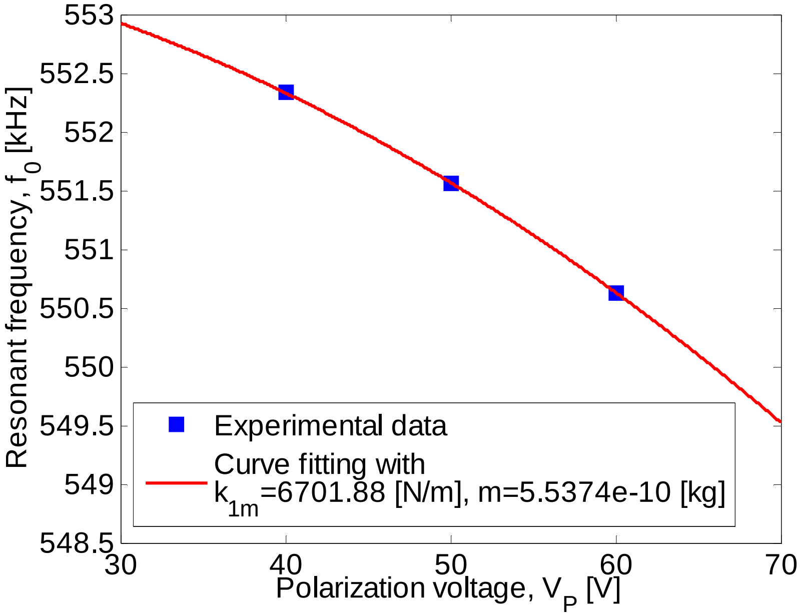

Figure 3.9 Plot of resonant frequency f_0 versus V_P for the second-mode ff beam resonator.

Fig. 3.10 presents the curve of Δf_0 versus $Y^2_{0,f_0'}$. Again, Δf_0 varies linearly with $Y^2_{0,f_0'}$. However, compared with Fig. 3.7, the slope of the curve is negative, meaning that the nonlinearities always shift the resonance to lower frequencies. According to Eqs. (2.8) and (2.9), κ, k_3 are negative numbers. Furthermore, different from the fundamental-mode case, the value of κ changes with the DC polarization voltage, indicating that the mechanical and electrostatic cubic nonlinear spring constants are comparable with each other.

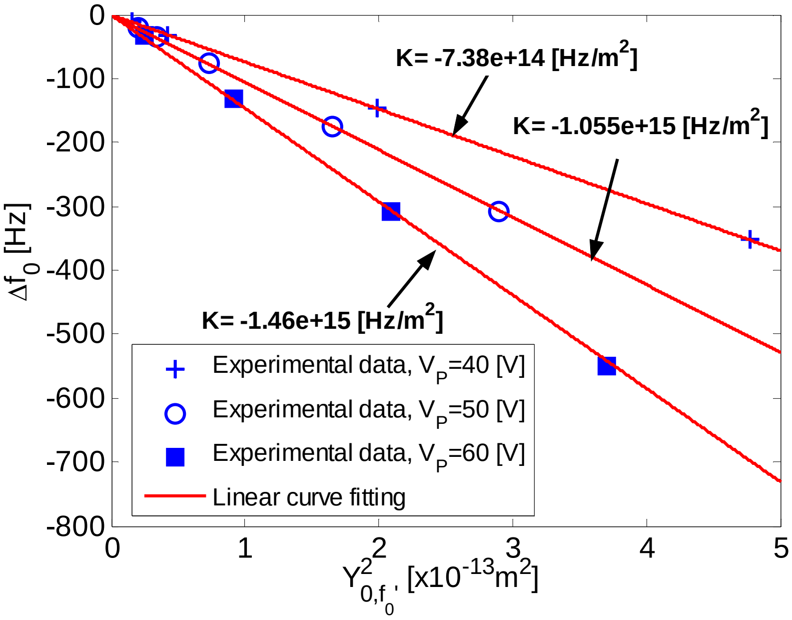

Figure 3.10 Relationship between Δf_0 and $Y^2_{0,f_0'}$ for the second-mode ff beam resonator.

In order to get a clear picture of how the effective cubic spring constant changes with V_P, κ is translated into k_3 via Eq. (2.9) and plotted in Fig. 3.11.

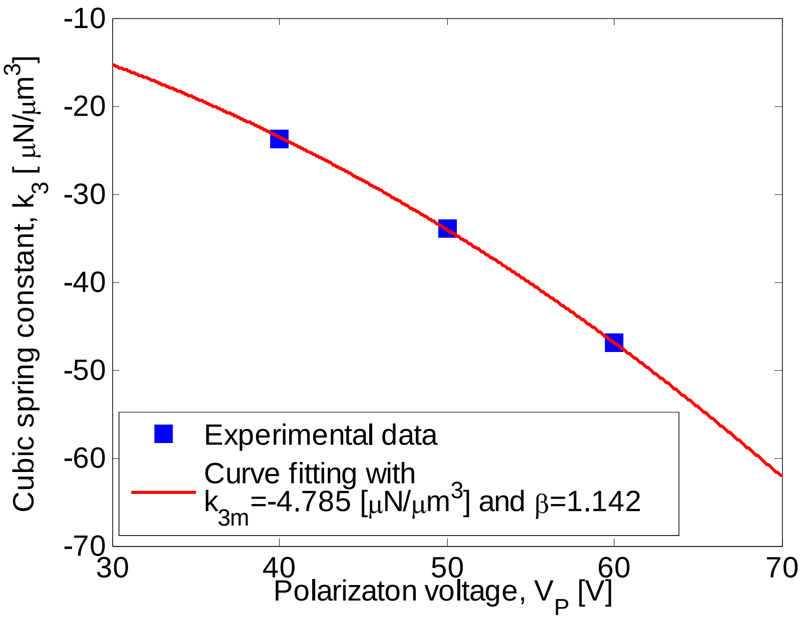

Figure 3.11 Plot of cubic spring constant k_3 versus V_P for the second-mode ff beam resonator.

As shown, the relationship between k_3 and V_P follows a square law. By fitting the curve with Eq. (3.4), k_{3m} is extracted to be -4.785 μN/μm^3 and β is 1.142.

It should be noted that k_{3m} of the second-mode ff beam resonator is negative and much smaller in magnitude than that of the fundamental-mode resonator. The difference in k_{3m} is attributed to the specific support beam design. As shown in Fig. 3.2, there is only one support beam at each nodal point of the second-mode ff beam. With less support beams, the nodal point is freer to move. This is believed to release most of the axial stiffening force in the beam, significantly reducing its k_{3m}. However, for the fundamental-mode ff beam resonator (Fig. 3.1), each of its nodal points is supported by two flexural beams. Hence, the axial stiffening force in the ff beam is maintained, resulting in a much larger k_{3m}. For further verification, the second-mode ff beam resonator was modified with totally six support beams (two support beams at each nodal point) and fabricated. This modified resonator has a much larger k_{3m} of 301.77 μN/μm^3 than its three-support-beam counterpart, confirming that k_{3m} can be changed by the specific support beam design.

Table 3.2 summarizes the experimentally extracted linear mechanical spring constant, lumped mass, cubic mechanical spring constant and fitting coefficient. (k_2 is ignored due to the symmetric structure of the ff beam) for each resonator. The ANSYS simulated parameters using force-large displacement analysis are also tabulated for comparison.

Table 3.2 Experimentally extracted and ANSYS calculated model parameters for the ff beam resonators.

Parameter	**Vibration mode of the ff beam**			
	Fundamental		***Second***	
	Experimental	**ANSYS simulated**	**Experimental**	**ANSYS simulated**
Linear mechanical spring constant, k_{1m} [N/m]	14077.75	3271	6701.88	3521
Lumped mass, m [$\times 10^{-10}$ kg]	9.399	1.649	5.5374	2.596
Cubic mechanical spring constant, k_{3m} [μN/μm^3]	$\approx k_3$=2285	16.39	-4.785	-0.525
Fitting coefficient, β	unimportant	N/A*	1.142	N/A*

* The fitting coefficient β is affected by the distributed effects and fabrication variations. Hence, its value cannot be obtained from ANSYS simulation.

As Table 3.2 displays, the two approaches contribute two sets of resonator parameters differing quite a lot from each other. This difference is mainly due to the deviation of the dynamic mode shape of the ff beam from its static deflection, as mentioned earlier in Fig. 2.5. To verify this, a cc beam resonator (length: 300 μm, width: 6 μm and thickness: 25

μm) was fabricated and characterized in the same way as the ff beam resonator. With the dynamic mode shape of the cc beam approximating its static deflection, the matching rates of k_{1m}, m and k_{3m} between the two sets of parameters are 76%, 71% and 59%, respectively (100% for perfect matching), which are much closer than the ff beam resonator. Hence, it can be concluded that the mismatch between the experimentally extracted and ANSYS simulated ff beam parameters is mainly due to the difference between its dynamic mode shape and static deflection. Moreover, for the fundamental-mode ff beam resonator, the simulated k_{3m} is smaller than the one from the experiment by more than two orders of magnitude. The small value of simulated k_{3m} is contrary to the observation of k_{3m} domination in Fig. 3.7. Because of this mismatch, the experimentally extracted parameters were used for all the simulations to be discussed in the next section.

3.1.4 Simulation versus experiments

All the model parameters listed in Table 3.2 were extracted from the preliminary experimental results at V_P=40, 50 and 60V. In this section, simulation results will be provided to predict the nonlinear behavior of the ff beam resonator under different driving conditions (i.e. V_P>60V). Here, the numerical simulation approach was used and the governing nonlinear equation of motion (Eq. (2.19)) was solved in Matlab.

For comparison, the simulated large-signal frequency responses for the fundamental-mode ff beam resonator are presented in Fig. 3.12 together with the measured ones. The frequency was swept forwards and backwards in the measurement to determine the hysteresis range. As shown, under two different driving conditions, the abrupt amplitude jumps seen in the experiments are accurately reproduced by the simulation. However, it

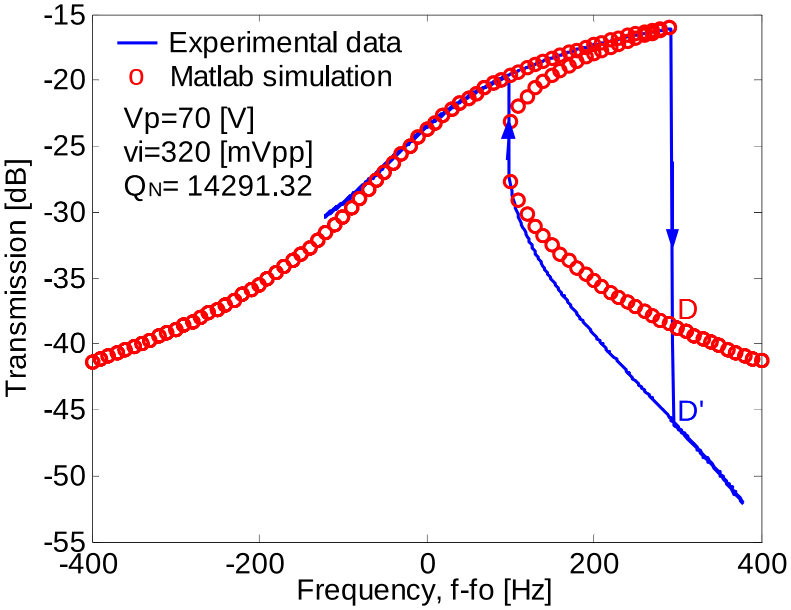

(a)

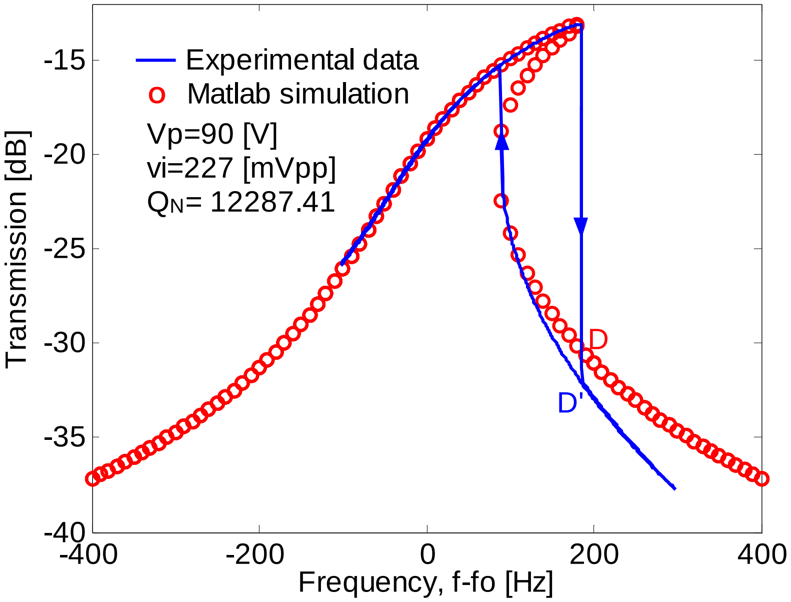

(b)

Figure 3.12 Measured and simulated S21 transmissions for the fundamental-mode ff beam resonator with input level: (a) V_P=70V, v_{ac}=320mV_{PP} and (b) V_P=90V, v_{ac}=227mV_{PP}.

is observed that the simulated curve deviates from the measured one at point D and D'. This is due to the fact that the feed-through capacitance was ignored in the simulation. As a result, the anti-resonance pulls point D downwards to D'. To include the effect of feed-through capacitance, the Matlab code needs to be revised; or the equivalent-circuit simulation method can be used (Veijola T, 2001). Another observation is that the quality factor Q decreases from 14291.32 at $V_P = 70$V to 12287.41 at $V_P = 90$V. The reduction in Q is believed to be the combined effects of increased energy losses from the ff beam to the composite support beams due to the frequency mismatch (Hsu W T, 2001), the structural damping and the loading effects (Yongchul A, 2001; Ho G K, 2005; Pourkamali S, 2007).

Fig. 3.13 presents the experimental and simulated results for the second-mode ff beam resonator. As shown, with the effect of feed-through capacitance being suppressed by the fully differential driving and sensing configurations, the simulated responses match the experimental results much better.

Besides the frequency response, Fig. 3.14 shows another comparison for critical driving conditions predicted by Matlab simulation and those measured from the experiments. (Critical driving conditions refer to the boundary determined by the combination of AC and DC voltages above which the multi-valued hysteresis response is triggered, and below which is the hysteresis-free region.) To simulate the critical driving conditions, another Matlab program was composed based on Eqs. (2.11) and (2.15). As shown in Fig. 3.14, the simulation agrees well with the measurement results for both the fundamental-

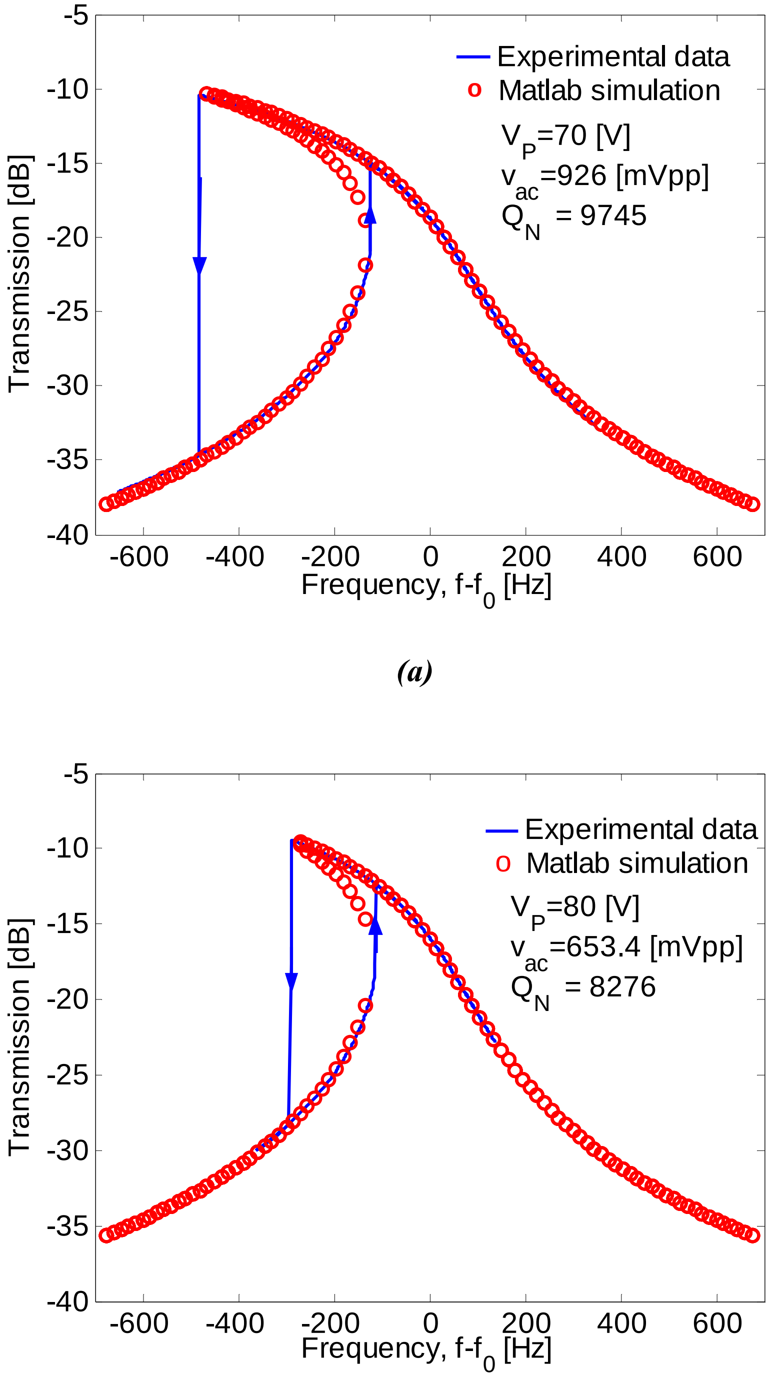

(a)

(b)

Figure 3.13 Measured and simulated S21 transmissions for the second-mode ff beam resonator with input level: (a) V_P=70V, v_{ac}=926mV_{PP} and (b) V_P=80V, v_{ac}=653.4mV_{PP}.

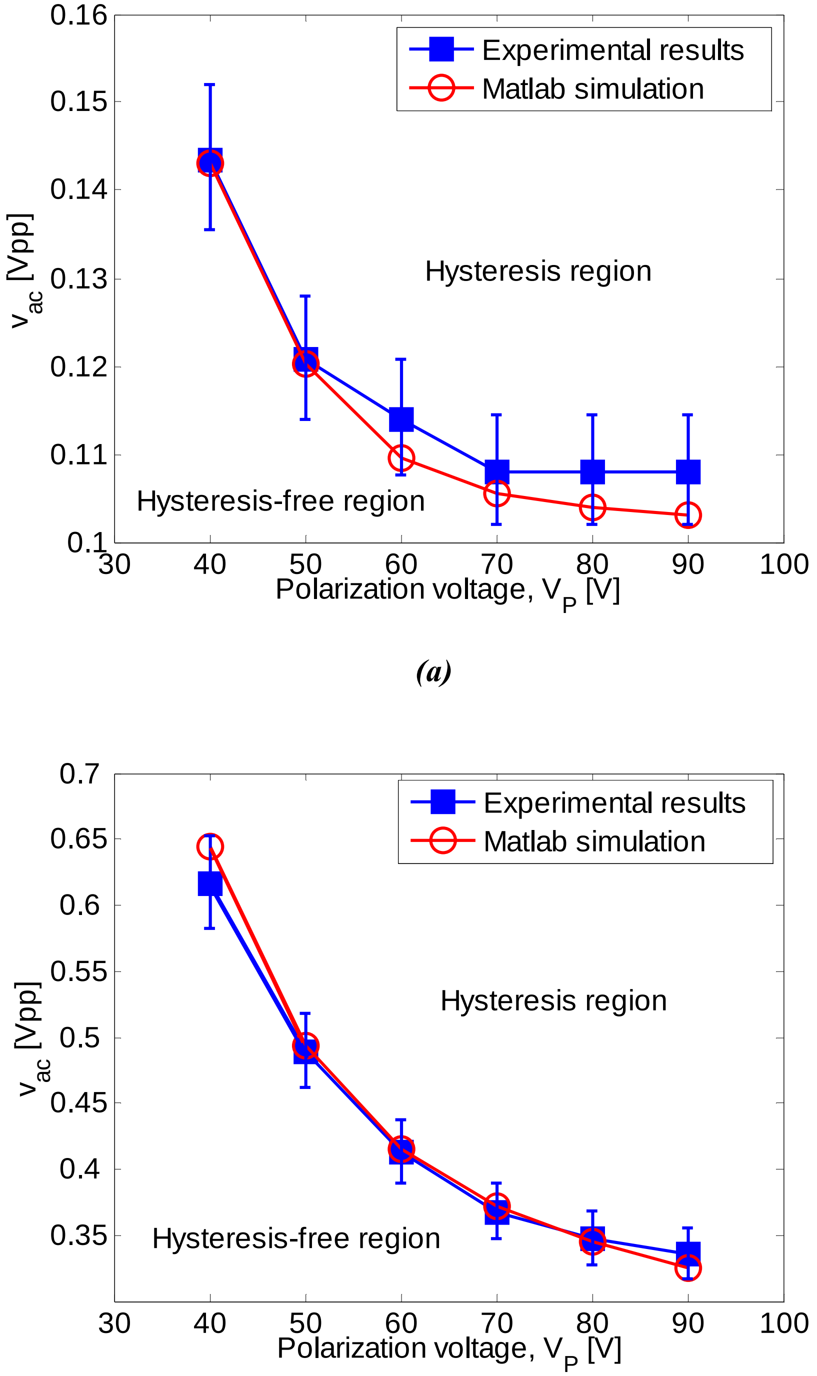

(a)

(b)

Figure 3.14 Measured and simulated nonlinear driving limits for the: (a) fundamental-mode ff beam resonator and (b) second-mode ff beam resonator. The error bars of the measurement are ±0.5dB.

mode and second-mode ff beam resonators, again confirming the reliability of the proposed modeling technique.

3.1.5 Summary

An effective semi-analytic characterization and modeling technique has been proposed to investigate the nonlinearities in the fundamental-mode and second-mode ff beam resonators. The proposed technique can be used to extract the accurate nonlinear model of the resonator from just a few preliminary measurement results. Both the nonlinear model and the experimental results conclusively show that for the fundamental-mode ff beam resonator, the cubic mechanical spring hardening effects dominate, shifting the resonance to higher frequencies. On the other hand, depending on the specific support beam design, the second-mode ff beam resonator can exhibit either spring hardening or softening behaviors. However, for the fundamental-mode ff beam resonator having the spring hardening effects, we were not able to observe the useful nonlinearity cancellation phenomenon because of the domination of k_{3m}. Hence, a cc beam resonator with small k_{3m} was intentionally designed to demonstrate the nonlinearity cancellation and all the results can be easily generalized to other resonators as well.

3.2 Clamped-clamped beam micromechanical resonators

3.2.1 Experimental results and discussion

Fig. 3.15 presents the SEM pictures of the cc beam resonator fabricated using the SOIMUMPs process. As shown, the cc beam was designed to be long and narrow to reduce the cubic mechanical spring constant k_{3m}, according to (Young W C, 2002):

$$k_{3m} = 12.18E\frac{W_r h}{L_r^3} \tag{3.6}$$

where W_r, h and L_r are the width, thickness and length of the cc beam, respectively.

With small k_{3m}, we expect to observe the spring hardening, softening as well as the useful nonlinear cancellation operation regimes.

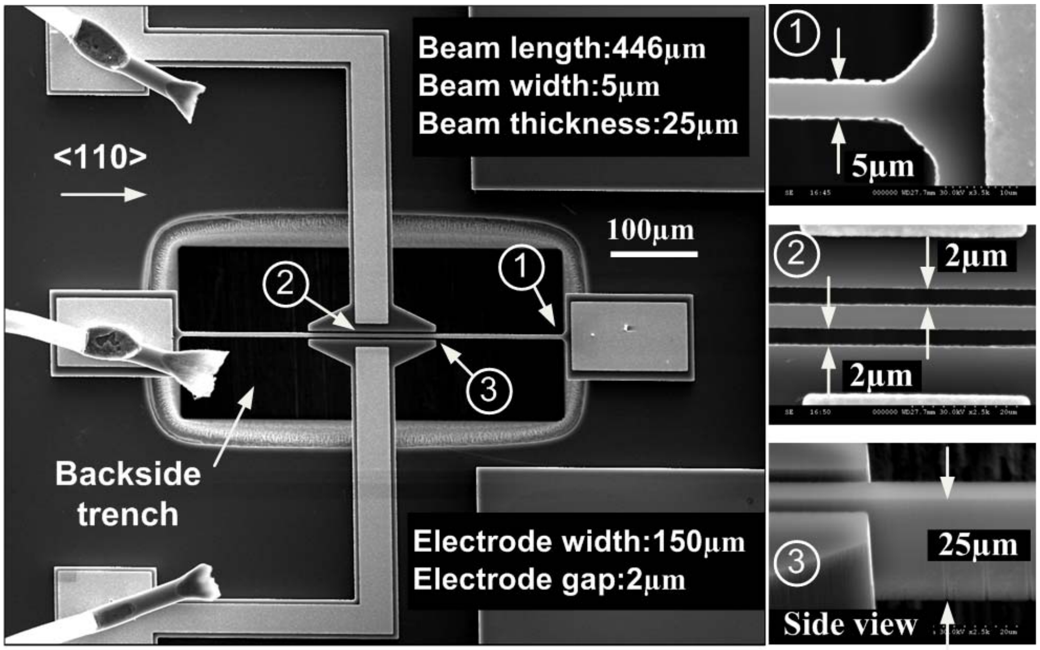

Figure 3.15 SEMs of the clamped-clamped beam resonator.

After device fabrication, the cc beam resonator was tested in vacuum using the standard two-port measurement setup, similar to Fig. 3.1(a). Fig. 3.16 presents the measured S21 transmission frequency response for the cc beam resonator with $V_P = 20$V. As shown, the resonant frequency of the cc beam centers around 194 kHz. This is comparable to the theoretical value of 213.57 kHz, which is calculated from (Bannon F D, 2000):

$$f_0 = \sqrt{\frac{E}{\rho}}\frac{W_r}{L_r^2} \tag{3.7}$$

The measured Q is around 6308 and it is much lower than that of the ff beam resonator. The low Q of the cc beam resonator is due to large vibration energy losses through the anchors to the substrate.

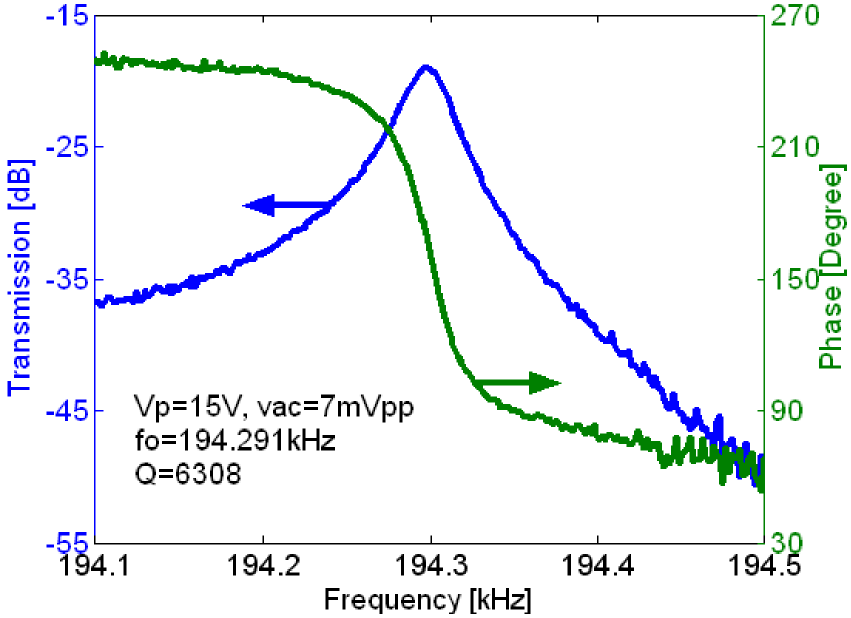

Figure 3.16 Measured S21 transmission for a 194 kHz cc beam resonator.

The almost symmetric shape of the frequency response, as shown in Fig. 3.16, was only observed at low AC actuation voltage of $v_{ac} = 7\text{mV}_{\text{PP}}$. Fig. 3.17 presents the frequency response curves of the resonator for fixed V_P at 20V and varying v_{ac}. As shown, for small

AC voltage of 47mV$_{PP}$, the response curve still remains single-valued. However, as v_{ac} is further increased, the curve keeps bending to higher frequencies, eventually showing the discontinuity due to frequency hysteresis at v_{ac}=75.6mV$_{PP}$ and 134mV$_{PP}$.

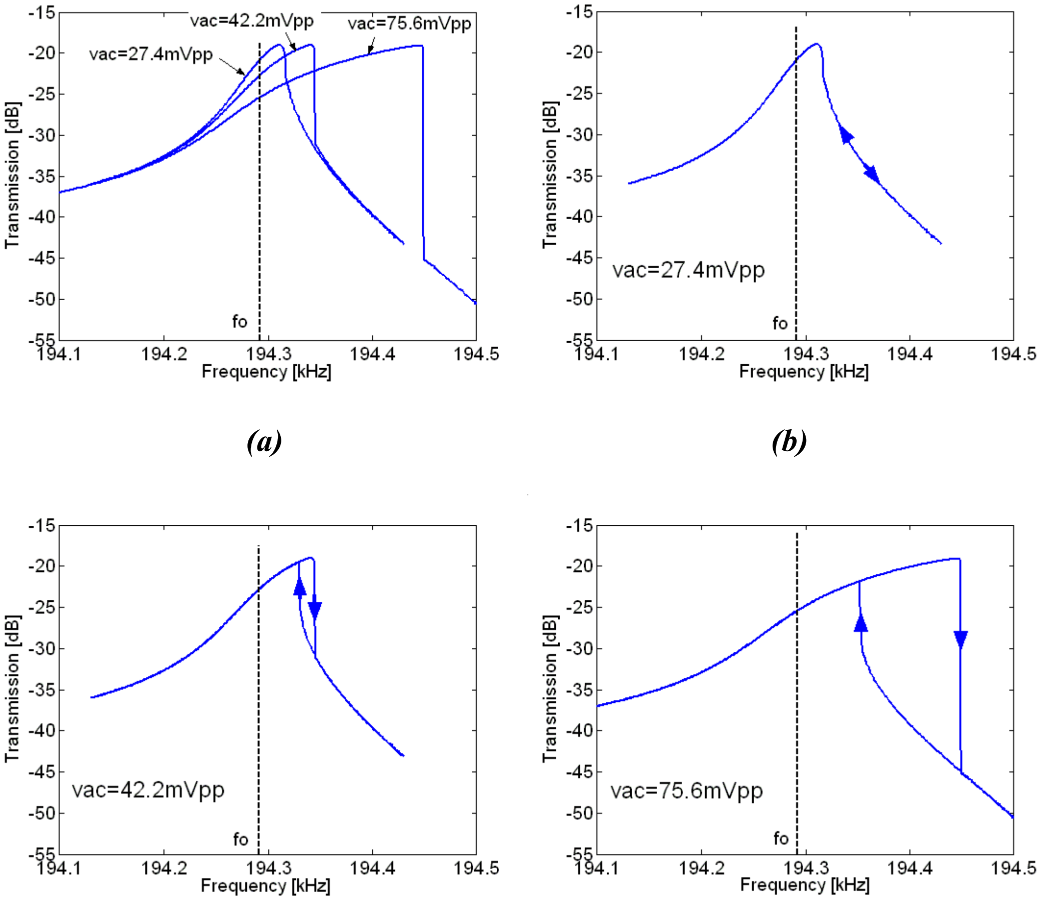

(a) *(b)*

(c) *(d)*

Figure 3.17 Measured S21 transmissions for V_P=15V and various v_{ac}, showing spring hardening effect (a) forward sweep (b)(c)(d) forward and backward sweeps.

The bending-to-higher-frequency response curve indicates that at low DC polarization voltage V_P=20V, the nonlinear behavior of the cc beam resonator is of the hardening type. However, as discussed in Chapter 2.2.3, the cubic nonlinear spring constant also contains an electrostatic component k_{3e} and according to Eq. 2.17, the effect of k_{3e} becomes more pronounced for large V_P values. Fig. 3.18 presents the measured frequency responses at V_P=70V. As expected, the response curves bend to lower frequency side due to the negative k_{3e}.

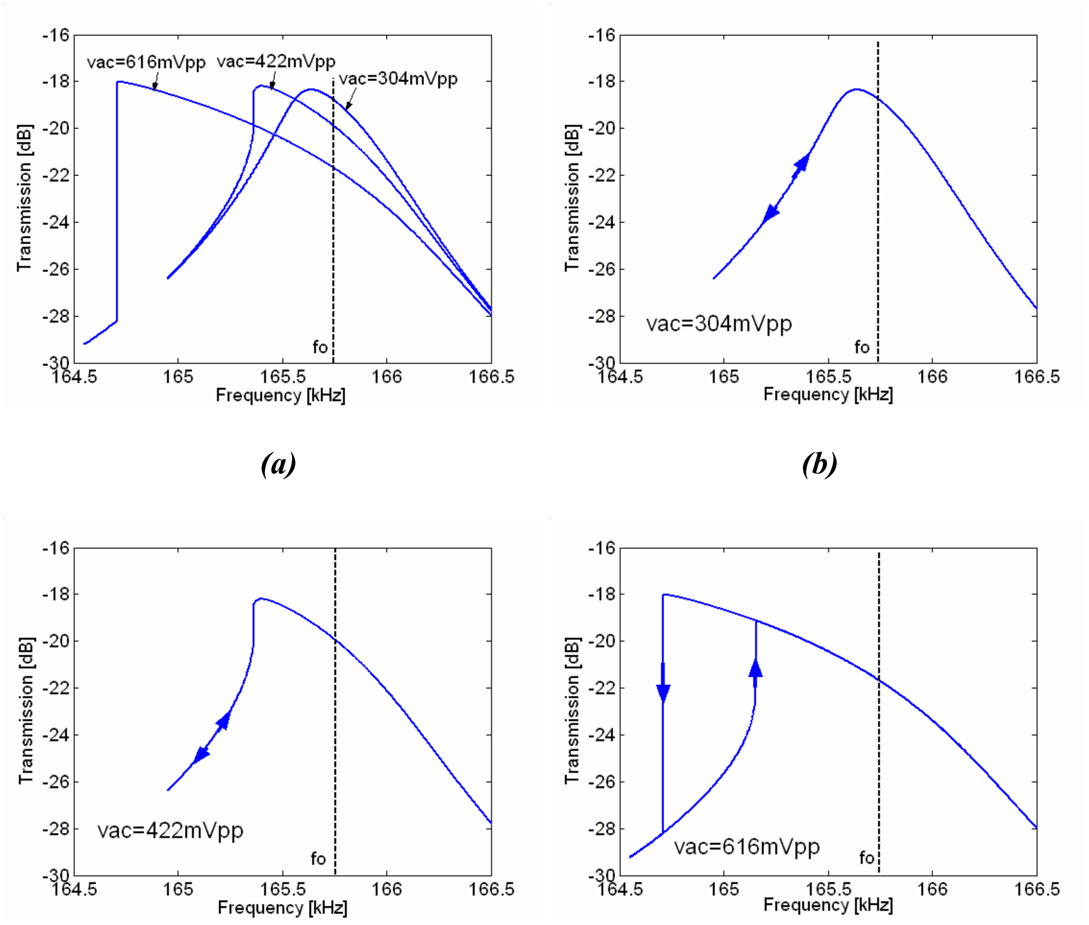

(a) *(b)*

(c) *(d)*

Figure 3.18 Measured S21 transmissions for V_P=70V and various v_{ac}, showing spring softening effect (a) backward sweep (b)(c)(d) forward and backward sweeps.

Besides the spring hardening and softening behaviors, Fig. 3.19 presents the frequency response measured at an intermediate polarization voltage of V_P=45V. As shown, the response curve evolves quite differently from Fig. 3.17 and Fig. 3.18. Specifically, as v_{ac} is increased, the resonance first tilts to higher frequencies and later to lower frequencies.

The "bending-to-different-directions" phenomenon is unexpected and it cannot be explained by the third order equation of motion (Eq. 2.19). The root cause is that at intermediate V_P, the cubic mechanical and electrostatic nonlinear spring constants almost cancel out (i.e. $k_3=k_{3m}+k_{3e}\approx 0$) and hence the effects of even higher order nonlinearities begin to show up. Apart from the frequency bending, the resonance peaks for the three curves are also different, manifesting that the nonlinearities not only adjust the resonant frequency, but also alter the structural damping and Q value.

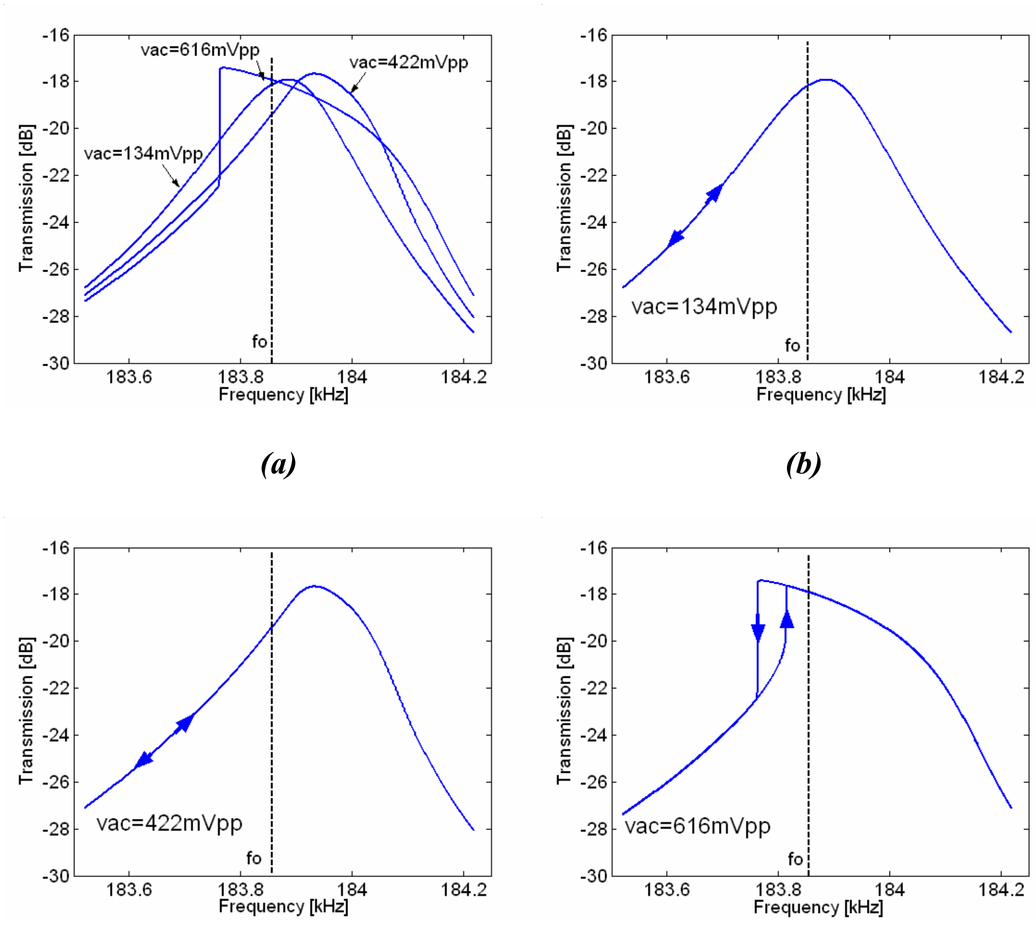

(a) *(b)*

(c) *(d)*

Figure 3.19 Measured S21 transmissions for V_P=45V and various v_{ac} , showing nonlinearity cancellation (a) backward sweep (b)(c)(d) forward and backward sweeps.

To summarize the nonlinearity induced frequency shift, Fig. 3.20 presents the effective amplitude-frequency coefficient α under different driving conditions.

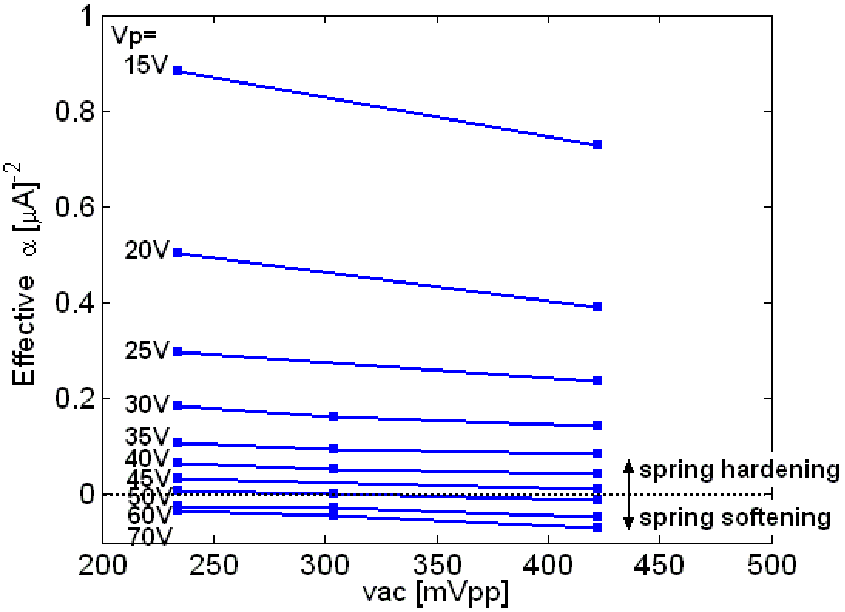

Figure 3.20 Effective amplitude-frequency coefficient α for different driving conditions.

As Fig. 3.20 shows, for a fixed V_P, α is almost a constant, regardless of the AC voltage applied. This indicates that the stabilization of the resonant frequency cannot be achieved by controlling the AC excitation voltage. As V_P changes, α is positive at low V_P and negative at high V_P. The positive α means that the resonant frequency increases with the vibration amplitude, showing the spring hardening effect, whereas the negative α means that the resonant frequency decreases as the vibration amplitude grows, presenting the spring softening behavior. At intermediate V_P values between 45V to 50V, α is very close to zero. This is where the nonlinearity cancellation occurs and operation in this regime gives the resonator a better signal strength with minimal frequency fluctuations. It is also observed in Fig. 3.20 that α is more sensitive to V_P change in the spring hardening domain than in the spring softening domain. In other words, as the electrostatic nonlinearities are increased, α becomes less dependent on the polarization voltage applied. This agrees well with Eq. (2.25) and it offers designers more flexibility to choose the appropriate polarization voltage while still keeping α small. Using the proposed semi-analytic characterization technique in Chapter 3.1.3, the model parameters of the cc beam resonator are extracted from the experimental data at V_P = 20, 30 and 40V as follows:

$k_{1m} = 144.8\,\text{N/m}$, $m = 9.589 \times 10^{-11}\,\text{kg}$, $k_{3m} = 6.816\,\mu\text{N}/\mu\text{m}^3$ and $\beta = 0.66$.

Substituting all these parameters into Eq. (2.25), Fig. 3.21 plots the experimental and simulated relationship between V_P and α. As shown, excellent agreement is achieved between the two curves.

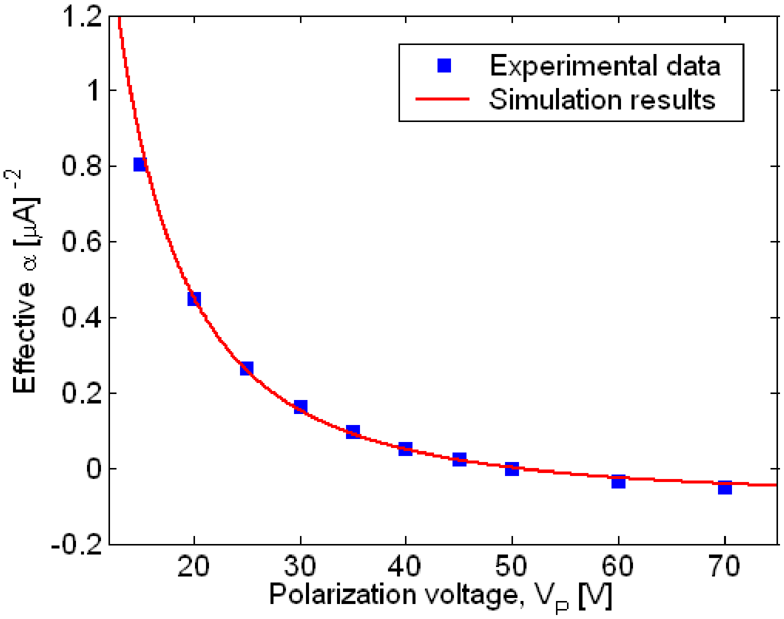

Figure 3.21 Relationship between V_P and α for the cc beam resonator.

In addition to the amplitude-frequency coefficient, Fig. 3.22 presents another comparison between the simulated critical vibration amplitudes Y_C (Eq. (2.10)) and those calculated based on the electrical measurement results (Eq. (2.20)). During this experiment, the input v_{ac} to the resonator was increased in a step of 0.5 dBm, until the hysteresis was observed, and accordingly the measurement uncertainty was within ±0.5 dB.

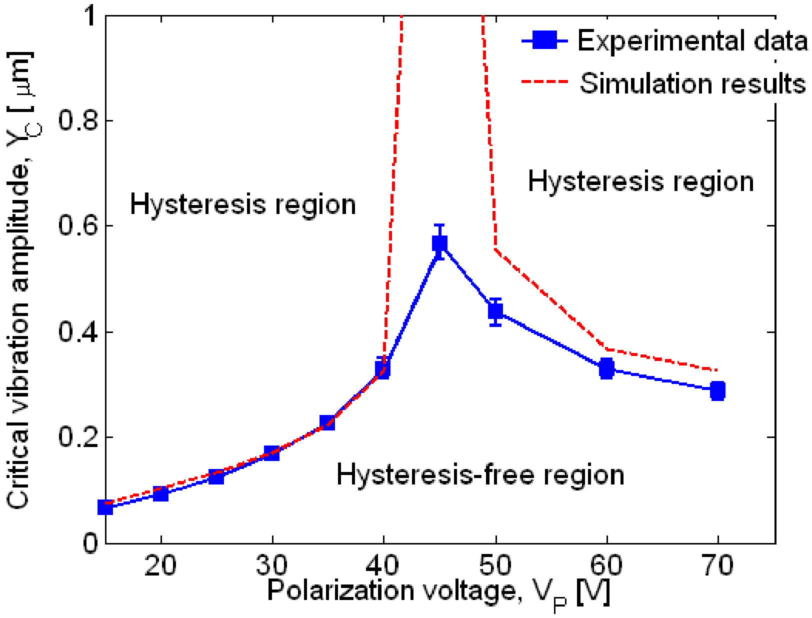

Figure 3.22 Critical vibration amplitude Y_C of the cc beam resonator.

As shown in Fig. 3.22, the boundary curve separates the V_P-Y_C plane into two different regions. Above the boundary curve, the multi-valued hysteresis response is observed, and below the curve is the linear hysteresis-free region. The nonlinearity cancellation occurs in the vicinity of 45V, which boosts the vibration amplitude to 0.57 μm. According to Eq. (2.29), the larger Y_C increases the maximum storable energy $E_{stored}^{\max}$ in the resonator. The exact value of $E_{stored}^{\max}$ is plotted in Fig. 3.23, where $E_{stored}^{\max}$ at V_P = 45V is around 2.059×10^{-11} J.

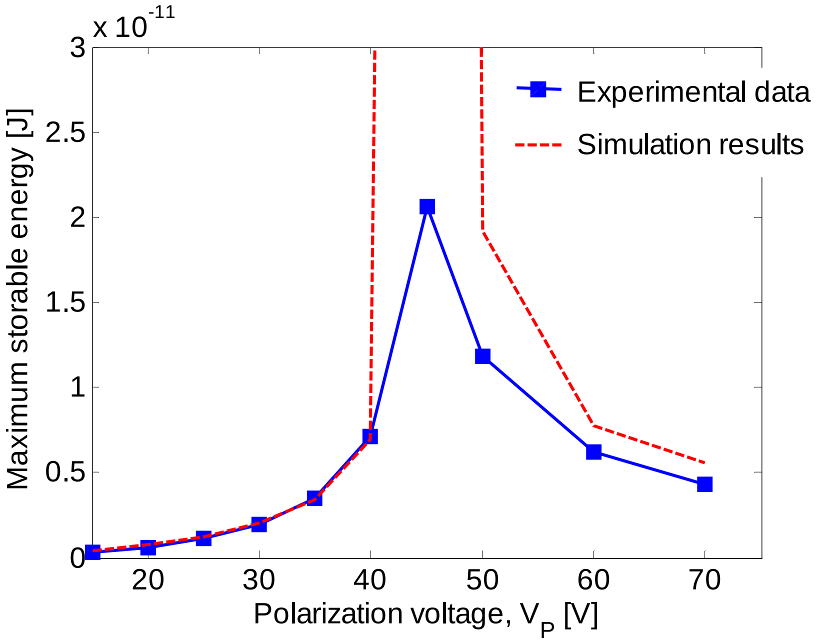

Figure 3.23 Maximum storable energy of the cc beam resonator.

In Figs. 3.22 and 3.23, the simulation results deviate from the measured values around V_P=45V. Since the nonlinear model only includes the nonlinear spring constants up to third order, this deviation again tells that the actual behavior of the resonator in the nonlinearity cancellation regime is determined by even higher order nonlinearities. Although the simulation accuracy can be improved by introducing more higher order terms into Eq. (2.7), the equation of motion will become too complicated to be solved in the closed form.

From the above discussion, it becomes clear that the presence of the mechanical hardening and electrostatic softening effects provides the possibility of the first order nonlinearity cancellation which improves the overall device performance. However, such cancellation is not always achievable. For experimental illustration, another cc beam resonator was implemented using the same SOIMUMPs process. The new beam length and width were 300 μm and 6 μm respectively with all the other dimensions remaining the same as those of the original cc beam resonator. The measured response curves for this resonator at V_P=70V are plotted in Fig. 3.24.

As shown, the resonance keeps bending to higher frequencies as v_{ac} is increased, showing the spring hardening effect. Although the nonlinearity cancellation can occur if V_P is further increased, the extra high polarization voltage and possibility of pull-in failure make the nonlinearity cancellation less practical. Therefore, to achieve reasonable V_P for cancellation to happen, k_{3m} should be minimized. According to Eq. 3.6, this requires the cc beam resonator to be long and narrow, similar to the original resonator.

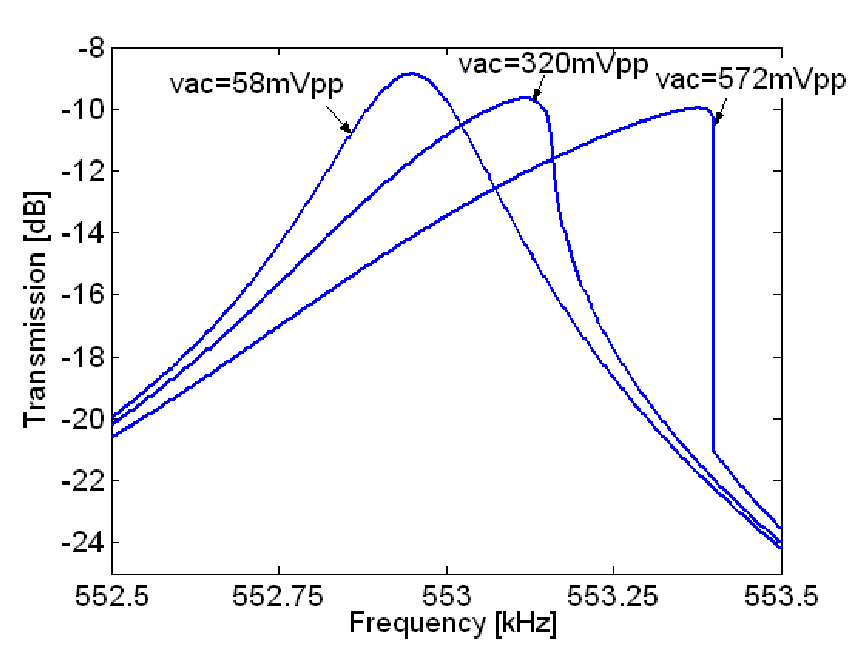

Figure 3.24 Measured S21 transmissions (forward sweep) for the 300μm long and 6μm wide cc beam resonator at V_P=70V, showing spring hardening effect.

3.2.2 Summary

Detailed analysis of the nonlinear behavior of a micromechanical cc beam resonator under different driving conditions is presented. The beam resonator was designed to be 5 μm wide, 446 μm long and 25 μm thick. It has a resonant frequency of 194 kHz with a Q value of 6308 in 37.5 μTorr pressure. For polarization voltages below 45V, the nonlinear frequency response of the resonator bends to the higher frequency side due to the mechanical spring hardening effect. When polarization voltages increase above 45V, the nonlinear response curve tilts to the lower frequency side because of the electrostatic spring softening effect. At intermediate voltage levels, the useful cancellation between the mechanical and electrostatic nonlinearities is observed which reduces the overall nonlinear stiffness of the device. Specifically, we found that the nonlinearity cancellation helps to stabilize the resonant frequency by reducing the amplitude-frequency coefficient to almost zero. In addition, the nonlinearity cancellation boosts the critical vibration amplitude to 0.57 μm and maximum storable energy to 2.059×10^{-11} J. However, for certain resonators with very large k_{3m} or very small k_{3e}, the nonlinearity cancellation might not happen. To achieve a reasonably low polarization voltage for the cancellation, guidelines such as designing the beam resonator to be long and narrow need to be followed.

Chapter 4 Nonlinearity in bulk mode resonators

Chapter 3 has demonstrated that the proposed semi-analytic technique is able to accurately characterize and model the nonlinearities in flexural mode resonators. In this chapter, we will extend the proposed technique to the study of nonlinearities in bulk mode resonators. Comprehensive comparison between the flexural mode and bulk mode resonators reveals that bulk mode resonators perform much better than their flexural mode counterparts for high frequency applications.

4.1 Scaling limit of flexural mode resonators

Very much like the case for transistors, extending the frequencies of micromechanical resonators into VHF and UHF ranges requires scaling down of the resonators' dimensions. As can be seen from Eqs. (3.1) and (3.7), the resonator scales as:

$$\hat{l} = \frac{l}{\sigma}$$

$$\hat{f}_0 = \sigma f_0 \qquad (\sigma > 1) \tag{4.1}$$

where l and $\hat{l}$ are the linear dimensions of the resonator; f_0 and $\hat{f}_0$ are the resonant frequencies and σ is the scaling factor.

Although it is possible to reduce the size of flexural mode resonators to achieve higher frequencies, "scaling-induced limitations" will show up such as the increased susceptibility to temperature and contamination fluctuations and insufficient power handling capabilities. While the first two issues can be alleviated by using the appropriate device packages, the last one is quite challenging. In order to elucidate the scaling-induced power handling limitations in flexural mode resonators, the cc beam resonator is used here as an example. The linear and cubic spring constants of a cc beam resonator are given by (Young W C, 2002):

$$k_1 \approx k_{1m} = 16.23E\frac{W_r^3 h}{L_r^3} \tag{4.2}$$

$$k_3 \approx k_{3m} = 12.18E\frac{W_r h}{L_r^3} \tag{4.3}$$

Note that the approximation of $k \approx k_m$ is only valid for high frequency cc beam resonators whose mechanical spring constants are much larger than the electrostatic ones. Substituting Eqs. (4.2) and (4.3) into Eq. (2.29), the maximum storable energy $E_{stored}^{\max}$ of the resonator can be expressed as:

$$E_{stored}^{\max} = 22.2E\frac{1}{Q}\frac{W_r^5 h}{L_r^3} \tag{4.4}$$

By optimistically assuming that the scaling does not affect the frequency-quality factor product (i.e. $\hat{Q} = Q/\sigma$), it can be deducted from Eq. (4.4) that $E_{stored}^{\max}$ scales as:

$$\hat{E}_{stored}^{\max} = \frac{E_{stored}^{\max}}{\sigma^4} \Rightarrow \frac{\hat{E}_{stored}^{\max}}{E_{stored}^{\max}} = \left(\frac{f_0}{\hat{f}_0}\right)^4 \tag{4.5}$$

From Eq. (4.5), a tradeoff between the resonant frequency and maximum storable energy is observed. It is this tradeoff that hinders the flexural mode resonators from being used in high frequency applications.

In order to address the limitations of flexural mode resonators, some previous work shows that bulk mode resonators are capable of storing several orders of magnitude larger vibration energy than flexural mode resonators (Kaajakari V, 2004a; Kaajakari V, 2004b). However, the research on the nonlinearities in bulk mode resonators is still in the infant stage and previous work only focused on the longitudinal and square extensional mode resonators. One of the main drawbacks of these two resonators is that both of them are single-ended devices and hence suffer from the feed-through interference, limited dynamic range of input and output signals, etc..

As an alternative, we will report the first study of nonlinearities in a fully differential Lamé-mode bulk resonator in this chapter. Characterization and modeling of the nonlinearities will be carried out using the proposed semi-analytic technique. Comparison between the bulk mode and flexural mode resonators will also be covered.

4.2 Resonator design and fabrication

The bulk mode resonator is designed to operate in the Lamé mode (Majjad H, 2001; Bhave S A, 2005) and fabricated using the SOIMUMPs process. The modal simulation done with the finite element software, ABAQUS, and a micrograph of the resonator are shown in Fig. 4.1.

In this mode, the edges of the square plate bend in anti-phase while the plate volume is preserved. This particular vibration mode facilitates the differential driving and sensing of the resonator. The length of the square edge is 650 μm. For support beams are placed at the corners of the plate (nodal points). Such configuration helps to minimize the energy losses from the resonator through the support beams to the substrate.

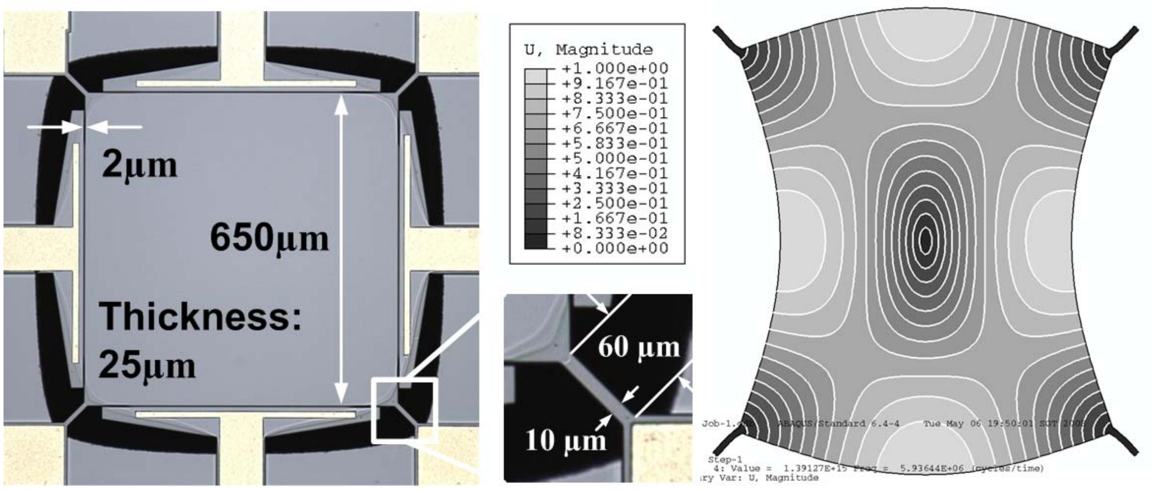

Figure 4.1 Micrograph of the Lamé-mode resonator and its modal simulation in ABAQUS.

If the material of the square plate is isotropic and the edge length *L* of the square is much larger than its thickness (25 µm), the resonant frequency f_0 can be calculated using the formula (Bhave S A, 2005):

$$f_0 = \sqrt{\frac{G}{\rho}} \frac{1}{\sqrt{2}L} \tag{4.6}$$

where *G* is the shear modulus and is given by:

$$G = \frac{E}{2(1+\nu)} \tag{4.7}$$

According to Eq. (4.6), the resonant frequency is 5.81 MHz, which is very close to the ABAQUS simulated value of 5.93 MHz.

4.3 Measurement setup and resonator characterization

Fig. 4.2 presents the fully differential driving and sensing measurement setup for the Lamé-mode resonator. The output currents from the resonator were converted to voltages through an off-chip differential trans-impedance amplifier with C_f = 2 pF and R_f = 685 kΩ. The air pressure of the measurement was kept around 37.5 µTorr throughout the measurement.

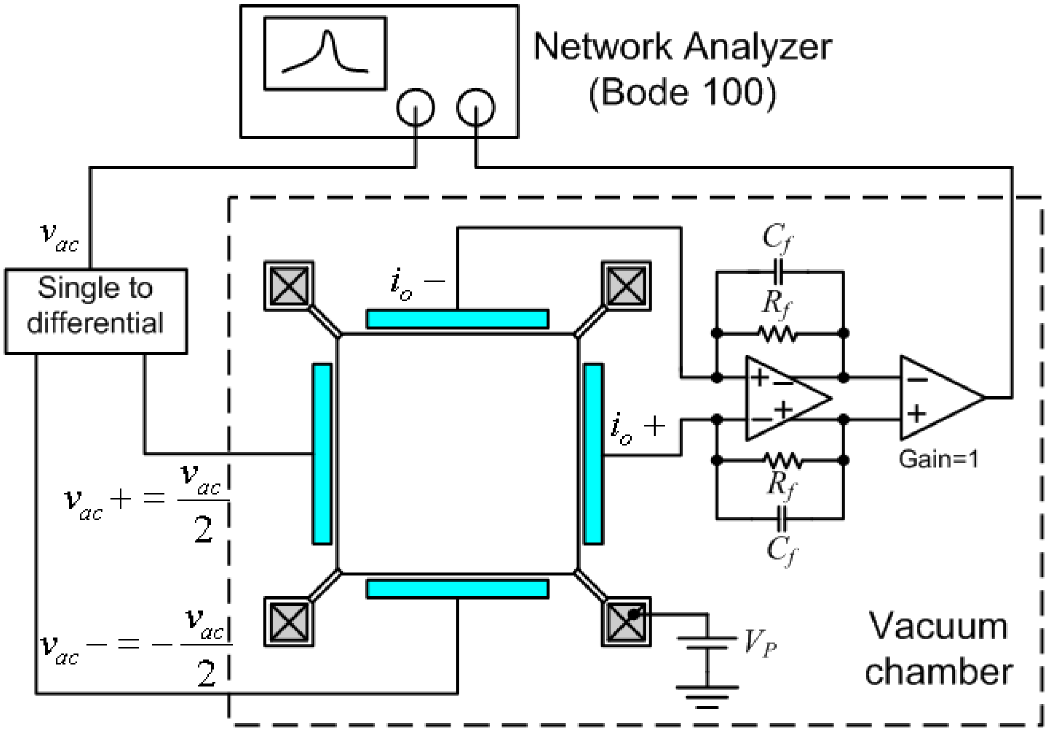

Figure 4.2 Differential drive and sense measurement setup for the Lamé-mode resonator.

The measured S21 transmission curve for the Lamé-mode resonator is plotted in Fig. 4.3. As shown, the resonant frequency is around 6.353 MHz with Q as high as 1.7 million. The anti-resonance peak due to the feed-through capacitance is effectively suppressed by the differential measurement setup. The corresponding phase plot also shows the expected sudden drop at resonance.

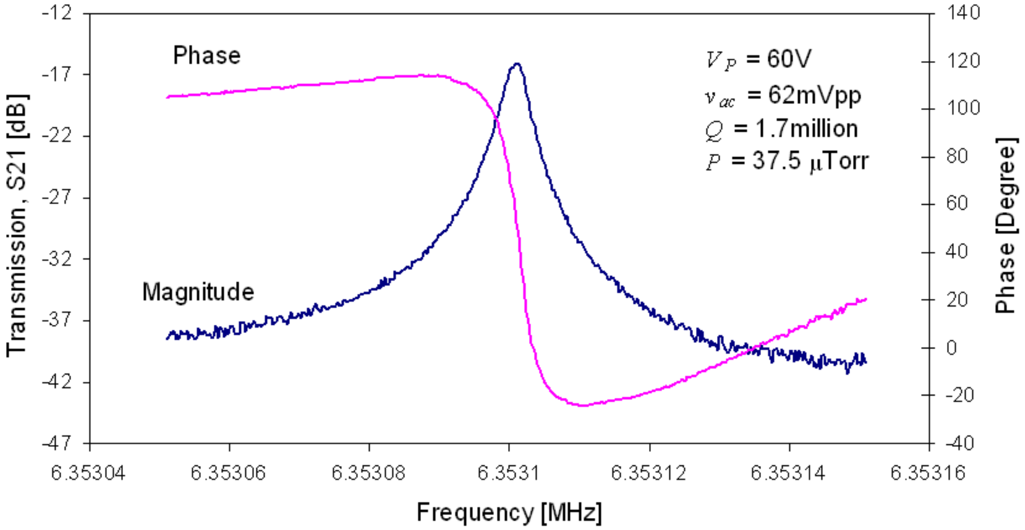

Figure 4.3 Measured S21 transmission curve for the 6.35 MHz Lamé-mode resonator.

The almost symmetric shape of the transmission curve in Fig. 4.3 was only observed for low AC excitation voltages. When v_{ac} was increased while V_P was fixed at 60V, the resonator was progressively driven into the nonlinear regime, showing an amplitude dependent resonant frequency f_0'.

As Fig. 4.4 shows, for v_{ac} = 1.322V$_{PP}$, the transmission curve still remains single-valued. As v_{ac} is further increased, the curves keep bending to lower frequencies, eventually showing the discontinuity due to hysteresis at v_{ac} = 2.662V$_{PP}$ and 3.916V$_{PP}$. The bending-to-lower-frequency phenomenon indicates that the nonlinearities in the Lamé-mode resonator are of the softening type.

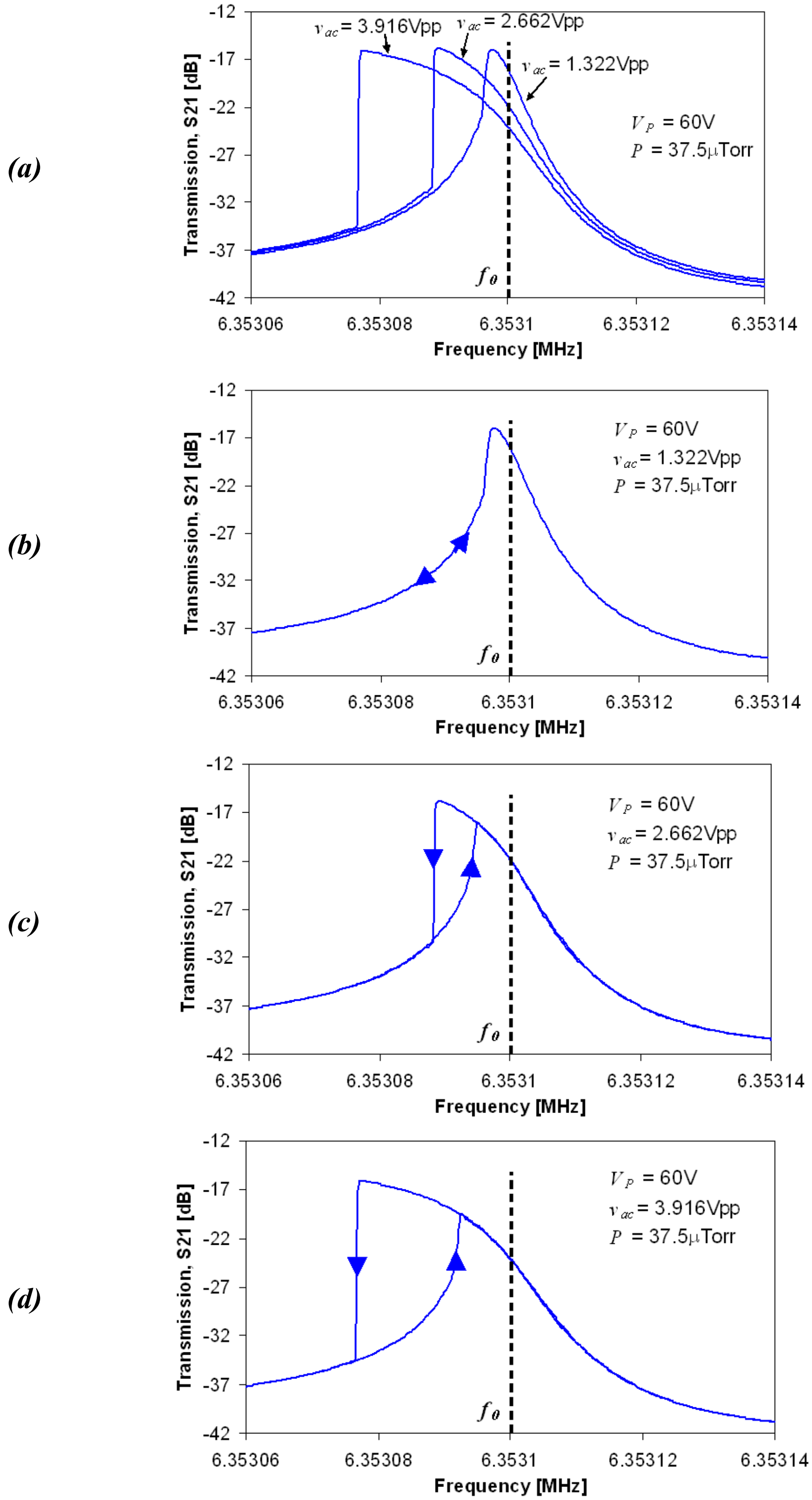

Figure 4.4 Measured S21 transmissions for V_P=60V and various v_{ac}, showing spring softening effect (a) forward sweep (b)(c)(d) forward and backward sweeps.

Applying the semi-analytic technique, all the key model parameters of the Lamé-mode resonator were extracted and summarized in Table 4.1. For comparison purpose, the parameters of the second-mode free-free beam resonator (with three support beams) mentioned earlier in Chapter 3.1 are also tabulated. The second-mode ff beam resonator is chosen here because it is also fully differential and exhibits the spring softening behavior, similar to the Lamé-mode resonator.

Table 4.1 Model parameters of the Lamé-mode and second-mode free-free beam resonators.

Parameter	**Resonator**	
	Lamé-mode	**Second-mode ff beam**
Layout area	650 μm × 650 μm	650 μm × 470 μm
Resonant frequency, f_0	6.353 MHz	550 kHz
Quality factor, Q	1.7 million	10 k
Lumped mass, m	1.352×10^{-8} kg	5.5374×10^{-10} kg
Linear mechanical spring constant, k_{1m}	$\approx k_1 = 2.155\times10^{7}$ N/m	6701.88 N/m
Cubic mechanical spring constant, k_{3m}	$\approx k_3 = -2.4\times10^{15}$ N/m^3	-4.785×10^{12} N/m^3
Nonlinear parameter, κ	-2.657×10^{14} Hz/m^2	-1.5×10^{15} Hz/m^2 (V_P=60V)

4.4 Comparison between the bulk mode and flexural mode resonators

In this section, the performance of the bulk mode and flexural mode resonators will be compared in terms of resonant frequencies, quality factors and nonlinear behaviors.

4.4.1 Resonant frequency and quality factor

As Table 4.1 shows, with comparable layout area, the Lamé-mode resonator is able to achieve a resonant frequency up to 6.353 MHz, which is much higher than 550 kHz for the second-mode ff beam resonator. This is due to the much stiffer structure (larger k_1) of the Lamé-mode resonator, according to Eq. (2.3):

$$f_0 = \frac{1}{2\pi}\sqrt{\frac{k_1}{m}}$$

Besides the resonant frequency, it is also noted that the quality factor Q of the Lamé-mode resonator is 1.7 million, substantially higher than that of the second-mode ff beam resonator. While the ultra high Q of the Lamé-mode resonator can be partially attributed to the nodal support design, the main reason is still its high stiffness. According to Eq. (2.4), the Q definition is:

$$Q = \frac{\sqrt{k_1 m}}{\gamma}$$

where the damping coefficient γ is roughly of the same range for both resonators in vacuum.

4.4.2 Resonator nonlinearities

While the comparisons presented in section 4.4.1 are all based on linear vibration, this section will focus on the nonlinear behaviors of the two resonators. As can be seen from Figs. 3.13 and 4.4, both the Lamé-mode and second-mode ff beam resonators exhibit softening type nonlinearities. However, the amounts of nonlinearities in these two resonators are quite different. To show the difference, Fig. 4.5 plots the nonlinear response curves of the two resonators under the same driving condition.

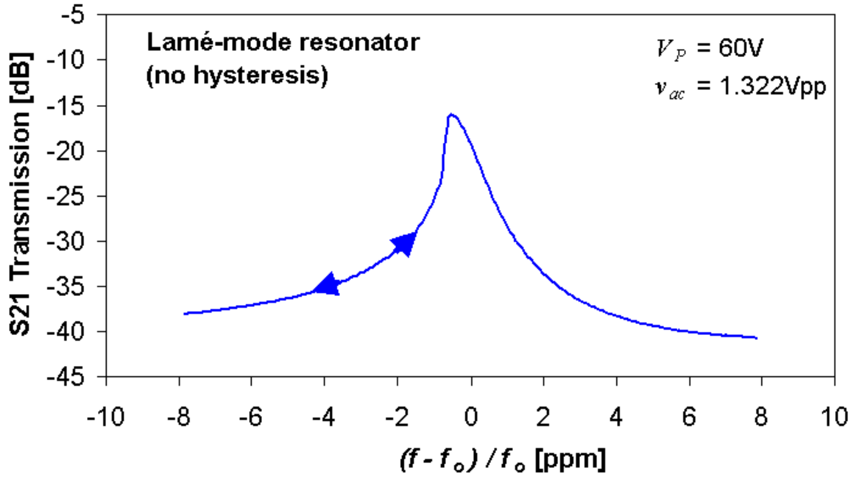

(a)

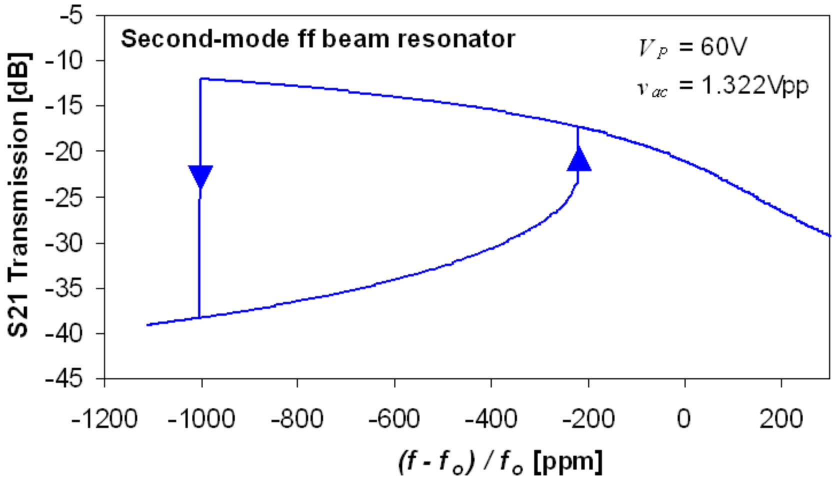

(b)

Figure 4.5 Measured transmission curves at V_P = 60V and v_{ac} = 1.322V_{PP} for the (a) Lamé-mode and (b) second-mode ff beam resonators. Note that the x range in (b) is much wider than the x range in (a).

As shown, at V_P = 60V and v_{ac} = 1.322V_{PP} , the response curve of the Lamé-mode resonator is still a single-valued function. However, for the second-mode ff beam resonator, the resonant frequency is shifted by more than 1000 ppm and a large frequency hysteresis loop is observed, both indicating a more severe nonlinear vibration. Qualitatively, the minimal nonlinear effects in the Lamé-mode resonator result from its high stiffness and hence small vibration amplitude. Quantitatively, the amount of frequency shift is determined by both nonlinear parameter κ and vibration amplitude at resonance $Y_{0,f_0'}$, as shown by Eq. (2.8):

$$\Delta f_0 = f_0' - f_0 = \kappa Y_{0,f_0'}^2$$

In Table 4.1, κ of the Lamé-mode resonator is smaller than that of the second-mode ff beam resonator by 82%. Furthermore, according to Eq. (2.22), $Y_{0,f_0'}$ of the Lamé-mode resonator is about 84% smaller than that of the second-mode ff beam resonator under the same driving condition. Hence, both small κ and $Y_{0,f_0'}$ make the Lamé-mode resonator less susceptible to the nonlinear effects.

In order to further compare the nonlinear performance between the flexural mode and bulk mode resonators, Fig. 4.6 presents the absolute effective amplitude-frequency coefficients $|\alpha|$ and maximum storable energies $E_{stored}^{\max}$ for the fundamental-mode and second-mode ff beam resonators, cc beam resonator and Lamé-mode resonator. (The former three flexural mode resonators have already been discussed in Chapter 3.) As Fig. 4.6(a) shows, $|\alpha|$ of the Lamé-mode resonator is more than four orders of magnitude smaller than those of the flexural mode resonators. This enables the Lamé-mode resonator to achieve very stable vibration. In addition, Fig. 4.6(b) shows that $E_{stored}^{\max}$ of the Lamé-mode resonator is about three orders of magnitude larger than those of the

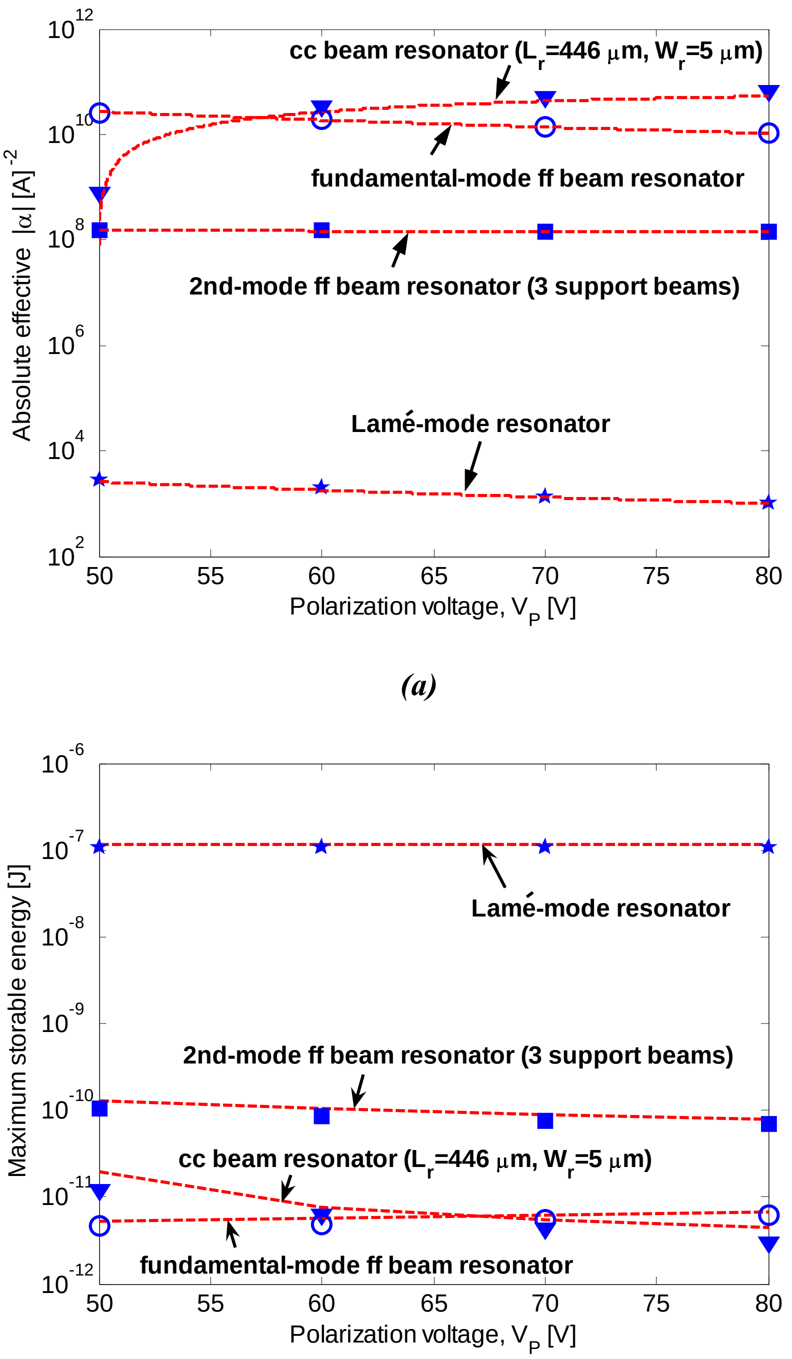

(a)

Reported $E_{stored}^{\max}$ by other research groups (Kaajakari V, 2004b) for the cc beam resonator: 2.6×10^{-11} J, cantilever resonator (flexural mode): 1.5×10^{-10} J and square extensional mode resonator (bulk mode): 1.9×10^{-7} J.

(b)

Figure 4.6 (a) Absolute amplitude-frequency coefficients and (b) maximum storable energies of the flexural mode and bulk mode resonators (the markers represent the experimental data and the dashed lines are the simulation results).

flexural mode resonators. The large $E_{stored}^{\max}$ of the Lamé-mode resonator is attributed to its capability of attaining very high frequencies, while still retaining relatively large dimensions. According to the *Leeson's* equation (Eq. (2.27)), large $E_{stored}^{\max}$ is beneficial for both the noise floor and near carrier noise of the resonator-based oscillator.

4.5 Summary

We have presented comprehensive study of the nonlinearities in a 6.35 MHz Lamé-mode bulk resonator. The nonlinearities are of the softening type and progressively bend the resonance to the lower frequency side as the vibration amplitude grows. Compared with the flexural mode resonator, the Lamé-mode bulk resonator has much higher resonant frequency and quality factor due to its high stiffness. Besides, we have conclusively shown that the Lamé-mode bulk resonator has much smaller amplitude-frequency coefficient and much larger power handling capability, both making it a good solution to the scaling induced limitations. Hence, recent research interests are being shifted from flexural mode to bulk mode resonators, especially for VHF and UHF applications (Nguyen C T C, 2001). Motivated by this, two further studies will be conducted on bulk mode resonators in the next chapter.

Chapter 5 Further studies on bulk mode resonators

This chapter will present two further studies on bulk mode resonators. Firstly, the effect of etch holes on the quality factor is investigated. Totally five Lamé-mode resonators are designed and tested to explore how the quality factor is affected by the quantity and location of the etch holes. Secondly, a novel technique is proposed to reduce the capacitive gap size of the resonator below the fabrication limitation. Using this technique, a Lamé-mode resonator with 0.64 μm gap size is successfully implemented in the standard 2 μm SOIMUMPs process. Results of this chapter will be very useful for optimal design of the bulk mode resonators.

5.1 Effect of etch holes on the quality factor of bulk mode resonators

Surface micromachining (Carter J, 2005) and SOI based bulk micromachining (Miller K, 2004) are two of the most commonly used processes to fabricate the bulk mode micromechanical resonators. In surface micromachining process, a critical etch step is required to release the resonators from the substrate. To facilitate this release etch, so-called etch holes are typically formed in the bulk structures. These etch holes not only improve the etch uniformity, but also shorten the etch time and thus minimize the undesirable over-etch of other useful layers. However, in SOI based bulk micromachining process where the backside release etch is provided, bulk mode resonators can be fabricated with or without etch holes. Hence, it is very important to understand whether the etch holes will affect the resonator performance.

In the literature, some work has been done to examine the effect of etch holes on the mechanical properties (tensile stress and Young's modulus), electrostatic force behaviors and resonant frequencies of micromechanical structures (Rabinovich V L, 1997; Sharpe Jr W N, 1997; Hsu W T, 2007). However, none of them investigates how the quality factor of the resonator is affected.

5.1.1 Resonator design

With this motivation in mind, in this section, we study the effect of etch holes on the quality factor by examining five Lamé-mode resonators fabricated using the SOIMUMPs process. The micrograph of the first resonator without etch holes (resonator **A**), together with the modal simulation from ABAQUS, are presented earlier in Fig. 4.1. Based on resonator **A**, another four modified resonators with etch holes were also implemented. Their micrographs are presented in Fig. 5.1. As shown, the etch holes are intentionally placed: all over (resonator **B**), at the center (resonator **C**) of, at the middle edge (resonator **D**) of and at the corner (resonator **E**) of the resonator to investigate how the quality factors are affected by the quantity and location of the etch holes.

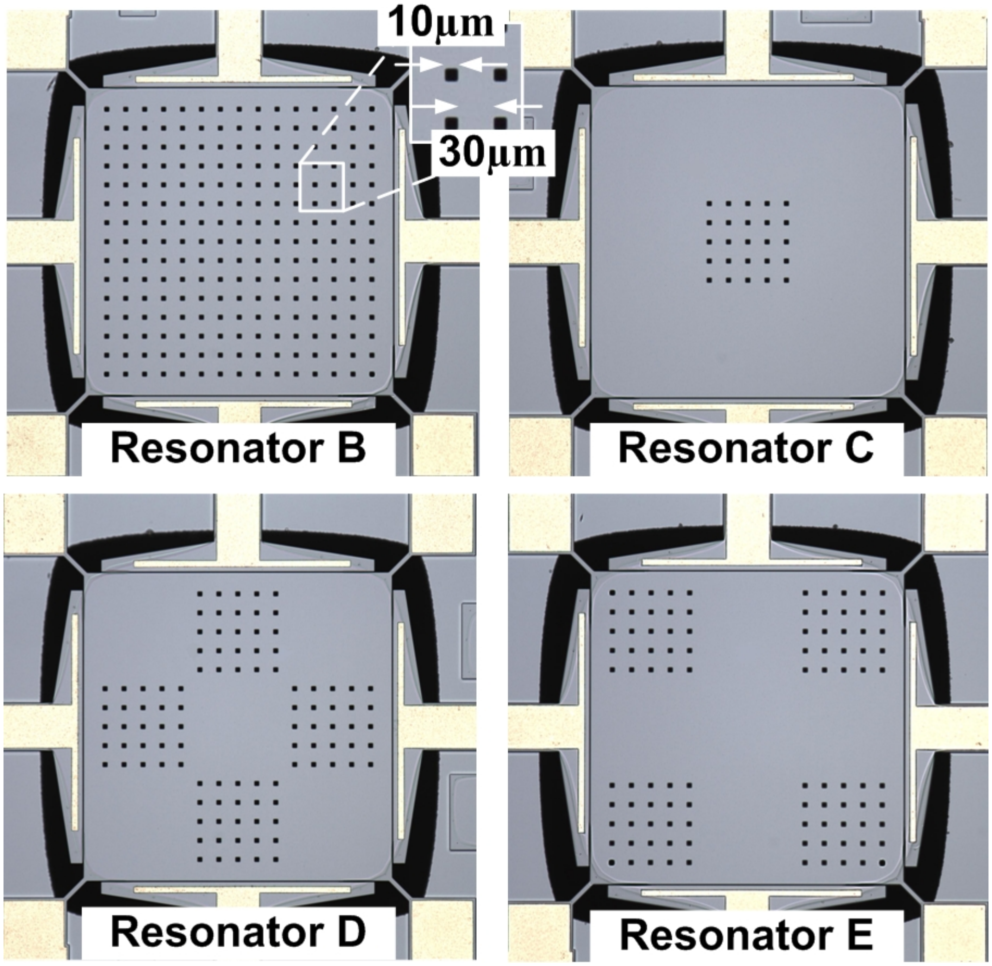

Figure 5.1 Micrographs of the four Lamé-mode resonators with etch holes and their dimensions.

5.1.2 Results and discussion

Fig. 5.2 plots the S21 transmission curves for resonator **A** and **B** using the fully differential driving and sensing measurement setup with C_f = 2 pF and R_f = 685 kΩ in vacuum pressure of 37.5 μTorr (Fig. 4.2). It can be seen that resonator **B**'s transmission curve is much broader (lower Q) than resonator **A**'s, showing the effect of etch holes.

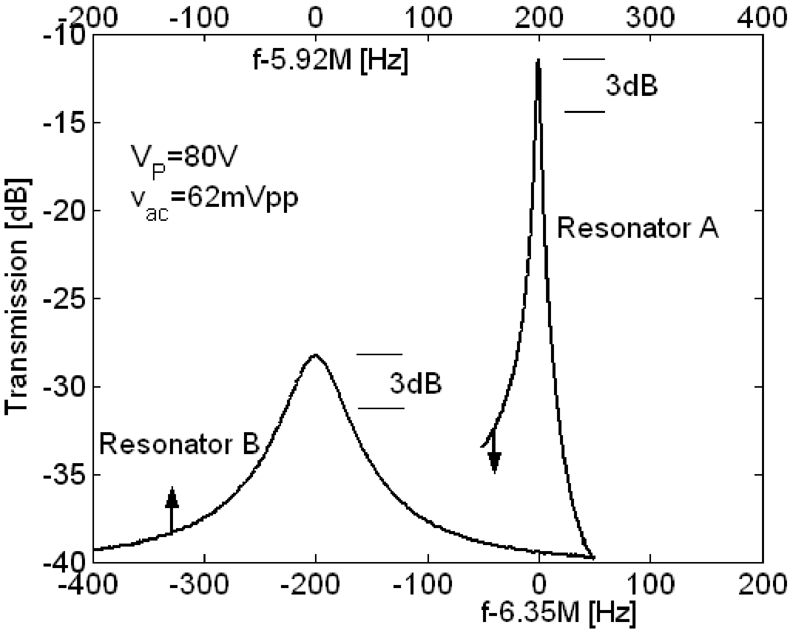

Figure 5.2 S21 transmission curves for resonator A and B with the same measurement setup.

To summarize the performance of all the five resonators, their measured and ABAQUS-simulated resonant frequencies and *Q*'s are listed in Table 5.1. The measurement was taken in vacuum with V_P = 80V and v_{ac} = 62mV$_{PP}$. The *Q*'s were experimentally measured based on the bandwidth at 3dB below the resonance peak. The repeatability of the measurements was ensured by testing each of the resonators on two different die samples. The results show that for a particular resonator **A** to **E**, *Q* varies between 3% and 7% across the two dies.

It is noted in Table 5.1 that the simulated f_0's match reasonably well with the measured ones. As for *Q*, resonator **A** exhibits the highest value of 1.7 million. For resonator **B** to **E** with etch holes, their *Q*'s decrease significantly with resonator **B** having the lowest *Q* of

116k. In order to further investigate the impacts of etch holes on quality factors, ABAQUS modal simulations were carried out for resonator **B** to **E**.

Table 5.1 Resonant frequency f_0 and quality factor Q for each of the Lamé-mode resonator (the measurement setup was the same for all the resonators).

Resonator	**Etch hole location**	**f_0 measured (MHz)**	**f_0 simulated (MHz)**	***Q* measured**	**Resonance peak (dB)**
A	none	6.35	5.936	1,666,383	-11
B	all over	5.92	5.65	115,575	-28.3
C	center	6.13	5.79	162,733	-26.79
D	middle edge	6.11	5.8	164,217	-35
E	corner	6.3	5.91	291,897	-28.05

As Fig. 5.3 shows, the mode shapes of resonator **B** to **E** are changed by the etch holes. Specifically, for resonator **B** with etch holes all over the surface, the displacement contours are distorted in the vicinity of etch holes. This distortion indicates that the longitudinal standing wave is interfered by the etch holes as it propagates through the resonator, leading to increased vibration energy dissipation $E_{dissipated}$. Consequently, the resonator's Q is decreased, according to Eq. 2.6:

$$Q = 2\pi \frac{E_{stored}}{E_{dissipated}}$$

Since the interference occurs everywhere across resonator **B**, the energy loss is also the highest among the five devices, and hence resonator **B** shows the lowest Q. Having less etch holes, resonator **C** is expected to have a higher Q than resonator **B**. However, due to the uneven mass distribution, the nodal points of resonator **C** are shifted to the inner part

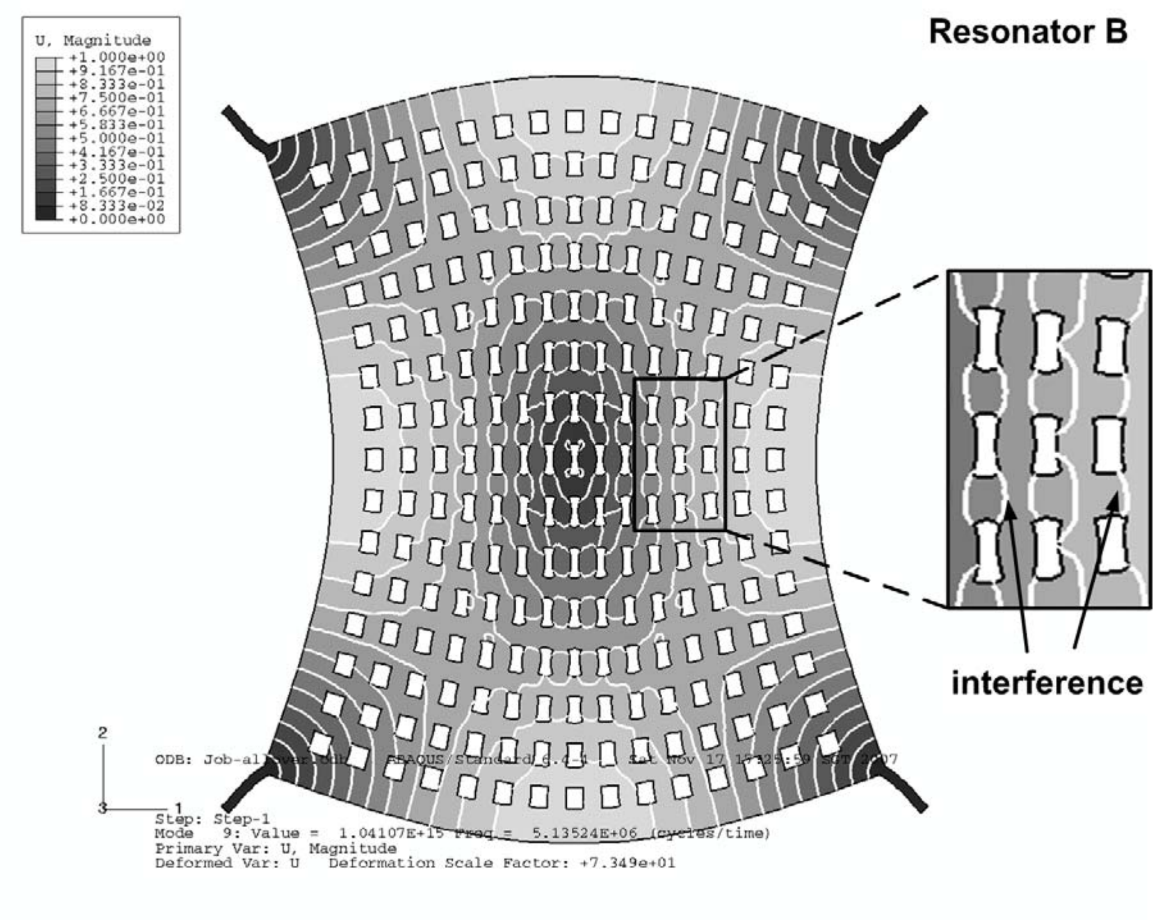
Resonator B
U, Magnitude
+1.000e+00
+9.167e-01
+8.333e-01
+7.500e-01
+6.667e-01
+5.833e-01
+5.000e-01
+4.167e-01
+3.333e-01
+2.500e-01
+1.667e-01
+8.333e-02
+0.000e+00
interference
2
3
1
ODB: Job-allover.odb ABAQUS/Standard 6.4-1 Sat Nov 17 15:25:59 SGT 2007
Step: Step-1
Mode 9: Value = 1.04107E+15 Freq = 5.13524E+06 (cycles/time)
Primary Var: U, Magnitude
Deformed Var: U Deformation Scale Factor: +7.349e+01

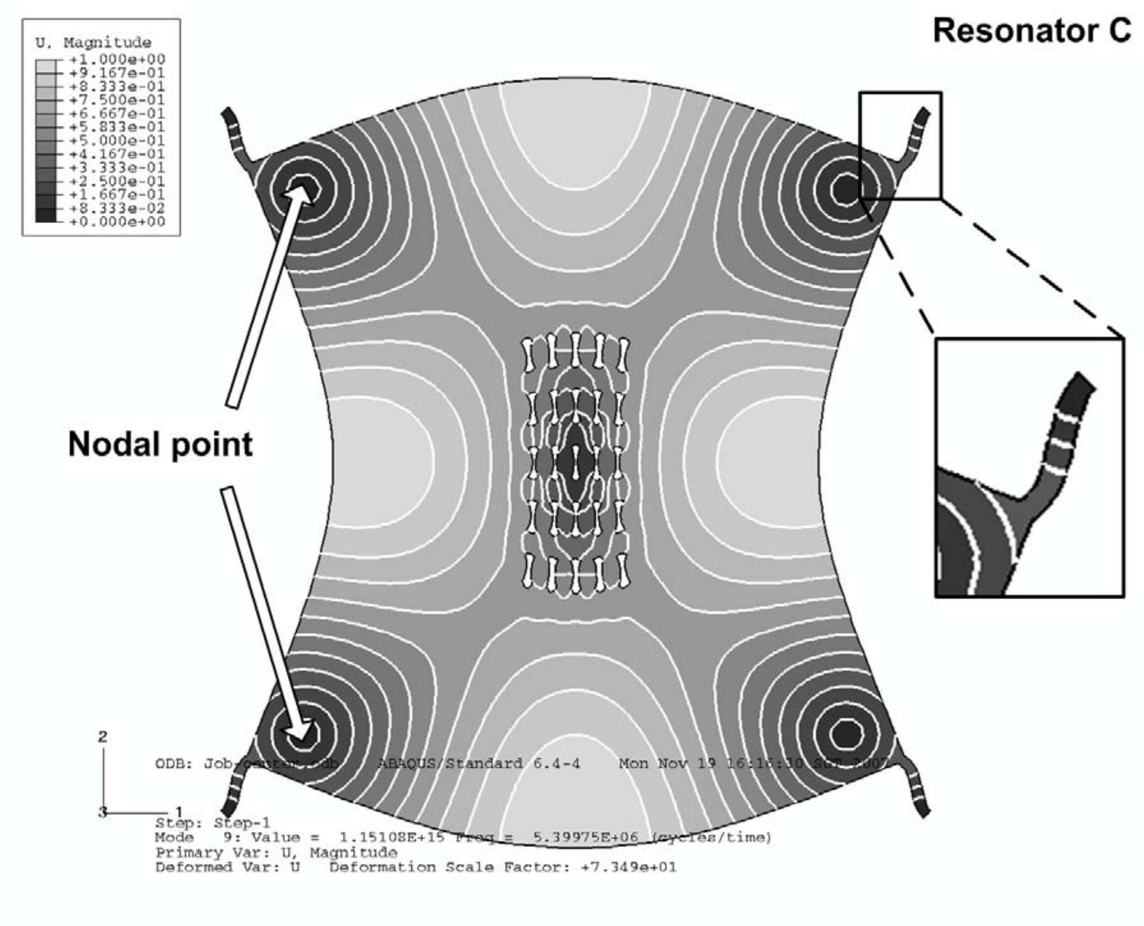
Resonator C
U, Magnitude
+1.000e+00
+9.167e-01
+8.333e-01
+7.500e-01
+6.667e-01
+5.833e-01
+5.000e-01
+4.167e-01
+3.333e-01
+2.500e-01
+1.667e-01
+8.333e-02
+0.000e+00
Nodal point
2
3
1
ODB: Job-center.odb ABAQUS/Standard 6.4-4 Mon Nov 19 16:16:30 SGT 2007
Step: Step-1
Mode 9: Value = 1.15108E+15 Freq = 5.39975E+06 (cycles/time)
Primary Var: U, Magnitude
Deformed Var: U Deformation Scale Factor: +7.349e+01

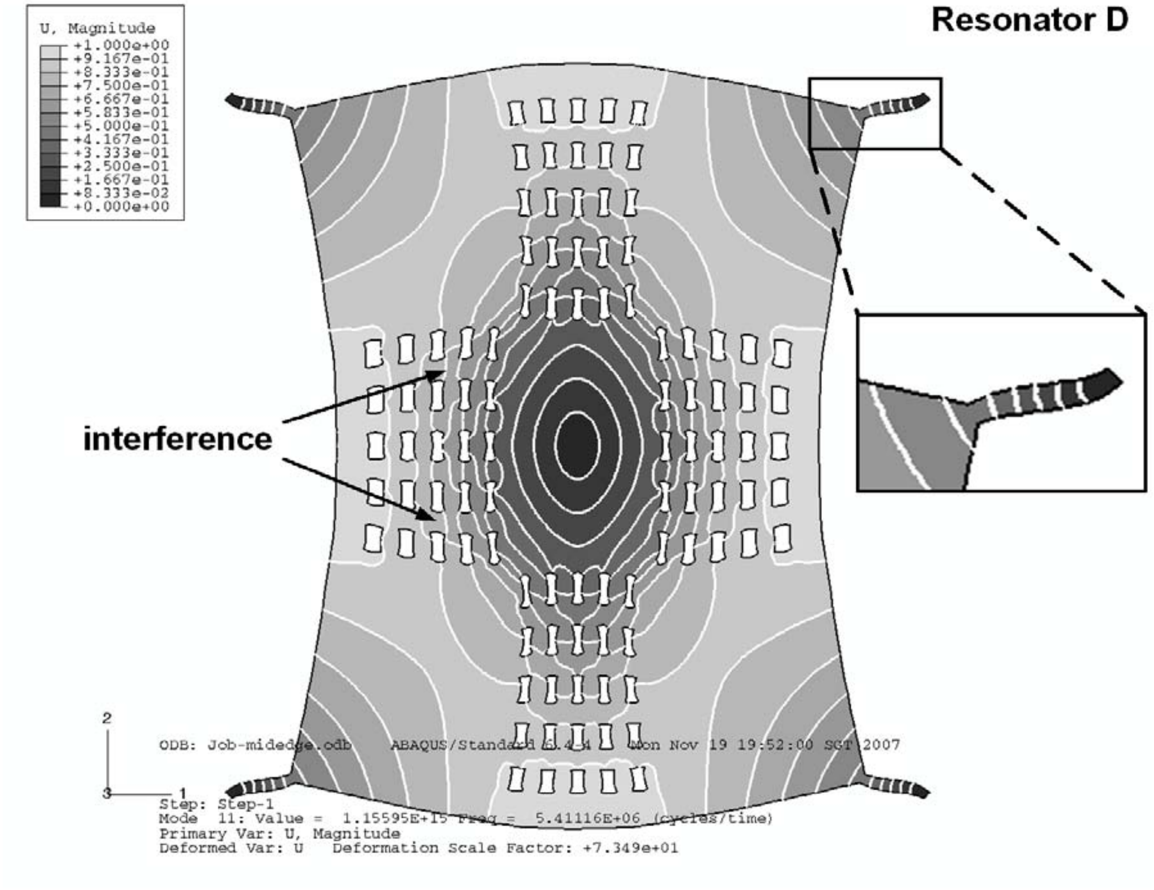
U, Magnitude
+1.000e+00
+9.167e-01
+8.333e-01
+7.500e-01
+6.667e-01
+5.833e-01
+5.000e-01
+4.167e-01
+3.333e-01
+2.500e-01
+1.667e-01
+8.333e-02
+0.000e+00
Resonator D
interference
2
3
1
ODB: Job-midedge.odb   ABAQUS/Standard 6.4-4   Mon Nov 19 19:52:00 SGT 2007
Step: Step-1
Mode 11: Value = 1.15595E+15 Freq = 5.41116E+06 (cycles/time)
Primary Var: U, Magnitude
Deformed Var: U   Deformation Scale Factor: +7.349e+01

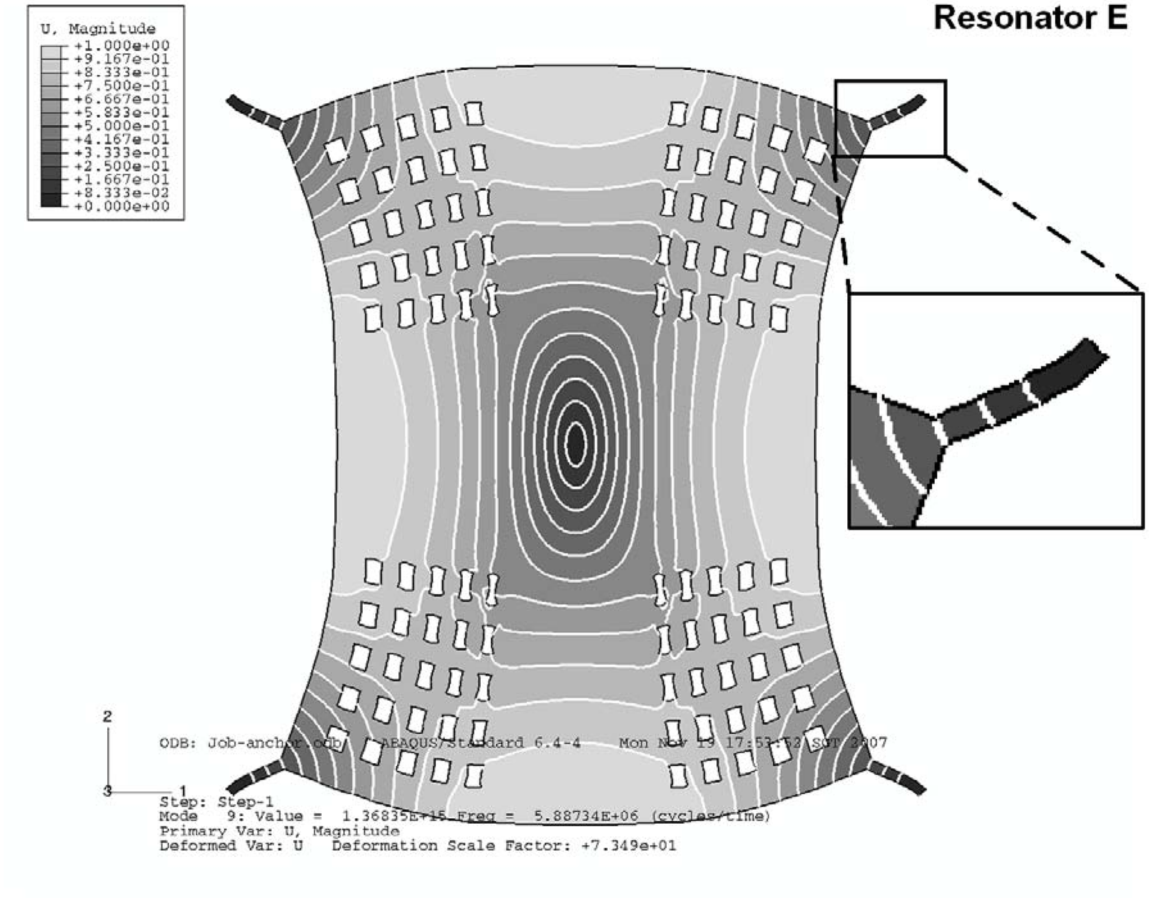

Figure 5.3 ABAQUS modal simulation for the four Lamé-mode resonators with etch holes.

of the plate and hence, the ends of the support beams start to move (Fig. 5.3). The movement of the support beams increases energy losses from the resonator through the support beams to the substrate. This partially cancels the benefits of using less etch holes. Resonator **D** and **E** have the same amount of etch holes, but their locations are different. For resonator **D**, the etch holes are distributed near the middle edge of the plate where the maximum displacement occurs. Due to the strong interference of the etch holes, the displacement contours are severely distorted, increasing the total energy losses. In contrast, for resonator **E**, the interference is minimal since the etch holes only cover the low-displacement corner regions. Furthermore, the modal simulation indicates that the movement of the support beams is reduced. Hence, resonator **E** exhibits the highest *Q* among resonator **B** to **E** due to the effective suppression of the energy losses.

It is also noted in Table 5.1 that although resonator **C** and **D** have almost the same *Q*'s, resonator **C**'s resonance peak is 8 dB above resonator **D**'s. According to Eq. (2.21), this observation tells that the etch holes not only affects the *Q* factor, but also alters the spring constant of the resonator. To verify this, Fig. 5.4 presents the frequency tuning characteristics for resonator **C** and **D**.

As shown, a tuning slope of -0.2336 ppm/V is achieved for resonator **C** whereas the tuning slope of resonator **D** is just -0.0927 ppm/V. The expression of the tuning slope can be derived by differentiating Eq. (2.18) with respect to V_P:

$$\text{Tuning slope} = \frac{1}{f_0}\frac{\partial f_0}{\partial V_P} \doteq -\frac{1}{k_{1m}}\left(\frac{4\varepsilon_0 W_e h V_P}{d^3}\right) \tag{5.1}$$

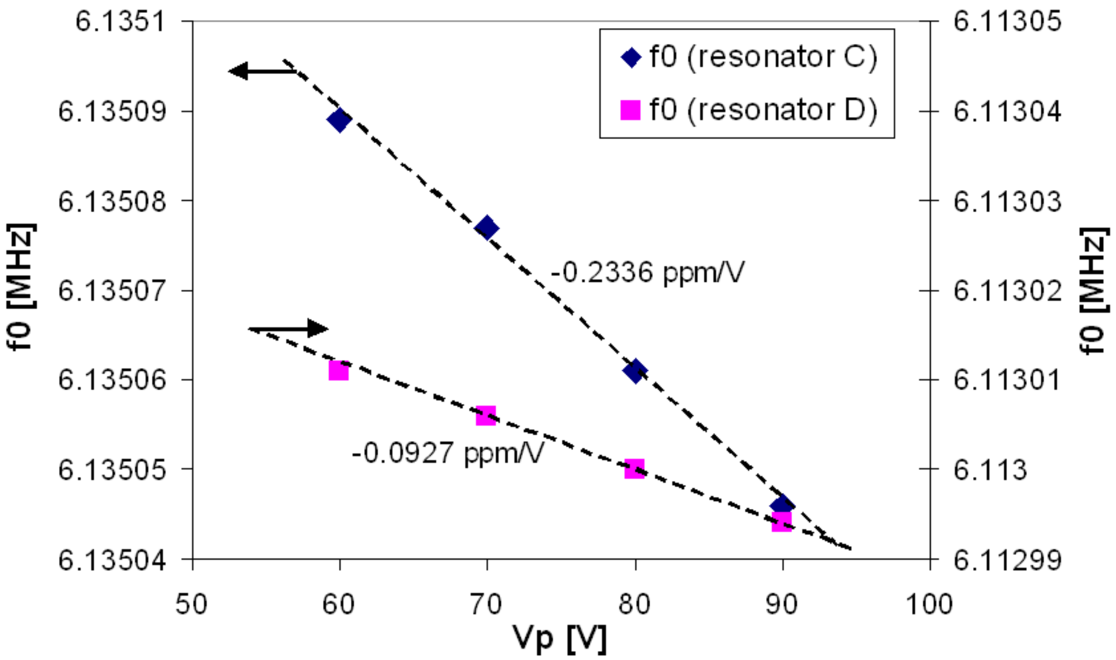

Figure 5.4 Measured frequency tuning characteristics for resonators C and D.

Based on Fig. 5.4 and Eq. (5.1), it can be seen that k_{1m} of resonator **C** is 2.5 times smaller than that of resonator **D**. According to Eq. (2.21), the 2.5 times smaller k_{1m} of resonator **C** leads to 8dB higher resonance peak than that of resonator **D**, which agrees well with the experimental observation in Table 5.1 and confirms that the etch holes change k_{1m} of the resonator.

5.1.3 Summary

Totally five Lamé-mode resonators have been designed, fabricated and tested to investigate the limit of the quality factors due to etch holes. It is found that the resonators with etch holes have quality factors reduced by an order of magnitude than the one without etch holes. ABAQUS simulation reveals that the reduction in Q is attributed to two energy loss mechanisms. The first mechanism is due to the interference between the longitudinal standing wave propagation and the etch holes while the second mechanism is caused by the movement of the support beams. It is also demonstrated that by minimizing these two mechanisms, the resonator's Q can be greatly improved. As etch holes are inevitable in certain processes such as surface micromachining (Carter J, 2005) for releasing bulk structures, the results of this study will provide useful guidelines for designers to maximize the resonator's Q even in the presence of etch holes.

5.2 Reduction of capacitive gap size for bulk mode resonators

Apart from etch holes, another problem facing the high-frequency bulk mode resonators is their large equivalent series motional resistance R_m, and hence, high insertion losses. In RF applications, the large R_m prevents the micromechanical resonators from being directly coupled to antennas, where matching impedances in the range of 50 Ω are often required. To address this problem, several tentative solutions have been reported in the literature. For instance, resonators with high dielectric constant capacitive gaps were shown to have small R_m (Lin Y W, 2005; Chandrahalim H, 2006). However, such resonators suffer from material mismatch and characterization issues and the use of dielectric material complicates the fabrication process. Another way to reduce R_m was to mechanically couple several identical resonators in an array (Demirci M U, 2003a). This approach does not require complicated fabrication processes, but the replicas of the same resonator occupy larger-than-conventional silicon area. Among different R_m reduction techniques, capacitive gap reduction is the most effective one because R_m is proportional to the fourth order of the gap size d, according to (Bannon F D, 2000):

$$R_m = \frac{d^4\sqrt{k_1 m}}{\varepsilon_0^2 N^2 W_e^2 h^2 Q V_P^2} \propto \frac{d^4}{Q} \tag{5.2}$$

where N is the number of drive/sense electrodes.

There are several dedicated processes which can be used to fabricate sub-micron capacitive gaps using ultra-thin sacrificial layers (No S Y, 2001; Quévy E, 2003). However, such methods have not been standardized to date and most of them are very costly. Therefore, many researchers still face the problems of implementing narrow gap resonators using the standard low cost foundry process. To address the limitations of the existing solutions, in this section, we will propose an innovative gap reduction technique based on electrostatic parallel-plate actuation. Using the 2 μm commercially available SOIMUMPs process, the proposed technique achieved 0.64 μm capacitive gaps for the 6.35 MHz Lamé-mode resonator to reduce its R_m by ten times and boost the output signal by 20 dB.

5.2.1 Resonator design

The SEM picture of the fabricated Lamé-mode resonator, together with its key dimensions, are presented in Fig. 5.5.

As shown, besides the standard Lamé-mode resonator (Fig. 4.1), this particular device has four movable electrodes, each comprising two stoppers and a pair of cc support beams. The parallel connection of the two cc support beams suppresses the undesirable movement of the electrode in the orthogonal direction. The operation of the resonator can be divided into two phases. First, a DC polarization voltage V_P is applied to the square resonator while the electrodes are biased at DC ground, as shown in Fig. 5.6.

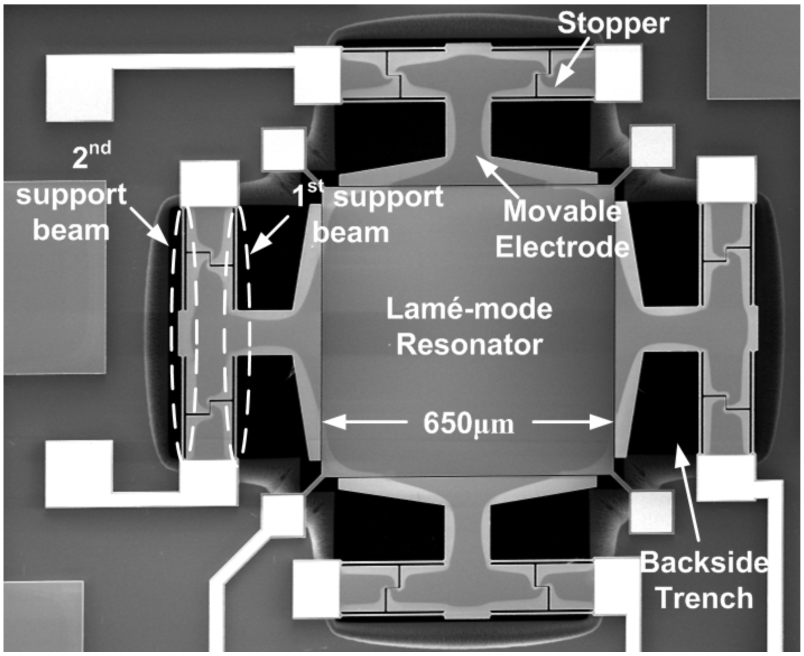

Dimension of the movable electrode:

Electrode width W_e
575 μm

Structure thickness h
25 μm

Support beam length L_s
465 μm

Support beam width W_s
4 μm

Figure 5.5 Micrograph of the proposed Lamé-mode resonator with gap reduction actuator.

As V_P is increased, the movable electrodes will get closer to the square resonator due to the electrostatic force. If V_P increases beyond a certain pull-in limit $V_{pull\text{-}in}$, the electrodes will snap to the square resonator until they hit the stoppers. After the "touch point", V_P can be reduced for normal operation. As long as it is higher than the pull-out limit $V_{pull\text{-}out}$, the electrodes will not bounce back. If the original capacitive gap size is denoted as d_0 and the one between the electrodes and stoppers as d_S, the gap size right before the pull-in limit is around $0.66d_0$ (Senturia S D, 2001) and the final gap after pull-in is $d_{final} = d_0 - d_S$. For the current design, $d_0 = 2.5$ μm and $d_S = 2$ μm. Thus, the final gap is targeted at $d_{final} = 0.5$ μm.

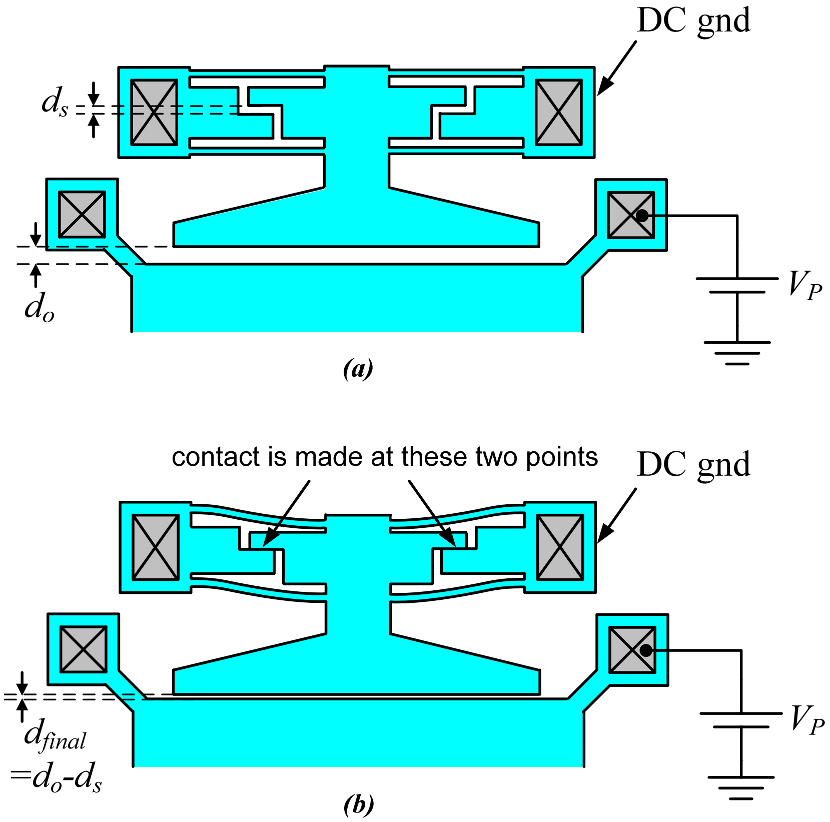

Figure 5.6 Schematic of the gap reduction actuator (a) before gap reduction and (b) after gap reduction.

5.2.2 Results and discussion

After fabrication, the resonator die was wire-boned to a PCB and tested using the same measurement setup as shown in Fig. 4.2 with C_f=3 pF and R_f=685 kΩ. The air pressure of the measurement can be controlled from high vacuum mode (37.5 μTorr) up to 1 atmosphere.

Fig. 5.7 presents the zoom-in micrographs of the capacitive gap region before and after pull-in. It is evident that after pull-in, the gap size becomes much narrower. The measured $V_{pull\text{-}in}$ and $V_{pull\text{-}out}$ are 65V and 35V, respectively. Based on $V_{pull\text{-}in}$ and $V_{pull\text{-}out}$ values, d_0 and d_{final} can be calculated to be 2.7 µm and 0.64 µm by solving the pull-in and pull-out formulas (Senturia S D, 2001):

$$V_{pull-in} = \sqrt{\frac{8k_s d_0^3}{27\varepsilon_0 W_e h}} \tag{5.3}$$

and

$$V_{pull-out} = \sqrt{\frac{2k_s\left(d_0 - d_{final}\right)d_{final}^2}{\varepsilon_0 W_e h}} \tag{5.4}$$

where k_s is the spring constant of the two support beams in parallel:

$$k_s = 2\times 16.23E\frac{W_s^3 h}{L_s^3} \tag{5.5}$$

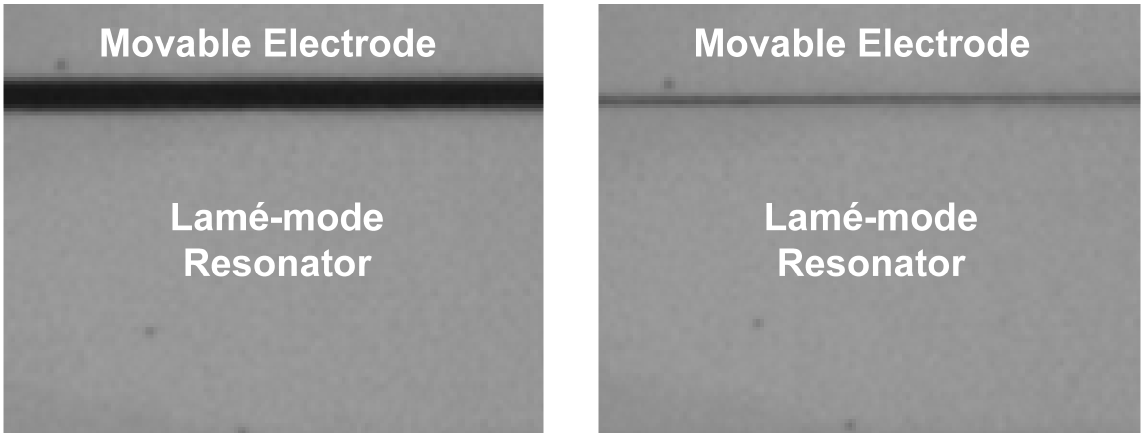

(a) ***(b)***

Figure 5.7 Zoom-in view of the electrode gap (a) before gap reduction and (b) after gap reduction.

It can be seen from Eqs. (5.3) and (5.4) that in order to achieve reasonably low $V_{pull\text{-}in}$, the support beams must be soft, i.e. long and narrow. However, too soft support beams are liable to mechanical noise and ambient vibration. Hence, a proper design should make a good compromise between the softness and robustness of the support beams.

In vacuum pressure of 37.5 μTorr, the measured S21 transmission curves for the Lamé-mode resonator at V_P=60V before and after gap reduction are shown in Fig. 5.8.

As shown, the resonance peak is boosted by 20 dB after gap reduction, which is equivalent to R_m reduction by 10 times. The value of R_m can be measured based on the resonance peak of the S21 curve:

$$R_{m\_measured} = \left| \frac{1}{j2\pi f_0 C_f} \parallel R_f \right| \cdot 10^{-\frac{\text{Resonance peak}}{20}} \tag{5.6}$$

Using Eq. (5.6), $R_{m\_measured}$ is calculated to decrease from 103 kΩ before gap reduction to 9.8 kΩ after gap reduction. The reduction ratio agrees well with the theoretical predictions by Eq. (5.2).

In addition to the vacuum testing, another set of S21 transmission curves were obtained in air and summarized in Table 5.2. As shown, before gap reduction, the resonance peak cannot be observed since it is below the noise floor whereas after gap reduction, the resonance peak is about -24.6 dB, 10 dB above the noise floor, showing a Q of 13k. This demonstrates that with the proposed gap reduction technique, it is possible to use the resonator even in air.

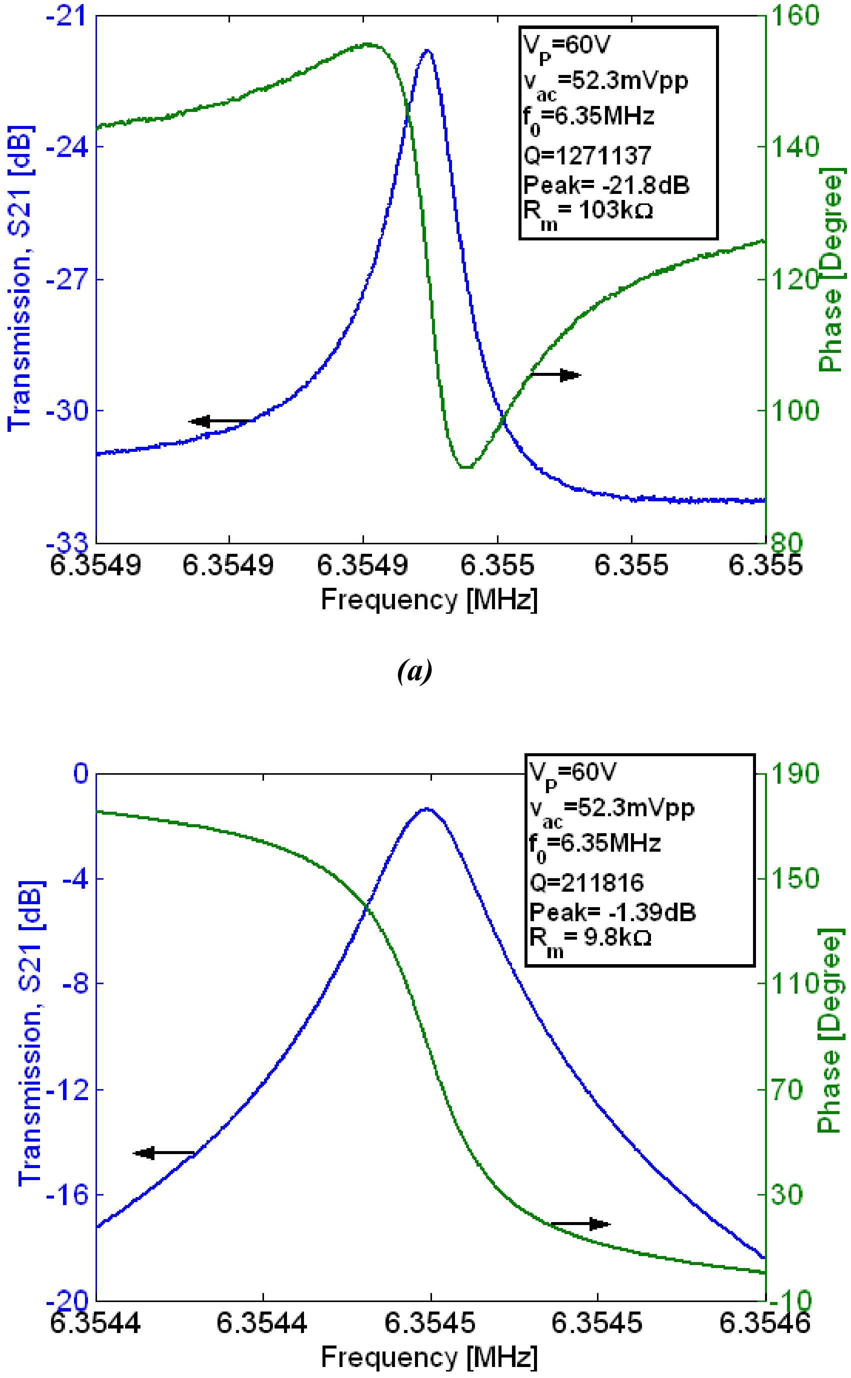

(a)

(b)

Figure 5.8 Measured transmission curve of the Lamé-mode resonator in vacuum (a) before gap reduction and (b) after gap reduction.

Table 5.2 Performance comparison of the Lamé-mode resonator before and after gap reduction (measurement was taken for V_P=60V and v_{ac}=52.3mV_{PP}).

	Vacuum (37.5 µTorr)		**Air (1 atm)**	
	Before gap reduction	**After gap reduction**	**Before gap reduction**	**After gap reduction**
Gap size	≈ $0.66d_0$=1.8µm	0.64 µm	≈ $0.66d_0$=1.8µm	0.64 µm
$\boldsymbol{Q}$	1,271,137	211,816	Cannot be measured**	12,700
Resonance peak	-21.8 dB	-1.39 dB	Cannot be measured**	-24.6 dB
$\boldsymbol{R_{m\_measured}}$	103 kΩ	9.8 kΩ	Cannot be measured**	142 kΩ

** In air, before gap reduction, the resonance peak is below the noise floor and hence the specific parameters cannot be measured.

Next, the repeatability of the proposed gap reduction technique is presented in Fig. 5.9 where the original gap size d_0 and final gap size d_{final} were measured for the same resonator (Fig. 5.5) on six different dies. In Fig. 5.9, the average d_0 for die 1 to die 6 is 2.675 µm with maximum and minimum values of 2.71 µm and 2.62 µm, respectively. The average d_{final} is 0.66 µm with maximum and minimum values of 0.71 µm and 0.62 µm, respectively. Hence, good uniformity is achieved with the proposed gap reduction technique across different dies.

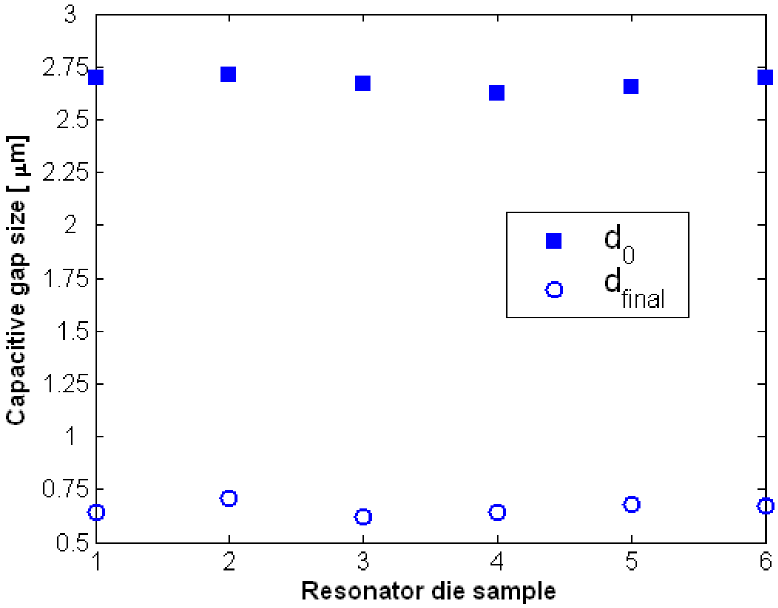

Figure 5.9 Repeatability test of capacitive gap size on six different resonator die samples.

Another interesting observation in Figure 5.8 is that before gap reduction, the frequency of the AC excitation voltage and the resonant frequency of the electrodes are well separated, and hence the electrodes hardly move during the measurement. Consequently, the measured parameters of the resonator such as the quality factor Q and motional resistance R_m are comparable to those of the Lamé-mode resonator with fixed electrodes. However, after gap reduction, Q decreases from originally above one million to about 212k. The same phenomenon (i.e. Q reduction) was observed for a cc beam resonator with a final gap of 0.4 μm. The drop in the measured Q is found to be attributed to the various loading effects such as the parasitic resistance, DC polarization voltage V_P, partial depletion, etc. in the signal path (Yongchul A, 2001; Ho G K, 2005; Pourkamali S, 2007). Although it is tough to identify the contributions from each individual effect, in practice, all the loading effects can be simply lumped into an equivalent resistor R_L, connected in series with the resonator. To elucidate the effect of R_L, Fig. 5.10 presents the equivalent circuit model for a typical micromechanical resonator.

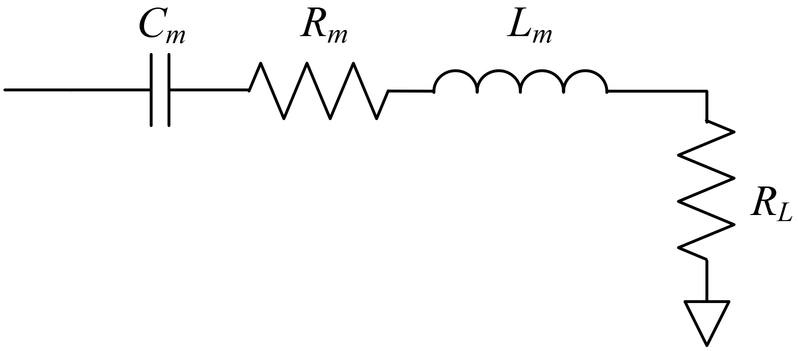

Figure 5.10 Equivalent circuit model for a micromechanical resonator.

As shown, the micromechanical resonator acts as a series RLC network in the electrical domain. At resonance, impedances of C_m and L_m cancel out and only R_m is left. Here we recall the definitions of the unloaded quality factor $Q_{unloaded}$ and loaded quality factor Q_{loaded} (Ho G K, 2005):

$$Q_{unloaded} = \frac{2\pi f_0 L_m}{R_m} \tag{5.7a}$$

$$Q_{loaded} = \frac{2\pi f_0 L_m}{R_m + R_L} = \frac{2\pi f_0 L_m}{R_{m\_measured}} \tag{5.7b}$$

Eq. (5.7) indicates that $Q_{unloaded}$ represents the intrinsic properties of the resonator whereas Q_{loaded} is the measured quality factor including the loading effect of R_L. $Q_{unloaded}$ is related to Q_{loaded} via:

$$Q_{loaded} = Q_{unloaded}\frac{R_m}{R_m + R_L} = Q_{unloaded}\frac{R_m}{R_{m\_measured}} \tag{5.8}$$

For the Lamé-mode resonator of this work, before gap reduction, the resonator's R_m is much larger than R_L. According to Eq. (5.8), the loading effect of R_L on Q_{loaded} is minimal. In other words, we have:

$$Q_{unloaded} \approx Q_{loaded}\,|_{\text{before gap reduction}} = 1,271,137 \tag{5.9}$$

However, once the gap is reduced, R_m becomes much smaller and comparable to R_L and this causes the drop in the measured Q_{loaded} value. To estimate the value of R_L, the measured motional resistance $R_{m\_measured}$ after gap reduction is plotted versus $1/V_P^2$ in Fig. 5.11. The curve is linear, as expected from Eq. (5.2), but exhibits a constant offset of 8 kΩ which is identified as the loading resistor R_L in series with the resonator.

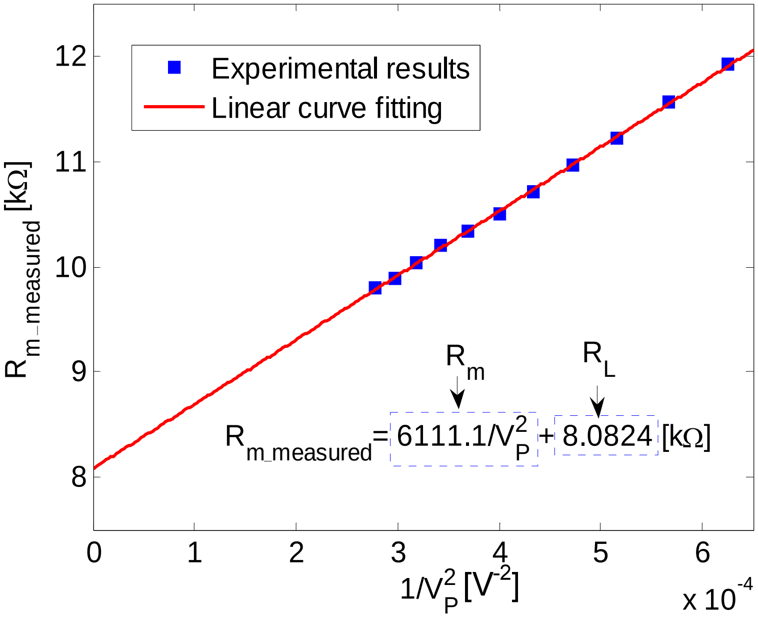

Figure 5.11 Measured motional resistance $R_{m\_measured}$ versus $1/V_P^2$ for the Lamé-mode resonator, showing a linear trend with a constant loading (R_L).

Substituting $R_L = 8$ kΩ and $Q_{unloaded} \approx 1,271,137$ (Eq. (5.9)) back into Eq. (5.8), the value of Q_{loaded} can be predicted. Fig. 5.12 presents a comparison between the estimated Q_{loaded} with measured Q_{loaded} as a function of V_P. As shown, the two curves agree quite well with each other, demonstrating that the Q reduction is caused by the loading effects and confirming the value of R_L in the signal path. Next, to further verify that it is not the defect in the design of gap reduction actuators that cause the Q reduction, another Lamé-mode resonator was implemented with $d_0 = 4$ µm and $d_{final} = 2$ µm. The measured Q of this particular device is around 1.57 million, which is very close to the measured Q of the Lamé-mode resonator with 2 µm capacitive gap size and fixed electrodes.

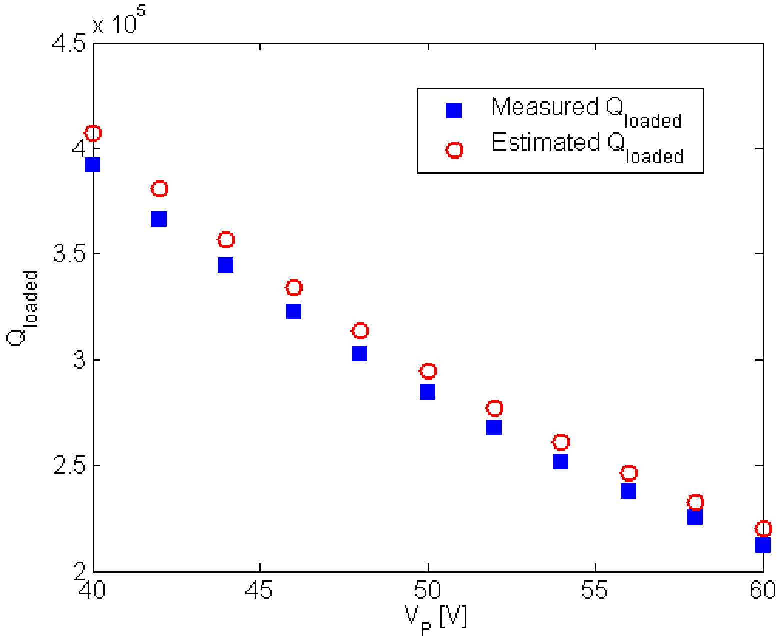

Figure 5.12 Estimated and measured loaded quality factor Q_{loaded} as a function of V_P.

5.2.3 Summary

The design of sub-micron capacitive gaps using standard 2 µm foundry process has been presented for the 6.35 MHz Lamé-mode resonator. This gap reduction technique achieved a final gap of 0.64 µm for our resonator which boosted the resonance peak by about 20 dB. The reduction in the quality factor after gap reduction was observed and we concluded that it was caused by the various loading effects in the signal path. This work demonstrates how sub-micron gaps can be innovatively implemented in low cost standard processes. Such a method can be used for various bulk mode resonators to improve their overall device performance.

Chapter 6 Conclusions and future work

6.1 Conclusions

Nonlinear vibration is one of the key issues with micromechanical resonators in limiting the ultimate device performance that can be achieved. However, due to the complexity of the nonlinear mechanism, the existing studies on the resonators' nonlinearities are still not well established and most of them are applicable to only specific simple structures.

In this thesis, we have proposed a semi-analytic technique which can be used to investigate the nonlinearities of virtually any types of resonators. The merit of the proposed technique is that it is capable of extracting both the linear and nonlinear resonator parameters from just preliminary measurement results. Subsequently, based on the extracted parameters, the accurate lumped model can be constructed which reveals the intrinsic nonlinear properties of the resonator. Using the proposed technique, we have presented the studies of nonlinearities in both flexural mode and bulk mode resonators including the ff beam, cc beam and Lamé-mode resonators. The key findings on the nonlinear properties of these resonators are summarized as follows:

1) The nonlinearity in the fundamental-mode ff beam resonator is of the hardening type which bends the resonance to higher frequencies. In contrast, the second-mode ff beam resonator can exhibit either spring softening or hardening nonlinearity depending on the specific support beam designs.

2) The useful first-order nonlinearity cancellation phenomenon demonstrated using the cc beam resonator not only reduces the amplitude-frequency coefficient to almost zero, but also boosts the critical vibration amplitude and maximum storable energy of the device. Furthermore, in the nonlinearity cancellation regime, the resonator behavior is governed by even higher order (above 3^{rd} order) nonlinearities.

3) The nonlinearity in the Lamé-mode bulk resonator is of the softening type and progressively bends the resonance to lower frequencies as the vibration amplitude grows. Compared with the flexural mode resonator, the Lamé-mode bulk resonator performs much better in terms of the resonant frequency, quality factor, amplitude-frequency coefficient and power handling capability.

Motivated by the superior performance of the Lamé-mode resonator, in the last chapter, we have conducted two further studies, namely the effect of etch holes on the quality factor and capacitive gap reduction. For the first topic, our study conclusively shows that the etch holes reduce the quality factors by more than an order of magnitude from 1.7 million to 116k due to two main energy loss mechanisms. It is also demonstrated that the quality factor depends on the specific location of etch holes on the resonator. As for the second topic, we have presented an innovative gap reduction technique to achieve sub-micron capacitive gaps for the resonator using the standard low cost 2 μm SOIMUMPs process from MEMSCAP. The resonator gap size was experimentally measured to be 0.64 μm, which boosted the resonance peak by 20 dB.

6.2 Suggestions for future work

This thesis presents nonlinear properties of different micromechanical resonators and provides useful techniques to optimize the device performance. However, there still remains a large amount of research to be done, especially in the area of oscillator circuit design, temperature compensation, packaging technology, etc.. Next, suggestions will be provided for each of these areas.

1) Oscillator circuit design

Firstly, for the resonators discussed in this thesis, it is necessary to implement the oscillator circuits to facilitate the closed-loop phase noise measurement. Besides the sustaining amplifier and output buffer stage, an automatic gain control (AGC) block should also be included in the circuit loop to prevent the resonator from entering the strong nonlinear regime (Roessig T A, 1997; Lin Y W, 2004). Furthermore, since the electronic circuits usually contribute most of the noise and power dissipation, the oscillator design also calls for dedicated low noise and low power solutions.

2) Temperature compensation

Secondly, typical micromechanical resonators exhibit temperature coefficients TC_f's around -20 ppm/^{o}C mainly due to the thermal dependence of Young's modulus (Hsu W T, 2000). Such TC_f's are more than 10 times larger than even those of the lowest grade quartz crystal oscillators (Frerking M E, 1978). Hence, temperature compensation is required for micromechanical resonators to achieve sufficient thermal stability. For flexural mode resonators, the compensation can be done using either electrostatic or mechanical methods. However, there are still no effective compensation methods for bulk mode resonators.

The principle of electrostatic compensation is to generate a temperature dependent k_{1e} to cancel the drift in k_{1m}, as shown by Eq. (2.18) (Hsu W T, 2002; Ho G K, 2005). This method is able to achieve TC_f = -0.24 ppm/°C for a 10 MHz cc beam resonator. However, as the resonant frequency scales up, k_{1m} will become much larger than k_{1e}, especially for bulk mode resonators. Therefore, using k_{1e} to compensate the k_{1m} drift might no longer be feasible.

On the other hand, the mechanical compensation can be achieved by introducing a temperature dependent tensile stress on the resonator to counteract the negative TC_f (Hsu W T, 2000). The reported data shows the TC_f reduction from -17 ppm/°C to -2.5 ppm/°C for a 10 MHz cc beam resonator. This method seems to be a feasible solution for high frequency bulk mode resonators as well. However, more work needs to be done to carefully tailor the resonator structure and fabrication process in order to generate sufficient stress for compensation.

3) Packaging technology

Finally, the packaging technology needs to be properly addressed before micromechanical resonators can be fully commercialized. The measurement setup in the vacuum chamber is by no means the best solution and hence a robust yet manufacturable packaging process has to be developed. A good packaging technology should not only facilitate convenient and faithful characterization of the resonator, but also provide enough protection against device failure and mechanical aging.

References

Agarwal M and Mehta H 2007 Scaling of amplitude-frequency-dependence nonlinearities in electrostatically transduced microresonators *J. Applied Phys.* **102** 074903

Andrews M K *et al* 1993 A resonant pressure sensor based on a squeezed film of gas *Sensors Actuators* A **36** pp 219-26

Ayela F and Fournier T 1998 An experimental study of anharmonic micromachined silicon resonators *Meas. Sci. and Technol.* **9** pp 1821-30

Bannon F D, Clark J R and Nguyen C T C 2000 High-*Q* HF microelectromechanical filters *J. Solid-State Circuits* **35** pp 512-26

Berkenpas E, Bitla S, Millard P and Cunha M. P. da 2004 Pure shear horizontal SAW biosensor on langasite *IEEE Trans. Ultrason., Ferroelectr., Freq. Contr.* **51** (11) pp 1404-11

Bhave S A, Gao D, Maboudian R and Howe R T 2005 Fully-differential poly-SiC Lamé-mode resonator and checkerboard filter *Proc. MEMS 2005 (Miami)* pp 223-6

Carter J *et al* 2005 *POLYMUMPs Design Handbook* MEMScAP

Chandrahalim H, Weinstein D, Cheow L F and Bhave S A 2006 Channel-select micromechanical filters using high-K dielectrically transduced MEMS resonators *Proc. MEMS 2006* pp 894-7

Demirci M U, Abdelmoneum M A and Nguyen C T C 2003a Mechanically corner-coupled square microresonator array for reduced series motional resistance *Proc. Transducers '03* pp 955-8

Demirci M U and Nguyen C T C 2003b Higher-mode free-free beam micromechanical resonators *Proc. 2003 IEEE Int. Freq. Contr. Symp. (Florida)* pp 810-8

Franke A E *et al* 1999 Post-CMOS integration of germanium microstructures *Proc. MEMS 1999 (Orlando)* pp 630-7

Frerking M E 1978 *Crystal oscillator design and temperature compensation* (Van Nostrand)

Frerking M E 1996 Fifty years of progress in quartz frequency standards *Proc. IEEE Int. Freq. Contr. Symp.* pp 33-46

Greywall D S 2005 Sensitive magnetometer incorporating a high-*Q* nonlinear mechanical resonator *Meas. Sci. Technol.* **16** pp 2473-82

Greywall D S *et al* 1994 Evading amplifier noise in nonlinear oscillators *Phys. Rev. Lett.* **72** pp 2992-5

Gui C, Legtenberg R, Tilmans H A, Fluitman J H and Elwenspoek M 1998 Nonlinearity and hysteresis of resonant strain gauges *J. MEMS* **7** pp 122-7

Hao Z L, Erbil A and Ayazi F 2003 An analytical model for support loss in micromachined beam resonators with in-plane flexural vibrations *Sensors Actuators* A **109** pp 156-64

Ho G K *et al* 2005 Low-motional-impedance highly-tunable, I^2 resonators for temperature compensated reference oscillators *Proc. MEMS 2005*, pp 116-20

Ho G K *et al* 2006 Temperature compensated IBAR reference oscillators *Proc. MEMS 2006* pp 910-3

Howe R T and Muller R S 1983 Polycrystalline silicon micromechanical beams *J. of the Electrochemical Society* **130** pp 1420-3

Howe R T 1987 Resonant microsensors *Tech. Digest 4th Int. Conf. Solid-State Sensors and Actuators* pp 843-8

Hsu W T, Clark J R and Nguyen C T C 2000 Mechanically temperature-compensated flexural-mode micromechanical resonators *Tech. Digest IEDM* pp 399-402

Hsu W T, Clark J R and Nguyen C T C 2001 *Q*-Optimized lateral free-free beam micromechanical resonators *Proc. Transducers '01* (*Munich*) pp 1110-3

Hsu W T and Nguyen C T C 2002 Stiffness compensated temperature insensitive micromechanical resonators *Proc. MEMS 2002* pp 731-4

Hsu W T and Brown A R 2007 Frequency trimming for MEMS resonator oscillators *Proc. IEEE Int. Freq. Contr. Symp.* pp 1088-91

Ikeda K *et al* 1988 Silicon pressure sensor with resonant strain gauges built into diaphragm *Tech. Digest 7th Sensor Symp.* pp 55-8

Kaajakari V *et al* 2004a Square-extensional mode single-crystal silicon micromechanical resonator for low phase noise oscillator applications *IEEE Electron Device Lett.* **25** (4)

Kaajakari V *et al* 2004b Nonlinear limits for single-crystal silicon microresonators *J. MEMS* **13** pp 715-24

Kaajakari V, Koskinen J K and Mattila T 2005 Phase noise in capacitively coupled micromechanical oscillators *IEEE Trans. Ultrason., Ferroelect., Freq. Contr.* **52** (12) pp 2322-31

Kinnell P K, Craddock R and Ward M C L 2004 Nonlinear model for the design of stable MEMS resonators *Proc. 18th Eurosensors Conf. (Rome)*

Kung J T (Analog Devices Inc., Norwood, MA) 1996 Methods for planarization and encapsulation of micromechanical devices in semiconductor processes *U.S. Patent* 5, 504, 026

Landau L D and Lifshitz E M 1999 *Mechanics* 3rd edn (Oxford, UK: Butterworth-Heinemann)

Lamminmaki T *et al* 2000 Electromechanical analysis of micromechanical SOI-fabricated RF resonators *Proc. 3rd Int. Conf. Modeling and Simulation of Microsyst., Semiconductors, Sensors and Actuators (San Diego)* pp 217-20

Lavigne G F and Miller S L 1998 A performance analysis system for MEMS using automated imaging methods *Proc. IEEE Int. Test Conf.* pp 442-7

Lee S and Nguyen C T C 2004 Phase noise amplitude dependence in self limiting wine-glass disk oscillators *Proc. Hilton Head 2004: A Solid State Sensor, Actuator and Microsystem Workshop (South Carolina)*

Lee T H 1998 *The design of CMOS radio-frequency integrated circuits* (U.K.: Cambridge University Press)

Lin Y W *et al* 2004 Series-resonant VHF micromechanical resonator reference oscillators *J. Solid-State Circuits* **39** (12) pp 2477-91

Lin Y W *et al* 2005 Vibrating micromechanical resonators with solid dielectric capacitive-transducer gaps *Proc. IEEE Int. Freq. Contr. Symp.* pp 128-34

Majjad H, Coudevylle J-R, Basrour S and de Labachelerie M 2001 Modeling and characterization of Lamé-mode microresonators realized by UV-LIGA *Proc. Transducers '01* **1** pp 300-3

Miller D C *et al* 2007 Characteristics of a commercially available silicon-on-insulator MEMS material *Sensors Actuators* A **138** pp 130-44

Miller K et al 2004 *SOIMUMPs Design Handbook* MEMScAP

Nguyen C T C 1991 Electromechanical characterization of microresonators for circuit applications *Master Dissertation* University of California, Berkeley

Nguyen C T C and Howe R T 1993 CMOS micromechanical resonator oscillator *Tech. Digest IEDM* pp 199-202

Nguyen C T C and Howe R T 1999 An integrated CMOS micromechanical resonator high *Q* oscillator *J. Soild-State Circuits* **34** (4) pp 440-55

Nguyen C T C 2001 Vibrating RF MEMS for low power wireless communications *Proc. iMEMS '01 (Singapore)* pp 21-34

No S Y and Ayazi F 2001 The HARPSS process for fabrication of nano-precision silicon electromechanical resonators *Proc. IEEE NANO '01* pp 489-94

Palaniapan M 2002 Integrated surface micromachined frame microgyroscopes *PhD Dissertation* University of California, Berkeley

Palaniapan M and Lynn K 2006 Nonlinear behavior of SOI free-free micromechanical beam resonator *Proc. 20th Eurosensors Conf. (Sweden)*

Palaniapan M and Lynn K 2007 Micromechanical resonator with ultra-high quality factor *Electron. Lett.* **43** pp 1090-2

Pourkamali S, Hao Z L and Ayazi F 2004 VHF single crystal silicon capacitive elliptic bulk-mode disk resonators - Part II: Implementation and Characterization *J. MEMS* **13** (6) pp 1054-62

Pourkamali S and Ayazi F 2005 Electrically coupled MEMS bandpass filters Part I: with coupling element *Sensors Actuators* A **122** pp 307-16

Pourkamali S, Ho G K and Ayazi F 2007 Low-impedance VHF and UHF capacitive silicon bulk acoustic-wave resonators Part II: measurement and characterization *IEEE Trans.Electron Devices* **54** (8) 2024-30

Quévy E *et al* 2003 Ultimate technology for micromachining of nanometric gap HF micromechanical resonators *Proc. MEMS 2003 (Kyoto)* pp 157-60

Rabinovich V L, Gupta R K and Senturia S D 1997 The effect of release-etch holes on the electromechanical behavior of MEMS structures *Proc. Transducers '97* pp 1125-8

Roessig T A, Howe R T and Pisano A P 1997 Nonlinear mixing in surface micromachined tuning fork oscillators *Proc. IEEE Int. Freq. Contr. Symp.*

Roessig T A 1998 Integrated MEMS tuning fork oscillators for sensor applications *PhD Dissertation* University of California, Berkeley

Schmidt M A and Howe R T 1986 Resonant structures for integrated sensors *Proc. Hilton Head 1986: IEEE Solid State Sensor Workshop (South Carolina)*

Senturia S D 2001 *Microsystem Design* (Kluwer Academic Publishers)

Sharpe Jr W N *et al* 1997 Effect of etch holes on the mechanical properties of polysilicon *J. Vac. Sci. Tech.* B **15** pp 1599-603

Smith J *et al* 1995 Embedded micromechanical devices for the monolithic integration of MEMS with CMOS *Tech. Digest IEDM* pp 609-12

Smits J G, Tilmans H A C and Lammerink T S J 1985 Pressure dependence of resonant diaphragm pressure sensors *Tech. Digest 3rd Int. Conf. Solid-State Sensors and Actuators* pp 93-6

Takeuchi H *et al* 2004 Ge-blade damascene process for post-CMOS integration of nano-mechanical resonators *IEEE Electron Device Lett.* **25**(8) pp 529-31

Tilmans H A, Elwespoek M and Fluitman J H 1992 Micro resonant force gauges *Sensors Actuators* **A** 30 pp 35-53

Tilmans H A and Legtenberg R 1994 Electrostatically driven vacuum-encapsulated polysilicon resonators. Part II. Theory and performance *Sensors and Actuators* **A** 45 pp 67-84

Timoshenko S 1974 *Vibration problems in engineering* 4th edn (New York: Wiley)

Turner G C and Andrews M K 1995 Frequency stabilization of electrostatic oscillators *Digest of the 8th International Conf. on Solid-State Sensors and Actuators* **2** pp 624-6

Vanlong Technology Co., Ltd. 2008 [Online] http://www.vanlong.com/

Veijola T and Mattila T 2001 Modeling of nonlinear micromechanical resonators and their simulation with the harmonic-balance method *Int. J. RF Microwave Comput.-Aided Eng.* **11** pp 310-21

Wang K and Nguyen C T C 1999 High-order medium frequency micromechanical electronic filters *J. MEMS* **8** (4) pp 534-57

Wang J *et al* 2004 1.51 GHz nanocrystalline diamond micromechanical disk resonator with material-mismatched isolating support *Proc. MEMS 2004*

Wong A C and Nguyen C T C 2004 Micromechanical mixer-filters *J. MEMS* **13** (1) pp 100-12

Wright P V 1992 A review of SAW resonator filter technology *Proc. IEEE Ultrason. Symp.* pp 29-38

Yongchul A, Guckel H and Zook J D 2001 Capacitive microbeam resonator design *J. Micromech. Microeng.* **11** pp 70-80

Young W C and Budynas R G 2002 *Roark's formulas for stress and strain* 7th edn (New York: McGraw-Hill)

Younis M I and Nayfeh A H 2003 A study of the nonlinear response of a resonant microbeam to an electric actuation *Nonlinear Dynamics* **31** pp 91-117

Yurke B *et al* 1995 Theory of amplifier-noise evasion in an oscillator employing a nonlinear resonator *Phys. Rev.* A **51** pp 4211-29

List of publications

Journal papers

Shao L C, Palaniapan M, Khine L and Tan W W 2007 Micromechanical resonators with sub-micron capacitive gaps in 2µm process *Electronics Lett.* **43** (25)

Shao L C and Palaniapan M 2008 Effect of etch holes on quality factor of bulk-mode micromechanical resonators *Electronics Lett.* **44** (15)

Shao L C, Palaniapan M, Tan W W and Khine L 2008 Nonlinearity in micromechanical free-free beam resonators: modeling and experimental verification *J. Micromech. Microeng.* **18** 025017

Shao L C, Palaniapan M and Tan W W 2008 The nonlinearity cancellation phenomenon in micromechanical resonators *J. Micromech. Microeng.* **18** 065014

Shao L C, Wong C L and Palaniapan M 2008 Study of the nonlinearities in micromechanical clamped-clamped beam resonators using stroboscopic SEM *J. Micromech. Microeng.* **18** 085019

Shao L C, Niu T and Palaniapan M 2009 Nonlinearities in high-*Q* SOI Lamé-mode bulk resonator *J. Micromech. Microeng.* (Accepted)

Conference papers

Shao L C, Palaniapan M 2007 Nonlinear behavior modeling of micromechanical free-free beam resonators *Proc. SPIE Microelectronics, MEMS and Nanotechnology (Canberra)*

Shao L C, Palaniapan M, Khine L and Tan W W 2008 Nonlinear behavior of Lamé-mode SOI bulk resonator *Proc. IEEE Int. Freq. Contr. Symp.* pp 646-50

Khine L, Palaniapan M, **Shao L C** and Wong W K 2008 Characterization of SOI Lamé-mode square resonators *Proc. IEEE Int. Freq. Contr. Symp.* pp 625-8

Shao L C, Wong C L, Khine L, Palaniapan M and Wong W K 2008 Study of various characterization techniques for MEMS devices *Eurosensors 2008 (Dresden)*

Wong C L, **Shao L C**, Khine L, Palaniapan M and Wong W K 2008 Novel acoustic phonon detection technique to determine temperature coefficient of frequency in MEMS resonators *Eurosensors 2008 (Dresden)*

Khine L, Palaniapan M, **Shao L C** and Wong W K 2008 Temperature compensation of MEMS oscillator composed of two adjoining square and beam resonators *Eurosensors 2008 (Dresden)*

Niu T, Palaniapan M, Khine L and **Shao L C** 2008 MEMS oscillators using bulk-mode resonators *Eurosensors 2008 (Dresden)*

Wong C L, **Shao L C** and Palaniapan M 2008 Characterization techniques for NEMS/MEMS devices *Proc. SPIE Smart Materials, Nano- and Micro-Smart Systems (Melbourne)*